DYNAMIC MODEL FOR SMALL-CAPACITY AMMONIA-WATER ABSORPTION CHILLER

A Thesis
Presented to
The Academic Faculty

By

Vinodh Kumar Viswanathan©

In Partial Fulfillment
Of the Requirements for the Degree
Master of Science in Mechanical Engineering

Georgia Institute of Technology

August 2013

DYNAMIC MODEL FOR SMALL-CAPACITY AMMONIA-WATER ABSORPTION CHILLER

Approved by:

Dr. Srinivas Garimella, Adviser
G.W. Woodruff School of Mechanical Engineering
Georgia Institute of Technology

Dr. Sheldon Jeter
G.W. Woodruff School of Mechanical Engineering
Georgia Institute of Technology

Dr. Aldo A. Ferri
G.W. Woodruff School of Mechanical Engineering
Georgia Institute of Technology

Date Approved: 2013-04-18

DEDICATION

To my family

ACKNOWLEDGEMENTS

I would like to thank my adviser Dr. Srinivas Garimella for his guidance and support through the course of work. Financial support from the US Advanced Research Projects Agency – Energy (ARPA-E) (contract DE-AR0000135) is gratefully acknowledged.

I would like to thank the Sustainable Thermal Systems Laboratory, in particular Alexander Rattner and Matthew Determan for their guidance and mentoring throughout my Masters work. Also, I appreciate the valuable feedback and comments on my thesis from Anand Nagavarapu, Brian Fronk and Adrienne Little.

Finally, I would like to thank my committee members for their guidance in the course of this work.

TABLE OF CONTENTS

LIST OF TABLES

LIST OF FIGURES

LIST OF SYMBOLS AND ABBREVIATIONS

Symbols

A	area (m^2)
Bo	boiling number (-)
Co	convection number (-)
COP	coefficient of performance (-)
C_{valve}	valve coefficient (kg s^{-1} Pa^{-1})
C_p	heat capacity (J kg^{-1} K^{-1})
F_{fl}	fluid surface parameter (-)
G	mass flux (kg m^{-2} s^{-1})
h	enthalpy (J kg^{-1})
h_{lv}	latent heat of vaporization(kJ kg^{-1})
M, m	mass (kg)
$\dot{m}$	mass flow rate (kg s^{-1})
N	number of segments (-)
P_{high}	high-side pressure (kPa)
P_{low}	low-side pressure (kPa)
P	pressure (kPa)
ΔP	pressure difference (kPa)
$\dot{Q}$	heat transfer rate (W)
q	vapor quality (-)
R	residue, in rate of energy (W)

t	time (s)
T	temperature (ºC)
U	extensive internal energy (J)
UA	overall heat transfer coefficient (W K^{-1})
x	concentration of ammonia (-)
We	Weber number (-)

Abbreviations

COP	coefficient of performance
LMTD	log-mean temperature difference
NTU	number of transfer units

Greek Symbols

α	heat transfer coefficient (W m^{-2} K^{-1})
ε	effectiveness
φ	angle (radians)
ρ	density (kg m^{-3})

Subscripts

ABS,A	absorber
C, c	cold
cs, conc	concentrated solution
COND	condenser
cf	coupling fluid
cf-w	between coupling fluid and wall
DES, D	desorber

ds, dil	dilute solution
EVAP, E	evaporator
EV	expansion valve
f-w	between working fluid and wall
H, h	hot
high	high-side
HX	heat exchanger
i	index for segment of heat exchanger
in	inlet
l, liq	liquid
lm	log-mean temperature
low	low-side
out	outlet
P	pump
RECT	rectifier
ref	refrigerant
RPC	refrigerant pre-cooler
RHX	refrigerant heat exchanger
RT	refrigerant tank
seg	segment
SHX	solution heat exchanger
sol	solution
ST	solution tank

v,vap	vapor
w	wall
1f, 2f	fluids 1 and 2

SUMMARY

Optimization of the performance of absorption systems during transient operations such as start-up and shut-down is particularly important for small-capacity chillers and heat pumps to minimize lifecycle costs. Dynamic models in the literature have been used to study responses to step changes in a single parameter, but more complex processes such as system start-up have not been studied in detail. A robust system-level model for simulating the transient behavior of an absorption chiller is developed here.

Individual heat and mass exchangers are modeled using detailed segmental models. The UA-values and thermal masses of heat exchangers used in the model are representative of a practical operational chiller. Thermal masses of the heat exchangers and energy storage in the heat exchanging fluids are accounted for to achieve realistic transient simulation of the heat transfer processes in the chiller. The pressure drop due to fluid flow across the heat exchangers is considered negligible in comparison to the pressure difference between the high- and low-side components (~ 1.5 MPa). In components with significant mass transfer effects, reduced-order models are employed to decrease computational costs while also maintaining accurate system response.

Mass and species storage in the cycle are modeled using storage devices. The storage devices account for expansion and contraction of the refrigerant and solution in the cycle as the system goes through start-up, shut-down, and other transient events. A counterflow falling film desorber model is employed to account for the heat and mass transfer interactions between the liquid and vapor phases, inside the desorber. The liquid film flows down counter to the rising vapor, thereby exchanging heat with the counterflowing heated coupling fluid. A segmented model is used to account for these processes, and a solver is developed for performing rapid

iteration and quick estimation of unknown vapor and liquid states at the outlet of each segment of the desorber. Other components such as the rectifier, expansion valves and solution pump are modeled as quasi-steady devices.

System start-up is simulated from ambient conditions, and the coupling fluid temperatures are assumed to start up to their steady-state values within the first 90 s of simulation. It is observed that the system attains steady-state in approximately 550 s. The evaporator cooling duty and COP of the chiller during steady-state are observed to be 3.41 kW and 0.60, respectively. Steady-state parameters such as flow rates, heat transfer rates and concentrations are found to match closely with results from simulations using corresponding steady-state models. Several control responses are investigated using this dynamic simulation model. System responses to step changes in the desorber coupling fluid temperature and flow rate, solution pumping rate, and valve setting are used to study the effects of several control strategies on system behavior. Results from this analysis can be used to optimize start-up and steady state performances. The model can also be used for devising and testing control strategies in commercial applications.

1. INTRODUCTION

1.1 Overview

Absorption cycles have been employed in refrigeration for many years, but have attracted renewed interest in recent years due to environmental concerns related to global warming. Most absorption systems use working fluids that have extremely low global warming potential (GWP) values compared to conventional refrigerants such as hydrochlorofluorocarbons (HCFC). Furthermore, the ability to utilize waste heat as the input energy in these thermally driven systems for space conditioning and refrigeration applications can lead to increased energy savings.

Conventional space-conditioning applications typically employ vapor-compression systems to provide cooling and heating. Vapor-compression heat pumps operate by circulating a refrigerant between low and high pressure sides, removing heat from a low temperature source and rejecting heat to a high temperature sink. Figure 1.1 shows a schematic of a simple vapor-compression heat pump. Low pressure refrigerant vapor enters the compressor where it is compressed to a high pressure by work input W_{in}. It then enters the condenser where it condenses, rejecting its latent heat Q_c to the hot ambient. The refrigerant leaves the condenser as a subcooled liquid at (3) before it flows through an expansion valve to a lower pressure. Subsequently, the refrigerant enters the evaporator at (4), where it acquires heat Q_E from the conditioned space to provide the desired cooling. Once the refrigerant is completely evaporated, it returns to the compressor at (1). The vapor compression cycle requires high-grade electricity to power the compressor and produce heating or cooling.

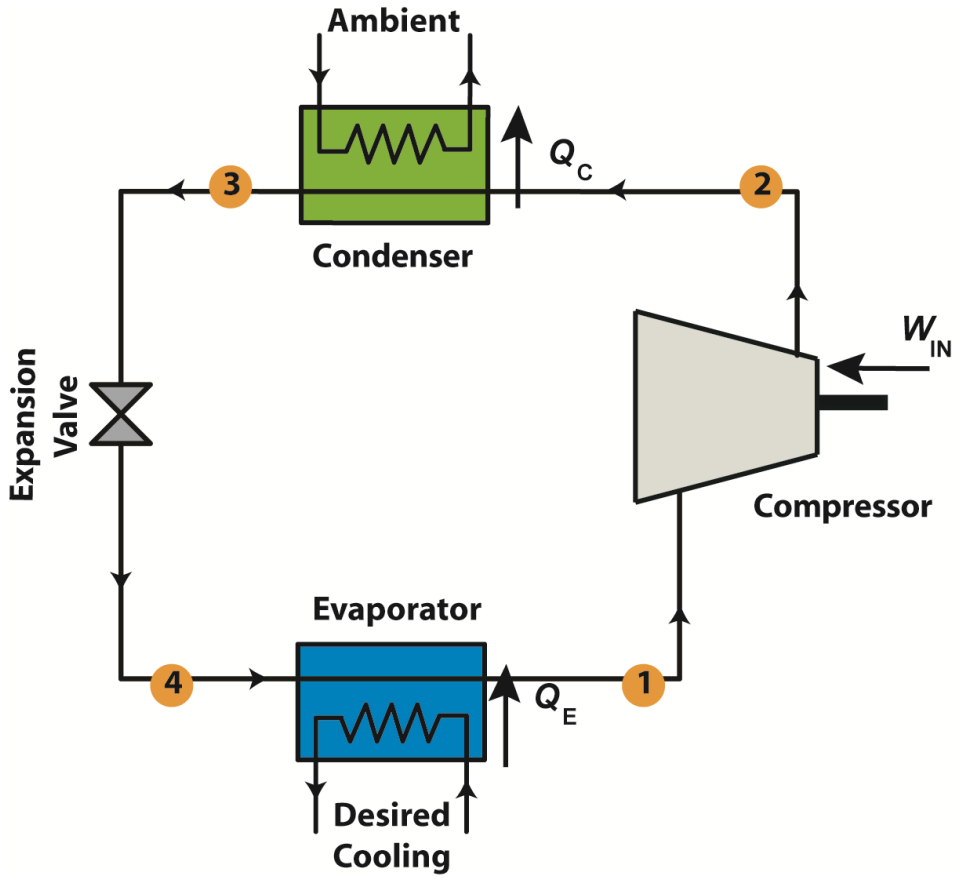

Figure 1.1 Vapor compression cycle

In general, vapor-compression systems have a higher coefficient of performance (COP) than an absorption system. However, a high COP can potentially be offset by high conversion and transmission losses associated with power generation from fossil fuels, leading to a low overall primary source based efficiency. Also, vapor-compression systems use synthetic refrigerants that are detrimental to the environment.

In comparison, an absorption heat pump uses a condenser, evaporator and an expansion valve similar to a vapor compression heat pump. However, the mechanical compressor is replaced by a thermal compressor consisting of an absorber, desorber, solution heat exchanger, expansion valve, and a pump. Figure 1.2 shows a schematic of a simple single-effect absorption system.

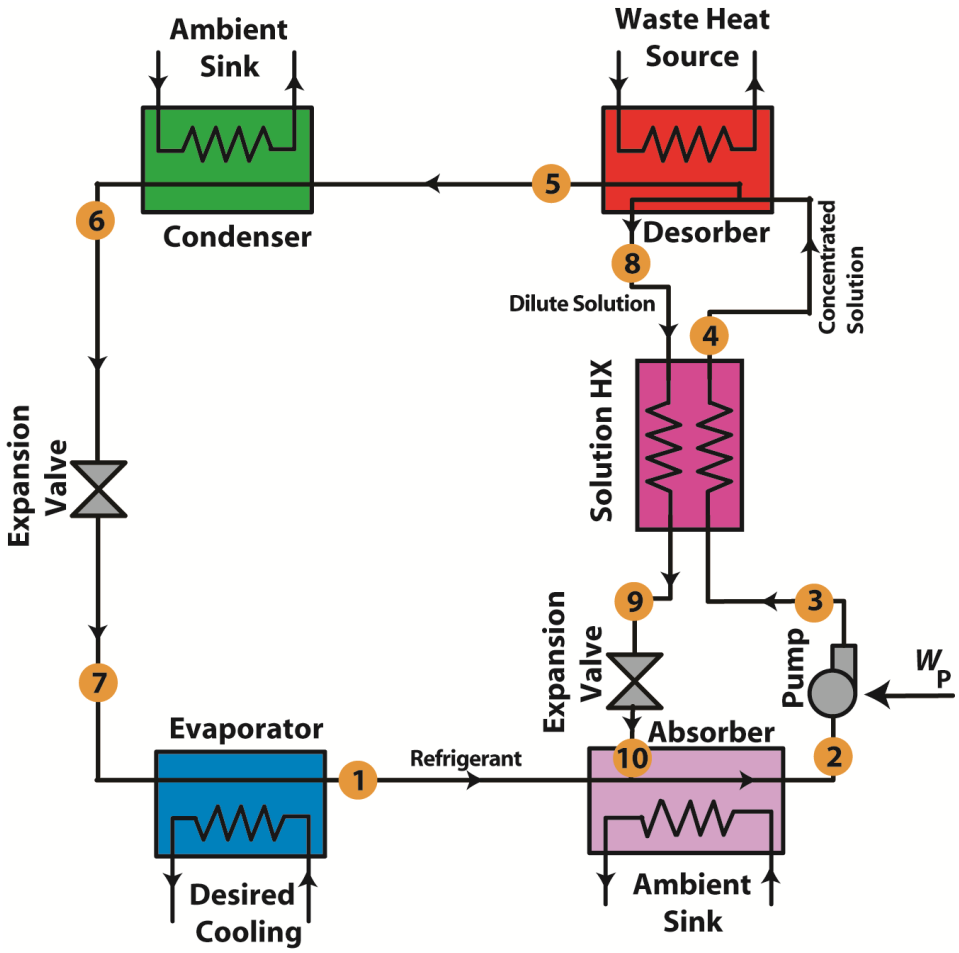

Figure 1.2 Absorption cycle

The refrigerant vapor leaves the evaporator at (1) and enters the absorber where the dilute solution flow is absorbed into the refrigerant as it is cooled, forming a concentrated solution of refrigerant and absorbent at (2). This absorption of the refrigerant into the absorbent releases a large quantity of heat Q_A, which must be rejected to the ambient. The concentrated solution is then pumped to the high-pressure side (3) and flows through the solution heat exchanger (SHX) on its way to the desorber, recuperating some of the heat, Q_{SHX}, from the concentrated solution stream, returning to the absorber from the desorber. The desorber is supplied with heat, Q_D, to separate the refrigerant stream (5) from the solution stream (4), leaving behind a dilute solution stream at (8).

However, absorption systems involve additional components that result in greater capital costs. The HVAC systems that are primarily sized for extreme weather conditions operate cyclically during mild weather conditions and thus, may experience multiple start-up and shut-down events. When installed in space conditioning application, the chiller must respond to continuously varying ambient conditions and changing cooling demands. Without adequate active system management, such transient operating conditions can lead to significant loss of performance, thus requiring the development of robust control strategies.

1.2 Working Fluids

The most common working fluid pairs used in absorption systems are lithium bromide-water and ammonia-water, which both have extremely low ODP and GWP values. On the contrary, the vapor compression systems have used refrigerants such as HCFCs. The ODP and GWP of refrigerants are summarized in Table 1.1 (Wang, 2001).

Refrigerants such as hydrofluorocarbons (HFC) do not appreciably affect the ozone layer

Table 1.1 Vapor-Compression Refrigerants (Wang, 2001)

Refrigerant	Application	Ozone Depletion Potential	Global Warming Potential
HCFC			
R-22	Residential and Commercial Refrigeration	0.05	0.34
HFC			
R-134a	Replacement for R-12	0.0	0.28
R-404a	Replacement for R-22	0.0	0.95
R-410a	Replacement for R-22	0.0	0.48
Inorganic Compounds			
R-717 (Ammonia)	Low Temperature Refrigeration/Absorption Refrigerant	0.0	0.0

but have a detrimental effect on environment due to their high global warming potential (GWP). The present study investigates absorption heat pumps using ammonia-water as the working fluid.

1.3 Need for controls in absorption systems

Absorption heat pumps used in residential and commercial applications encounter transient variations in operating conditions such as ambient temperatures, driving heat source temperatures and heating or cooling loads. Absorption heat pumps operating in buildings experience multiple start-up and shut-down cycles daily or hourly. Hence, if system performance is not controlled during these transients, low operating efficiencies will result for a significant portion of the run-time, leading to significant power losses. To minimize these losses and associated operating costs, it is critical to optimize the dynamic performance of the chiller. Such optimization becomes very challenging because of the two loops in the absorption heat pump (the refrigerant loop and absorbent loop) that both require multiple control variables such as the condenser and absorber fan speeds, two valve settings and pumping rate.

A robust control algorithm is needed during such start-up and shut-down operations, and would determine the optimal flow rates and valve settings for the given operating condition that maximizes the chiller performance. In general, controlling a vapor-absorption system is more difficult than controlling a vapor-compression system because two fluid loops in liquid and vapor phases at different species concentrations must be tracked, thus involving more parameters to be controlled. The development of such a control algorithm requires a thorough understanding of the transient behavior of the absorption system.

Figure 1.3 compares the potential coefficient of performance (COP) variation of an absorption system with and without controls.

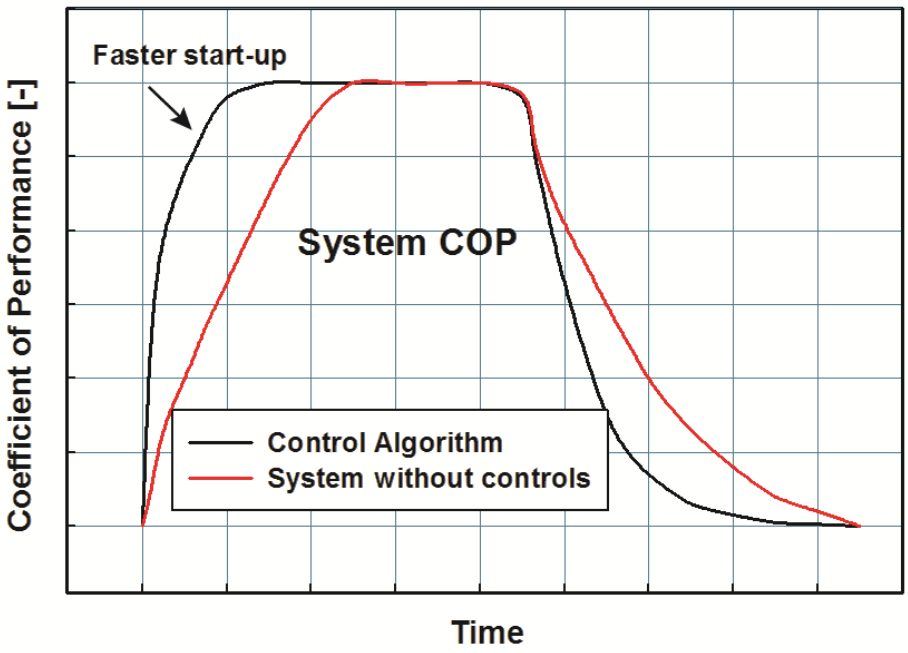

Figure 1.3 Potential COP vs. time for a representative absorption system

It can be inferred from Figure 1.3 that the system without controls takes longer to start-up and shut-down than the equivalent system with controls. In a hypothetical case, the start-up and shut-down times for a small-capacity system (1-3 RT) could be approximately 3-5 minutes, while the same for a higher capacity (10 RT) chiller could be ~15-20 minutes. For a real chiller encountering multiple start-up and shut-down cycles during the day, a lack of control could result in significant power losses, making system start-up a critical issue for absorption heat pumps. This is compounded by the fact that absorption systems are thermally driven, and a build-up of pressure in the high-side components is limited by component heat transfer rates. On the contrary, a vapor compression heat pump is electrically activated by a compressor, making pressurization of high-side components at system start-up relatively easier to achieve.

1.3.1 Parameters in absorption systems

The parameters of an absorption system can be classified as either design or run-time parameters. Design parameters include heat exchanger size, system charge, thermal energy storage of the heat exchangers, and others. Run-time parameters are the flow rates and temperatures of coupling fluids, mass flow rates of the working fluids, valve orifice diameters, and others. The design parameters influence how fast the system attains steady-state and also determine the level of steady-state performance. For example, one advantage of having larger heat exchangers is an increase in the cooling capacity of the chiller. But a larger system involves higher thermal mass and results in an increased start-up time. Run-time parameters determine the transient performance of the system during start-up and shut-down. For instance, if the valve setting is kept low enough during start-up, the refrigerant flow rate would also be low and result in a low pressure difference and lower evaporator load.

Because of the larger number of parameters indicated above, there is a need to understand how the system responds to each, and in general how the system behaves under different operating conditions. A thorough parametric study during steady-state and transient operation is first necessary before devising a control strategy for automated operation.

1.4 Need for dynamic model

Development of a control algorithm requires a thorough understanding of the transient behavior of the absorption system. As discussed earlier, control of a vapor-absorption system is more complex than that of a vapor-compression system.

Figure 1.4 shows a schematic of the role of a transient model in developing control strategies for the absorption chiller. The chiller usually has control devices such as thermostatic expansion valves, variable speed pumps and various temperature and pressure sensors that

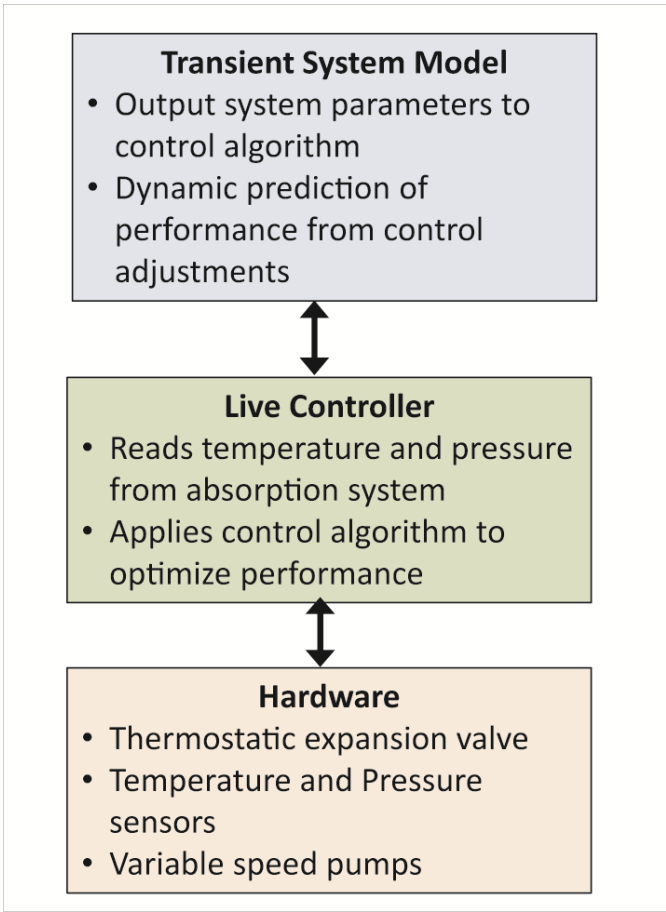

Figure 1.4 Potential role of transient model in devising a control algorithm

interact continuously with the live controller to implement the desired algorithm established in the controller. For example, a thermostatic valve can be used to modify the refrigerant flow rate based on the temperature glide in the evaporator. Thus, temperature sensors would measure the inlet and outlet temperatures of the evaporator to measure the evaporator temperature glide and then convey that information to the controller. The controller then modifies the valve opening to control the flow rate based on the inputs from the transient model. Thus, a control algorithm could be developed based on guidelines from the transient model. The transient model is the first step towards a robust control strategy, and understanding how different parameters such as flow rates, coupling fluid temperatures, volumes of components, etc. affect the performance of the

heat pump is imperative. An optimal choice of these parameters would result in improved performance during transient operations and also serve as a useful aid in the enhancement of steady-state performance.

1.5 Scope of this study

The present study focusses on the dynamic simulation of single-effect ammonia-water absorption heat pump. The model developed here uses a miniaturized absorption chiller developed by Determan and Garimella (2012) as the basis for implementation.

Most dynamic models in the past have studied the effect of a step change in one of the parameters governing the absorption system, whereas few have simulated the actual start-up process with typical changes in parameters. Furthermore, the miniaturized absorption heat pump under consideration is more difficult to model than other systems considered in the literature because such a miniaturized heat pump will react faster to transients due to a relatively small thermal mass. This makes it necessary to model heat and mass exchanger thermal masses in detail. A start-up process or any other transient event involves tracking of multiple parameters involved in the absorption system because they are inter-linked. The objective of the present study is to analyze the effect of various parameters including flow rates of the solution and coupling fluids, sizes of the heat exchangers, and ambient temperature that govern the performance of the absorption system.

1.5.1 Cause of system start-up transient

The system start-up transient is the result of transport delay of solution and refrigerant, gradual increase in component heat transfer rates due to thermal mass of solution and the heat exchanger wall and, the build-up of system pressures. The thermal masses of heat exchangers and energy storage in the fluids account for the heat transfer delay, which then delays reaching

steady-state. Also, the mass and species storage in the system is a cause for transport delay in the cycle. Therefore, the transient system model must account for these delays.

1.5.2 Objectives of the present study

The present study focusses on developing a dynamic model for a small-capacity absorption chiller, and will analyze the dynamics of absorption systems to formulate a transient model that can:

- Predict the start-up performance of an absorption heat pump from ambient conditions.
- Estimate the transient response of the heat pump to simulated step changes in the operating conditions.
- Make useful recommendations for the development of control strategies for the absorption chiller.

The purpose of this transient model is to predict the transient response of key parameters and to study how it affects the overall performance of the heat pump. It will serve as an aid in development of control strategies for the heat pump through control devices such as thermostatic valves or variable speed pumps.

1.6 Thesis organization

The organization of the thesis is as follows:

- Chapter 2 provides a brief review of the literature on dynamic modeling and control strategies for absorption heat pumps. It also lists potential simulation environments for dynamic modeling of absorption systems.
- Chapter 3 outlines the thermodynamic fundamentals and steady-state modeling of single-effect ammonia-water absorption systems.

- Chapter 4 describes the dynamic model formulation and the individual component models developed in this study.
- Chapter 5 presents dynamic performance results for the absorption chiller and system responses to different control strategies.
- Chapter 6 summarizes the conclusions from the transient model and provides recommendations for future work.

2. LITERATURE REVIEW

This chapter summarizes recent research on the dynamic behavior of absorption heat pumps, as well as on the simulation environments used in the past for dynamic modeling studies. This chapter is organized as follows:

- Section 2.1 contains a review of the dynamic models, testing and control strategies for analyzing the transient performance of an absorption heat pump
- Section 2.2 outlines the usefulness of different simulation environments for the dynamic modeling of absorption systems.
- Section 2.3 discusses the gaps in the literature and the scope of the present study.

2.1 Dynamic modeling and control strategies for absorption heat pumps

Some researchers have investigated the dynamic behavior of absorption heat pumps and used these dynamic studies to test control strategies for heat pump operation.

Kaushik *et al.* (1985) simulated the dynamic performance of an absorption heat pump driven by solar heat. Ammonia-water storage in the cycle was accounted for using two different storage tanks, namely condenser and absorber reservoirs downstream of the condenser and absorber, respectively. A high heat duty in the generator combined with low evaporator cooling duty resulted in excess refrigerant produced in the generator being stored in the condenser reservoir. On the other hand, a lower heat duty in the generator and higher cooling demand in the evaporator resulted in excess amount of refrigerant being drawn out of the condenser reservoir to meet the increased demand in the evaporator. As a result, the absorber reservoir downstream of the absorber was filled with excess solution. Thus, mass and species in the cycle were exchanged between the condenser and absorber reservoirs. Quasi-steady conditions were assumed in the heat exchanging components and storage in these components was neglected. Mass and species

storage in the cycle were modeled entirely in the storage tanks, and lumped capacity models were used to model the heat transfer in the remaining components. However, the quasi-steady assumption used in the evaluation of the overall heat and mass transfer would not be accurate in capturing the transient heat and mass transfer processes likely to occur in the miniaturized absorption system developed by Determan and Garimella (2012). The expansion valve model used in their study assumes that the amount of refrigerant required to meet the evaporator cooling demand is provided. Refrigerant flow based on the pressure difference between the high- and low- sides was not considered.

Butz and Stephan (1989) developed a dynamic model for an absorption heat pump and validated the model with an existing commercial heat pump. The investigated system employed a high-temperature (gas-fired) heat source, and used heat from a low-temperature water stream at 5-20°C to deliver heating power of 25 kW to a water stream at 30-50°C. A distributed parameter model was employed to model components such as the evaporator, condenser, refrigerant heat exchanger and solution-cooled absorber while a lumped capacity model was used to simplify other component models. Steady-state performance was first validated by comparing the temperature, pressure, and concentration values at different internal state points with experimental results. Dynamic response was also compared with the results of two separate experiments. The first experiment involved a step-change in the water inlet flow rate at the evaporator. The evaporator heat load remained unchanged while the water outlet temperature at the evaporator increased, thus confirming an increase in the heat transfer coefficient from an increase in the water flow rate. In the next experiment, they increased the water inlet temperature at the heat sink and observed a drop in the condenser heat duty and also an increase in the water outlet temperatures at the condenser and absorber. In a final experiment, they explored several

control strategies for the heat pump. They observed that intermittent burner cycling could cause significant energy losses. To mitigate these losses, they suggested the use of magnetic valves upstream of each internal throttle to prevent *pressure equalization* and internal *solution migration*. They also concluded that a continuous turn-down operation of the burner, coupled with a flow rate control where the solution flow is adjusted based on the heat demand would be an efficient control strategy. Alternately, they noted that maintaining a constant fluid level in the storage vessels during steady load operation, and varying the levels during transient loads to ensure optimal level at all times, was an effective strategy for stable performance. They also recommended that motor valves whose operation could be controlled by an increase or decrease of the voltage input to a linear step-up motor, be used instead of throttling valves to achieve better *fluid migration* and *separation of the two pressure vessels*, to achieve stable system performance.

Jeong *et al.* (1998) conducted a numerical study on the dynamic performance of a single-effect LiBr-H_2O absorption heat pump. Their work focused on upgrading 30-40°C heat, using a steam-driven absorption heat pump of 5000 kW heating capacity. A detailed parametric study was conducted to analyze the effects of flow rates, coupling fluid temperatures and heat exchanger areas on the system performance. It was found that increasing the driving steam temperature decreased the COP (for heating) of the heat pump although it increased its heating capacity. It was observed that an increase in the steam temperature increased the temperature of the components and made the heat transfer processes more irreversible. Furthermore, it increased the temperature of water at the condenser exit, and therefore, lowered the COP. Their study showed that an increase in the condenser coupling fluid temperature lowered the heating capacity, and left the COP unchanged. This was because reduced condensation due to lowered

coupling fluid temperature raised the high-side pressure and the desorber temperature, which in turn lowered the desorber heat load. Finally, an increase in the evaporator coupling fluid temperature increased both the heating capacity and COP of the heat pump. In their study, the flow rates of coupling fluids of the condenser and evaporator were varied separately. It was found that the heating capacity decreased with a decrease in the coupling fluid flow rate, while the COP remained unchanged. The decrease in the heating capacity was the result of reduced heat transfer coefficients that lowered the component heat duties. The effect of variation in overall heat transfer areas of individual components was also analyzed, and it was found that an increase in the heat transfer area improved the heating capacity of the heat pump and left the COP unaffected. However, an increase in the solution heat exchanger transfer area lowered the heating capacity, and increased the COP. Similarly, a decrease in the SHX heat transfer area reduced the COP drastically because of the exponential relation between the heat exchanger effectiveness and the heat transfer area. The results from their numerical study on intermittent system operation were compared with results from a practical operational heat pump, and it was found that even twelve minutes after the steam supply was shut off, the heat rejected by the absorber and condenser to the hot water coupling fluid was non-zero. During this time, the condenser duty decreased rapidly, while the absorber duty decreased slowly due to continuous vapor generation by evaporation of the refrigerant.

Fernández-Seara and Vázquez (2001) studied the effect of optimal generator temperature (OGT) in a single-stage ammonia-water absorption refrigeration system. A thorough parametric study was performed on the steady-state absorption cycle to determine COP and cooling load as a function of generator temperature for several cooling water temperatures. It was concluded that the OGT is a strong function of evaporator temperature, and condenser and absorber coupling

fluid temperatures. Assuming the evaporator was at a constant temperature, a linear relationship was deduced between the coolant temperature and OGT. Their control strategy was based on the assertion that at OGT, the system would perform at maximum COP irrespective of the thermal operating conditions. ON/OFF control was used for the refrigerant flow rate, using a temperature set point and difference range. In addition, the generator heat flux was controlled using a PID controller based on the error signal obtained between the OGT and the actual generator temperature, and the OGT was obtained from a specified coolant temperature.

Pérez de Viñaspre *et al.* (2004) studied the thermal behavior of a specific installation of a double-effect gas-fired H_2O/LiBr absorption chiller with a rated capacity of 352 kW. They studied the rates of energy distribution for different auxiliary components of the chiller unit. Air-handlers in five different rooms with cooling capacities between 34-93 kW were analyzed in the study. The average number of on/off cycles during the day was reported to be 36 and the operating time for each cycle was approximately five minutes. During 59% of the operation time, the chiller was in stand-by mode. An oversized chiller and a low cooling demand relative to the cooling capacity of the chiller were the prime reasons for the large number of on/off operations. The chiller was switched on when the chilled water temperature was between 7-10°C, and when the temperature fell outside this range, the chiller was switched to stand-by mode. Energy balance analyses showed that the air-handling units consumed 60% of the total power, followed by the fan coils (18%), and losses in pumps and lines accounted for the rest. The authors suggested the use of higher thermal inertia for the system through chilled water storage, and part-load operation as solutions to reduce the frequency of on/off operation.

Fu *et al.* (2006) developed the object-oriented simulation tool, ABSML (Absorption System Modeling Library) for dynamic absorption systems that incorporated different working

media and cycle configurations. A finite number of inter-connected control volumes were employed to simulate heat and mass transfer in the components. Steady-state momentum balance was used to relate pressure drop and mass flow rates between the control volumes. The start-up and shut-down behavior of several systems were analyzed with specific focus on an exhaust-driven double-effect $LiBr/H_2O$ chiller. A perturbation analysis of the chilled and cooling water temperatures, as well as exhaust gas flow rates, was performed around steady-state conditions. The predicted outlet temperatures of the chilled and cooling water were shown to match closely with the experimental values. The shut-down characteristics were analyzed by turning off the exhaust gas flow, solution pump and chilled and cooling water flows sequentially, to simulate a realistic shut-down process. The refrigeration capacity was non-zero for a significant period after the shut off of the exhaust gas, because the thermal mass of the heat exchangers maintained operation. However, the refrigerant and solution storage in the cycle were modeled primarily in the heat transfer components, and no specific device was incorporated to store any excess solution or refrigerant.

Kim and Park (2007) performed a numerical investigation of the dynamic behavior of a 10.5 kW single-effect ammonia-water absorption chiller. A lumped capacity approach was used to model the heat and mass transfer in the components and, a separated flow model was included to address the two-phase flow characteristics. The start-up time for the chiller was found to be nearly 1000 s and the time constant for achieving 67% of the chiller capacity was 409 s. Key system parameters such as bulk concentration, mass of ammonia-water solution, and volume of key components were varied, in a systematic parametric study. It was found that a higher bulk concentration resulted in a higher cooling capacity of the chiller and reduced the time constant. However, there was an optimal bulk concentration above which the chiller capacity was found to

decrease. It was concluded that low mass of the concentrated solution is favorable for achieving reduced time constants, even though a drop in the cooling capacity was observed. In general, an increased generator volume was shown to result in a higher cooling capacity, and reduced time constant. A step increase and subsequent decrease in the flue gas flow rate was tested, and it was found the time constant for chiller start-up could be reduced to 180 s. However, their model only considered thermal energy storage in the desorber, and the thermal masses of other components in the cycle were neglected. Furthermore, a lumped-capacity approach was employed, and each component was characterized by a single temperature value.

Kohlenbach and Ziegler (2008a) developed a dynamic model for a single-effect LiBr-H_2O system. The effects of transient behavior from mass storage in the absorber and desorber, thermal energy storage in all components, and a solution transport delay, were included in their model. Thermal storage was assumed in both the internal components and external coupling fluids. A transport delay was assumed to exist in the solution loop between the absorber and desorber, and in the refrigerant loop between the generator and evaporator. Their dynamic simulations were shown to match closely with experiments. The hot water inlet temperature for simulation was input from measurements on the absorption chiller. A 10 K step-change in the desorber coupling fluid temperature was investigated, while other external parameters were kept constant. The time taken for the hot water outlet temperature to attain steady-state was approximately 10 minutes, whereas the time for the system parameters to attain steady-state was close to 15 minutes. The steady-state results were shown to match with experimental results, although there was an observed delay of 10 s between experiments and dynamic simulation. Several factors were cited as reasons for this delay, such as the time-varying solution transport

delay, delay in the pipelines of coupling fluids, vapor storage in the vessels and solution storage in the tube bundles.

Kohlenbach and Ziegler (2008b) performed a numerical investigation using the dynamic model developed in Kohlenbach and Ziegler (2008a). The dynamic model was tested for its repeatability, sensitivity, and the model performance was validated with experimental results. The transient performance was studied from an existing steady-state (after 200 s) by increasing the desorber coupling fluid temperature by 10 K within 10 s, and then maintaining the temperature at its raised value for the rest of the time. Their numerical study was conducted for the system with zero thermal mass to reduce simulation time, and the transients were caused primarily by solution transport delay and mass storage in components. The step change was found to increase desorber vapor generation and cause an increase in system pressure. These factors contributed to the transient behavior of the chiller in terms of flow concentrations, system pressures, flow rates and heat loads. In the study, the external and internal thermal masses were varied, and the system response to a step change in the hot coupling fluid temperature was determined for each case. It was observed that the system with the lowest thermal mass responded the fastest, and also experienced the largest transient variations. Furthermore, an experimental validation was performed to compare the outlet temperatures of evaporator- and absorber-side coupling fluids. The values of the outlet temperatures were not accurately predicted by their simulation results due to the coarse nature of their thermodynamic model, although the dynamics were captured closely. There was an observed phase discrepancy of 10 s between experiments and dynamic simulation.

Marc *et al.* (2010) tested an installation of a 30 kW solar-driven H_2O/LiBr absorption chiller to provide space-conditioning without a back-up system. The chiller was tested in tropical

climatic conditions, and the limits of system operation without a set point temperature were explored. The limiting control was established using a set of pump and valve controls. For example, the solar pump was turned off when the solar-flux dropped below 100 W m^{-2} and the generator pump was turned on only when the hot and cold reservoirs reached temperatures of 80 ºC and 17 ºC, respectively. The transient start-up time, once the pumps were initiated, was reported to be 15 minutes. The work emphasized the need for a tighter control on energy consuming components, especially during part-load chiller operation, to save electrical power. The cooling tower fan was observed to contribute substantially to the power consumption. To decrease this power loss, an ON/OFF control that would operate based on the condenser water outlet temperature was suggested. Their control strategy needs further refinement to achieve better performance. It was concluded that a trade-off needed to be achieved between lower-chiller size, higher performance and optimal thermal comfort.

Matsushima *et al.* (2010) developed a dynamic simulation program using LiBr/H_2O as the working fluid to predict the transient behavior of absorption chillers with various configurations. They used a lumped-capacity approach for modeling the components and accounted for wall thermal mass. Their model assumed homogeneous mixtures of refrigerant or solution inside the components and approximated quasi-steady behavior of flows between components. Their program included an object-oriented formulation and a parallel processing architecture utilizing the Runge-Kutta-Gill method, with a new algorithm to estimate flow rate in a solution recirculation line. In their study, both cold and hot starts for the chiller were simulated where the cold-start analyzed start-up from ambient conditions and the hot-start analyzed chiller start-up from the existing steady-state. During cold-start, an initial LiBr concentration and temperature of 0.55 and 25°C, respectively, were assumed inside each component. For a double-

effect chiller configuration, the simulated variation in the evaporator cooling capacity, pressure and temperature of generator during start-up and shut-down was found to match closely with experiments. The same simulation tool was also used successfully to model a triple-effect absorption chiller with on-off operation.

Prasartkaew and Kumar (2010) simulated a 7 kW solar-biomass driven single-effect H_2O/LiBr chiller with the objective of evaluating the overall system performance on a daily and monthly basis. The biomass was utilized as a primary heat source at night and as an auxiliary heat source when solar energy was inadequate. The biomass burner was turned on when the hot water outlet temperature at the generator fell below a given set-point. Solar heating produced a constant hot water temperature during the daytime whereas the biomass-burner was switched on to heat the hot water tank at other times. During the evening transition from solar to biomass heating, the hot water temperature fluctuated close to the set-point resulting in a few on/off operations for the biomass boiler. The cooling capacity delivered by the chiller was found to increase during the day because of the higher heat transfer rates from solar heating, and decreases in the late evening due to a drop in the hot water temperature. It was observed that the average chiller COP stayed constant at 0.7, whereas the system COP decreased during daytime (solar heating) but remained unchanged at 0.69 when the biomass burner was activated (night time). The simulations were validated with experimental results from Syed *et al.* (2005) for a chiller capacity of 35 kW with the use of identical quarterly climactic conditions.

Cai *et al.* (2011) simulated the dynamic response of a single-effect ammonia-water absorption cycle to a step-change in the solution pump pressure rise. The thermodynamic properties of the mixture were estimated from the equation of state for mixtures. Mass, momentum and energy balances were conducted, and a lumped-capacity approach was used for

component modeling. The model was initially tested for its steady-state performance. It was observed that for a fixed temperature of the evaporator, absorber and condenser, the COP of the chiller decreased nearly linearly with increase in desorber temperature. The desorber heat load increased with an increase in the desorber temperature, whereas the evaporator duty was constant because of a fixed evaporator temperature, thus resulting in a lower COP at the higher desorber temperature. The dynamic response for 1% increase in the pressure difference across the pump showed that the heat loads and flow rates increased as expected and, as a result, the COP was increased. However, their simplified model assumed pure ammonia flow in the refrigerant loop, which may not be accurate enough for this simulation.

Monné *et al.* (2011) analyzed the performance of a solar powered absorption chiller installation using a detailed model in TRNSYS (Klein, 2006). The results from their study were validated with experiments, and showed a strong dependence of chiller COP on cooling water, chilled water, and generator driving temperatures. Furthermore, a new geothermal cooling system was proposed for heat rejection to improve chiller performance. A multi-regression fit was obtained based on experimental steady-state values of generator, condenser and evaporator temperatures. The numerical fit was used to relate the evaporator and generator heat loads with the evaporator, generator and condenser temperatures. Measured meteorological data were included in the model to match the simulation results with the results from the installation. The measured temperatures at the generator inlet and evaporator outlet, and the cooling capacity were compared with the results from simulation, on a given day of operation, and they were found to match well, with a maximum deviation of 11.8% observed in the cooling capacity, and 0 K deviation in the temperatures. Furthermore, the COP and cooling load of the installation were shown to decrease with an increase in ambient temperature. Finally, a new heat rejection system

was tested using a constant temperature water reservoir at 17°C as the heat sink, replacing the dry cooling tower, which used ambient air as the heat sink previously. The ambient air heat sink was found to be a less preferred option because the temperature of air varied between 20°C and 40°C, and thereby influenced the COP of the chiller during the course of the day. The TRNSYS model predicted a 42% increase in the COP while using the geothermal heat sink compared to the dry cooling tower case using ambient air as the heat sink.

Zinet *et al.* (2012) developed a dynamic model for single-effect H_2O/LiBr absorption chiller, delivering 15 kW of cooling. A customized falling-film evaporator-absorber was included, with mixed recirculation for the refrigerant and absorbent solutions. The condensation and refrigerant generation processes at the high-side utilized only a small fraction of the solution and absorbent flow in the cycle, while the major portion of the refrigerant and absorbent was re-circulated through the evaporator-absorber into their respective loops. The heat and mass transfer interactions in the absorber and desorber were modeled extensively using Nusselt's film theory, but the single-phase heat exchangers were modeled using the simplified NTU-effectiveness method. The chiller response time to a step reduction in the heated coupling fluid flow rate was reported to be 100 s. The chiller response time was underestimated due to transport delays, and delay times associated with the state-change propagation through the refrigerant and solution loops. Their model also captured the chiller response to a step-reduction in the chilled water inlet temperature, utilizing a thermostat to control the auxiliary circuit fluid flow rate.

Table 2.1 presents a summary of relevant literature on dynamic modeling and control strategies for absorption heat pumps.

Table 2.1 Summary of relevant literature

Author(s) (Year)	Working Fluid	Capacity	Driving Heat Source	Notes
Kaushik *et al.* (1985)	NH_3/H_2O	4 kW	Solar heat	• Ammonia-water storage estimated from condenser and absorber reservoirs • Quasi-steady assumptions in heat exchanger models • Constant flow rate expansion valve used
Butz and Stephan (1989)	NH_3/H_2O	8.57 kW	Gas burner	• Step increase in evaporator coupling fluid flow rate: Evaporator cooling duty unchanged and coupling fluid outlet temperature increased • Step increase in condenser inlet coupling fluid temperature: Condenser duty decreased and coupling fluid outlet temperature increased • Energy losses during intermittent burner cycling • *Control strategy:* Continuous burner turn down, solution pumping rate control and use of magnetic valves
Jeong *et al.* (1998)	$LiBr/H_2O$	5000 kW	Steam	• *Parameters*: Heat exchanger areas, coupling fluid flow rates and temperatures • *Outputs*: Trends in COP and heating capacity variation for different parameters • Non-zero heat loads in condenser and absorber observed for 30 minutes after shut-off of steam supply
Fernández-Seara and Vázquez (2001)	NH_3/H_2O	5 kW	Heated coupling fluid	• Obtained COP and cooling load as a function of generator temperature for different cooling water temperatures • Strong dependence of Optimal Generator Temperature (OGT) on cooling water and evaporator temperatures; Maximum COP observed at OGT • OGT increased linearly with cooling water temperature for a fixed evaporator temperature • *Recommendations*: Refrigerant flow rate control using temperature set point and generator flux control using PID controller

Table 2.1 (continued)

Author(s) (Year)	Working Fluid	Capacity	Driving Heat Source	Notes
Pérez de Viñaspre *et al.* (2004)	$LiBr/H_2O$	352 kW	Gas fired	• Oversized chiller and low cooling demand caused chiller standby mode • *Control strategy*: Switch on chiller when chilled water temperature varies between 7-10°C and switch off at other times • Average daily capacity of 68 kW (19% nominal capacity) ; Oversized chiller led to frequent on/off operations • Power consumption: Air-handling units (60%), fan coils (18%) and pumps (22%) • *Recommendations*: Increased thermal inertia through chilled water storage and part-load operation to reduce number of on/off cycles
Fu *et al.* (2006)	$LiBr/H_2O$, $NH3/H_2O$	Not specified	Exhaust	• Developed ABSML (Absorption System Modeling Library); Can incorporate different cycle configurations and working fluids • Perturbed evaporator and condenser coupling fluid temperatures to investigate start-up; Outlet temperature variation shown to match experimental results • Non-zero normalized refrigeration capacity after exhaust gas turn-off due to heat exchanger thermal mass
Kim and Park (2007)	NH_3/H_2O	10.5 kW	Flue gas	• Chiller start-up time - 1000 s; Time-constant - 409 s • *Parameters varied*: Bulk concentration, solution mass and generator volume; Studied effect on time constant and cooling capacity • *Control strategy:* Step increase in flue gas flow rate for 300 s followed by step reduction - Shown to minimize time constant to less than 180 s • Considered wall thermal mass only for desorber

Table 2.1 (continued)

Author(s) (Year)	Working Fluid	Capacity	Driving Heat Source	Notes
Kohlenbach and Ziegler (2008a)	LiBr/H_2O	10 kW	Hot water	• Accounted for fluid thermal masses (internal and coupling fluid), solution storage in desorber and absorber, refrigerant and solution transport delays • 10 s delay in absorber coupling fluid temperature between experiments and simulation results; Delay in pipelines, vapor storage in vessels, solution storage in bundles and coarse thermodynamic model cited as reasons for delay
Kohlenbach and Ziegler (2008b)	LiBr/H_2O	10 kW	Hot water	• Parametric studies using Kohlenbach and Ziegler (2008a) model • 10 K linear increase in desorber coupling fluid temperature increased vapor generation, pressure rise and increased solution transport delay • System with least thermal mass responded the quickest, but experienced largest transient variations
Marc *et al.* (2010)	LiBr/H_2O	30 kW	Solar heat	• Pump and valve controls investigated • *Start up*: Turn on generator pump followed by solution and other coupling fluid pumps; Turn on generator pump if hot reservoir temperature above 80°C and cold reservoir temperature below 17°C • Start-up time: 15 minutes since pumps were turned on • Power losses mainly due to cooling tower fan • *Control strategy*: Switch on cooling tower fan when condenser coupling fluid outlet temperature reaches 38°C and switch off when temperature falls below 33°C

Table 2.1 (continued)

Author(s) (Year)	Working Fluid	Capacity	Driving Heat Source	Notes
Matsushima *et al.* (2010)	$LiBr/H_2O$	141 kW	Gas/oil/fuel	• Assumed homogeneous mixture of refrigerant/solution inside components and quasi-steady behavior for flows between components; Object oriented formulation and parallel processing architecture employed • Hot start (start from previous steady-state) and cold start (start up from 25°C) behavior investigated • Evaporator cooling capacity, pressure and temperature results from simulation align with experimental results
Prasartkaew and Kumar (2010)	$LiBr/H_2O$	7 kW	Solar/Biomass	• Used solar energy during daytime and biomass during night and low sunshine times to drive chiller; • Biomass burner turned on when desorber coupling fluid outlet temperature was below 83°C • ON/OFF operation during transition from solar to biomass burner • Cooling capacity increased during daytime due to higher heat transfer rates and decreased during evening times because of reduced hot water temperature; COP stayed at 0.7 during operation
Cai *et al.* (2011)	NH_3/H_2O	320 kW	High temperature source	• Thermodynamic properties of ammonia-water estimated from equation of state • 1 % step increase in the pressure rise across the solution pump increased cooling capacity, refrigerant flow rate and COP rapidly; Time to reach steady state: 60 s

Table 2.1 (Continued)

Author(s) (Year)	Working Fluid	Capacity	Driving Heat Source	Notes
Monné *et al.* (2011)	LiBr/H_2O	4.5 kW	Solar power	• Temperatures from experiments matched TRNSYS simulation results; Maximum deviation of 11.8% in cooling capacity • Cooling capacity and COP decreased with increase in ambient temperature • Geothermal heat sink proposed to replace dry cooling tower to improve COP • TRNSYS model predicted 42% increase in COP using geothermal heat sink
Zinet *et al.* (2012)	LiBr/H_2O	15 kW	Waste heat and an auxiliary source	• Investigated system responses to step reduction in heat recovery fluid flow rate and chilled water flow rate; Chiller response time - 100 s • Chiller response time under-estimated due to transport delays and delay between refrigerant and solution loops • Investigated step reduction in chilled water inlet temperature; Desorber coupling fluid flow rate controlled based on chilled water outlet temperature; Time to reach steady-state - 300 s

2.2 Potential simulation platforms

This section outlines the advantages and disadvantages of different software platforms for the development of transient models for absorption systems.

2.2.1 MATLAB

- Matlab® (MathWorks, 2010) is a general purpose computing environment and is intended for algorithm/numerical methods prototyping and development.
- Matlab was employed by Kohlenbach and Ziegler (2008a, b) for the transient modeling of a physical single-effect LiBr/H_2O chiller. They used Matlab to solve the system of governing equations and employed the Newton-Raphson technique along with finite difference approximation.
- Matlab requires manual implementation of a nonlinear solver or choice of nonlinear solver that has already been implemented.
- Thermodynamic and transport property routines necessary for estimating thermodynamic properties of ammonia-water mixtures are required prior to the development of a transient absorption system model.

2.2.2 Simulink

- Simulink® (MathWorks, 2010) is a Matlab tool intended for simulation of signal processing, transient systems, and control systems.
- Simulink was employed by Nielsen *et al.* (2009) to perform a detailed transient heat exchanger model. Also, Bittanti *et al.* (2010) have used it to model the transient performance of an absorption chiller for air-conditioning applications.
- It is limited to a subset of Matlab programming language (embedded Matlab) and basic component blocks (multipliers, delays, adders, differentiators, and others)

and is a rigid programming paradigm. However, it has features such as time-varying input signals, in-built controllers, variable time-step solvers, and others, which are useful in transient model development and for the testing of control strategies.

- Models are generally configured in a "flow-chart" GUI. Also, Simulink has the functionality to import components specified in M-Code or C. This feature is more critical in Simulink because the thermal system components are not packaged with the program.
- Simulink supports modular programming allowing sub-models of increasing complexity to be built inside the main model. It supports model reusability, which can be useful for constructing similar component structures in the main model.

2.2.3 EES

- Engineering Equation Solver (EES) developed by Klein (2010) is a general purpose non-linear equation solver.
- It is used extensively for steady-state cycle models, but has not been widely used in the past for transient simulations because it is not designed for time-marching/integration with systems that include multiple state points (integration variable limits, total variable count limits, and others).
- A simple unsteady cycle/controls system model can be tested in EES. However, complexities such as user-defined inputs, storage of long simulation runs and adaptive time-stepping are not easy to implement.

2.2.4 TRNSYS

- TRNSYS (Klein, 2006) is a transient modeling software tool which uses ammonia-water properties from Ziegler and Trepp (1984).
- Pre-defined components can be selected from a large library, and placed on the user interface. Inputs and outputs are connected as in a familiar flow-chart. It has a number of built-in thermal system components.
- TRNSYS includes a number of components such as PID controllers and adaptive controllers that can be used directly in the control system model. Additionally, it has the capability to import a more sophisticated control code developed in other environments such as EES, Fortran or Matlab.
- The default thermal components in TRNSYS can handle single component/single-phase fluids and assume constant density and specific heats. However, a transient start-up process with ammonia-water would involve varying densities of fluids based on the pressure and temperature at different instants. Thus, the built-in thermal system components in TRNSYS are not appropriate for modeling the transients in an absorption chiller.

2.2.5 ABSML

- The Absorption System Modeling Library was developed by Fu *et al.* (2006) for modeling a wide range of absorption systems based on different working fluids for many different cycle configurations.
- Fu *et al.* (2006) modeled a LiBr/H_2O system using ABSML, and good agreement was found with experimental results (absolute temperature errors less than 0.5 K) under perturbed coupling fluid temperatures during startup and shut down.

- ABSML is not commercially available and software help files are limited.

Table 2.2 summarizes the advantages and disadvantages of different modeling environments for dynamic absorption. Based on the above mentioned features, Matlab/Simulink is chosen as the best modeling environment for the present study. The component models are

Table 2.2 Summary of simulation platforms for dynamic absorption

Software	Utility	Advantages for dynamic simulation	Limitations
Matlab	• General computing tasks • Algorithm/numerical methods prototyping and development	• Used to develop dynamic model for an absorption chiller (Kohlenbach and Ziegler, 2008a, b); governing equations solved using Newton-Raphson technique/ finite difference	• Manual implementation of non-linear solver required • Development of thermodynamic and transport property routines prior to dynamic model
Simulink	• Matlab tool • Simulation of signal processing, dynamical modeling and control systems	• Flow-chart based GUI configuration • Can import components specified in M-code or C • *Features:* Variable time steps, time dependent input signals, PID controls • Modular programming environment • Model reusability for replicating component models • Used for dynamic modeling of absorption systems and heat exchanger models (Nielsen *et al.*, 2009; Bittanti *et al.*, 2010)	• Basic component blocks (multipliers, differentiators, adders, and others) • Rigid programming paradigm
EES	• General purpose non-linear equation solver	• Useful for steady-state thermodynamic cycle models • Contains built-in thermodynamic property routines • Useful for testing simple unsteady cycle/ controls system model	• Not ideal for transient computations • Not designed for time-marching/integration with systems involving multiple-state points • Integration variable limits and total variable count limits • User-defined inputs, storage of long simulation runs and adaptive time-stepping not supported

Table 2.2 (Continued)

Software	Utility	Advantages for dynamic simulation	Limitations
TRNSYS	• Transient modeling software tool • Large library of thermal system component choices	• Built-in thermal system components • Configured in a "flow-chart" GUI • Can use PID controllers and adaptive controllers directly in control system model • Can import sophisticated control code developed in EES, Fortran or Matlab	• In-built components can handle only single component/single phase fluids; Constant density and specific heats assumed ; May not be ideal for modeling ammonia-water absorption systems
ABSML	• Absorption System Modeling Library used for modeling absorption systems	• ABSML used by Fu *et al.* (2006) to model LiBr/H_2O system • Wide range of property libraries, working fluids and cycle configurations (single-effect, double-effect triple-effect, and others) supported	• Not commercially available • Access to software help files limited

developed from scratch in Simulink, and, the ammonia-water property routines developed by Rattner and Garimella (in preparation, 2013) are invoked in each component model at different time steps.

2.3 Need for further research

To date, most studies have relied on lumped-capacity assumptions for components. However, temperature variation inside the components may be significant, especially during transient operation from thermal transport delays or large temperature glides. To resolve such phenomena in detail, segmented models are employed for heat and mass exchanging components.The thermal storage capacity of individual components affects the transient behavior of the system significantly, and must be accounted for to achieve accurate results. Also, while many studies have modeled the pressure difference across system components using momentum

balances, few have accounted for the transient pressure variations driven by mass accumulation in the system storage devices that have a much larger influence on system behavior. In a system with miniaturized heat and mass exchangers, the solution and refrigerant storage tanks account for the major portion of the fluid inventory. Thus, vapor-liquid equilibrium conditions in these components control system pressures. Accurate models for high- and low-side pressure variations are required for predicting flow rates and overall system behavior. The robust and detailed model developed in the present study and described in the subsequent chapters will enable simulation of the entire start-up and shut-down processes, not only responses to step changes in a single parameter.

3. THERMODYNAMIC FUNDAMENTALS AND STEADY-STATE MODEL

This chapter provides the necessary background on ammonia-water absorption heat pumps. A general introduction to heat pumps and computation of their performance is presented. Subsequently, a brief introduction of the steady-state modeling of the heat exchangers is summarized.

The steady-state analysis was performed using *Engineering Equation Solver* (EES) software (Klein, 2010). The thermodynamic fundamentals summarized in this chapter form the basis for the development of the transient model (Chapter 4). The steady-state performance of the absorption heat pump is used for comparison with the results from transient model (Chapter 5).

3.1 Introduction

A heat pump is a device that transfers heat from a low temperature to a high temperature. A heat pump can be used to heat or cool a space, depending on whether it is functioning in the heating or cooling mode, and such a transfer of heat requires a thermodynamic input in the form of either heat or work.

The performance of a heat pump is evaluated using the Coefficient of Performance (COP). The COP is defined as the ratio of the desired heat transfer to the amount of energy required to provide that desired heat transfer. The desired heat transfer includes the heat removed from the conditioned space (cooling mode), or the heat supplied at the high temperature heated space (heating mode). The energy required can include net work input (vapor compression) or the heat input (absorption).

3.2 Overview of heat exchangers

This section describes the steady-state modeling procedures used to predict the performance of heat exchangers in the absorption system. First, this section discusses the heat exchanger energy balance, and then introduces Log-Mean Temperature Difference and effectiveness-NTU methods for assessing heat exchanger performance.

A heat exchanger is a device that transfers heat from one fluid to another. The absorption heat pump under consideration in this study uses microchannel plate heat exchangers that consist of many stacked plates. According to Nellis and Klein (2009), such plate heat exchangers offer several advantages such as compactness, and the ability to size the system for different capacities by adding and removing the plates.

3.2.1 Energy Balances

Following the analysis in Incropera and DeWitt (1996), several assumptions are used in setting up the overall energy balance for a heat exchanger:

- The heat exchanger is insulated from its surroundings and thus, the only heat exchange takes place between hot and cold fluids.
- Axial conduction along the tubes is negligible
- Potential and kinetic energy changes are negligible
- The fluid specific heats are constant
- The overall heat transfer coefficient is constant

A counterflow heat exchanger, similar to some of the heat exchanger configurations used in the present study, is shown in Figure 3.1. The hot fluid enters at a mean temperature of $T_{H,in}$ and leaves at a mean temperature of $T_{H,out}$. The cold fluid flows in the opposite direction, entering at a mean temperature of $T_{C,in}$ and leaving at a temperature of $T_{C,out}$.

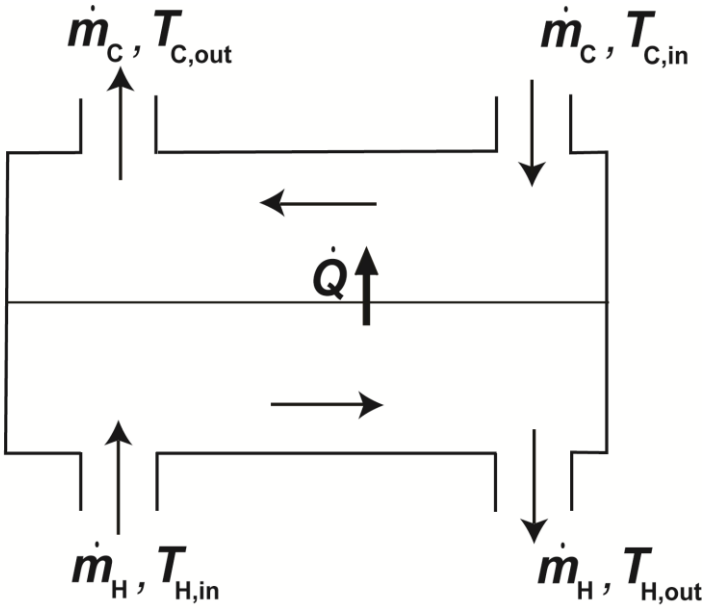

Figure 3.1 Schematic of a counterflow heat exchanger

The specific heat capacity for most fluids is a function of temperature. However, the specific heat capacity variation for each stream within single-phase heat exchangers is typically small. A representative average value is used to simplify the heat exchanger model, reducing the overall energy balance to Equation (3.1).

$$\dot{m}_H c_H (T_{H,in} - T_{H,out}) = \dot{m}_C c_C (T_{C,out} - T_{C,in}) \tag{4.1}$$

The rate of heat transfer from the hot fluid to the cold fluid can be determined from an energy balance on either the cold or the hot stream side, and is shown in Equation (3.2).

$$\dot{Q} = \dot{m}_H c_H (T_{H,in} - T_{H,out}) = \dot{m}_C c_C (T_{C,out} - T_{C,in}) \tag{4.2}$$

The closest approach temperature (CAT) is defined as the difference between the coupling fluid temperature and the working fluid temperature at the inlet or outlet, as applicable, and is an indication of the effectiveness of the heat exchanger to transfer heat.

3.2.2 Log-Mean Temperature Difference (LMTD) Method

The LMTD method calculates the heat transfer between the two fluid streams in a heat exchanger as the product of a log-mean temperature difference, ΔT_{lm}, and *UA* (Nellis and Klein, 2009):

$$\dot{Q} = UA\Delta T_{lm} \tag{4.3}$$

The log-mean temperature difference for a counterflow heat exchanger is defined by Nellis and Klein (2009) as:

$$\Delta T_{lm} = \frac{(T_{H,out} - T_{C,in}) - (T_{H,in} - T_{C,out})}{\ln[\frac{(T_{H,out} - T_{C,in})}{(T_{H,in} - T_{C,out})}]} \tag{4.4}$$

The UA-LMTD method is valid for heat exchangers where the capacity rate ($\dot{m}c_p$) of the two fluid streams are constant along the length of the heat exchanger. The method is not strictly valid for ammonia-water streams, especially in heat exchangers with phase change, but the method can still be used to provide useful approximations.

In cycle modeling calculations, estimates of desired CAT are used to obtain system and component state points, which in turn allow the estimation of component-specific UA values required to achieve those state points. The resulting UA values are then used as component specifications for the baseline configuration of the system and are fixed for further calculations. These baseline values for the absorption cycle are presented in Table 3.1.

Table 3.1 Baseline conditions for single-effect ammonia-water absorption cycle

	Description	Parameter	Value	Units
General Settings	Refrigerant	NH_3/H_2O	-	-
	Ambient Temperature	T_{amb}	35	°C
	Cooling capacity	$\dot{Q}_{evap}$	3.54	kW (1 RT)
	Pump efficiency	η_{pump}	0.65	-
Solution and coupling fluid data	Solution flow rate	$\dot{m}_{conc,des,in}$	0.00975	kg s^{-1}
	Desorber coupling fluid (Paratherm™)	$\dot{m}_{des,cf}$	0.084	kg s^{-1}
		$c_{p,cf,des}$	2.54	kJ kg^{-1} K^{-1}
	Condenser coupling fluid (25% Propylene Glycol/water mixture)	$\dot{m}_{cond,cf}$	0.112	kg s^{-1}
		$c_{p,cf,cond}$	3.993	kJ kg^{-1} K^{-1}
	Absorber coupling fluid (25% Propylene Glycol/water mixture)	$\dot{m}_{abs,cf}$	0.112	kg s^{-1}
		$c_{p,cf,abs}$	3.993	kJ kg^{-1} K^{-1}
	Evaporator coupling fluid (25% Propylene Glycol/water mixture)	$c_{p,cf,evap}$	3.97	kJ kg^{-1} K^{-1}
		$\dot{m}_{evap,cf}$	0.16	kg s^{-1}
UA-values	Absorber	ABS	0.58	kW K^{-1}
	Solution Heat Exchanger	SHX	0.18	kW K^{-1}
	Desorber	DES	0.149	kW K^{-1}
	Rectifier	REC	0.0284	kW K^{-1}
	Condenser	CON	0.565	kW K^{-1}
	Refrigerant Heat Exchanger	RHX	0.06	kW K^{-1}
	Evaporator	EVAP	0.86	kW K^{-1}
Effectiveness	Solution heat exchanger	SHX	0.97	-
	Refrigerant heat exchanger	RHX	0.97	-

3.2.3 Effectiveness-NTU method

The steady-state model developed in this study uses the effectiveness-NTU (ε-NTU) method to calculate the parameters of the solution heat exchanger and the refrigerant heat exchanger. The effectiveness-NTU method is algebraically identical to the LMTD method; both methods represent different presentations of the same information, with the UA-LMTD method being more suitable for design, and the ε-NTU being more suitable for the prediction of the performance of a heat exchanger that has already been designed.

Heat exchanger effectiveness is defined as the ratio of the actual heat transfer rate ($\dot{Q}_{act}$) to the maximum possible heat transfer ($\dot{Q}_{max}$) rate for the given inlet conditions:

$$\varepsilon = \frac{\dot{Q}_{act}}{\dot{Q}_{max}} \tag{4.5}$$

For a representative case with the cold fluid having a lower heat capacity than the hot fluid, an alternate way to express this relationship is to use the respective temperatures, as shown in Equation (3.6). Figure 3.2 represents the T-x diagram of a simple counterflow heat exchanger, showing the hot and cold fluids. The cold fluid is assumed to have a lower heat capacity compared to the hot fluid.

$$\varepsilon = \frac{(\dot{m}c_p)_{min}(T_{C,out} - T_{C,in})}{(\dot{m}c_p)_{min}(T_{H,in} - T_{C,in})} \tag{4.6}$$

The effectivenesses for both the refrigerant pre cooler and the solution heat exchanger are assumed to be 0.97 in this analysis of the baseline case.

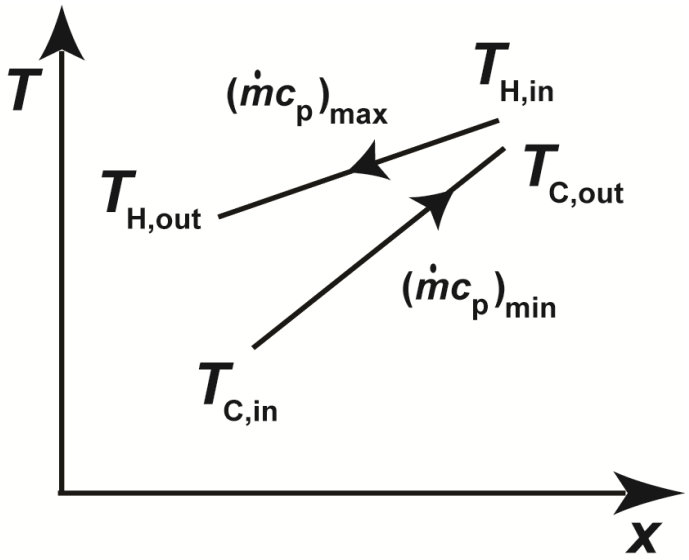

Figure 3.2 T-x diagram of the heat exchanger

3.3 Single-effect ammonia-water absorption cycle

The steady-state modeling procedure for the single-effect ammonia-water absorption cycle is based on the investigations of Determan and Garimella (2012), who demonstrated the feasibility of fabricating and operating a monolithic micro-scale absorption heat pump.

3.3.1 System overview

A schematic of the single-effect ammonia-water absorption cycle is shown in Figure 3.3. Concentrated ammonia-water solution leaves the absorber (1) and is pumped to the high-side via the solution-cooled rectifier and the solution heat exchanger, thus recuperating the heat rejected by these components. This pre-heated ammonia-water solution enters the desorber (5) and is heated by a waste heat stream. The heat transferred in the desorber ($\dot{Q}_{DES}$) is used to vaporize and separate the ammonia from the ammonia-water liquid mixture. After separation, the vapor enters the rectifier (6) and the dilute solution returns to the solution heat exchanger (7). The solution-cooled rectifier is used to increase the concentration of ammonia vapor by condensing

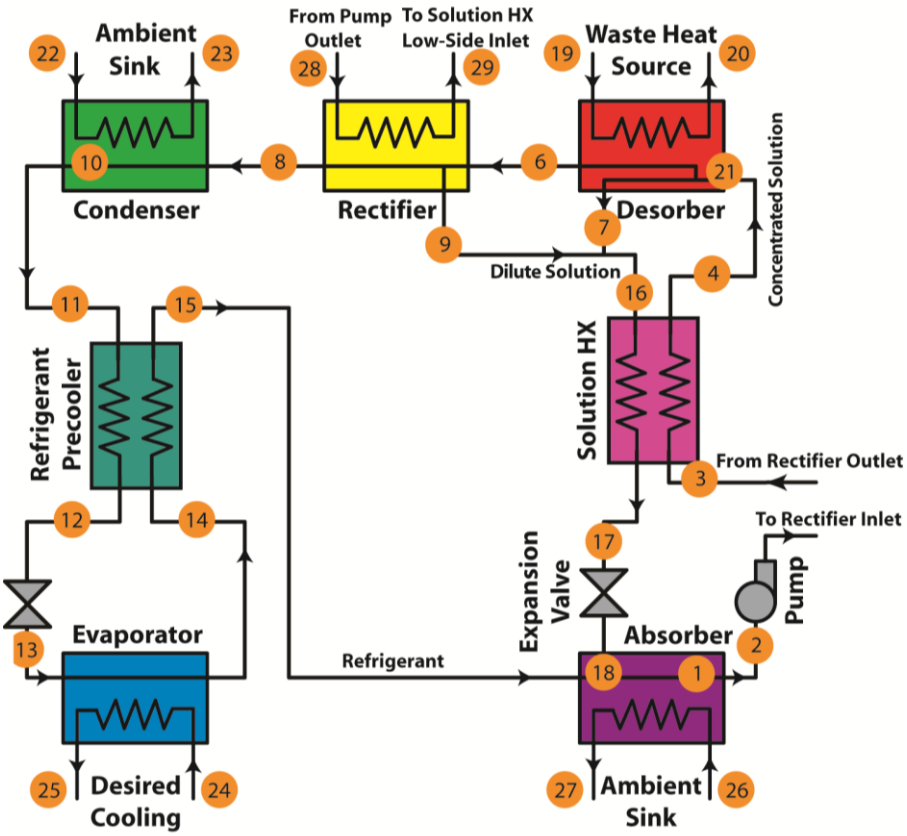

Figure 3.3 Schematic of absorption cycle

the water fraction, and the low concentration reflux (9) is directed towards the solution heat exchanger, enabling it to mix with the dilute solution exiting the desorber (16) where it pre-heats the concentrated solution flowing to the desorber. Finally, the dilute solution returns to the absorber (18) operating at the low-side pressure through an expansion valve (17).

The enriched ammonia-vapor exits the rectifier and enters the condenser (8). The ammonia vapor rejects heat to the ambient in the condenser and exits as a liquid refrigerant (11) to the refrigerant heat exchanger. In the refrigerant heat exchanger, it rejects heat to the refrigerant vapor from the evaporator and enters the expansion valve (12). Upon expansion to the low-side pressure, it enters the evaporator as a two-phase mixture (13).

Inside the evaporator, heat from the conditioned space $\dot{Q}_{EVAP}$, is removed to produce the desired cooling effect. This heat boils the refrigerant, which exits the evaporator mostly as vapor (14), and enters the refrigerant heat exchanger where it is further heated to result in a higher temperature refrigerant vapor phase at low-pressure (15). This refrigerant enters the absorber, mixing adiabatically with the returning dilute solution (18).

During the absorption process, the ammonia vapor releases a large amount of heat $\dot{Q}_{ABS}$ that must be rejected to the ambient. The vapor is then absorbed into the liquid solution (1) to complete the cycle.

3.3.2 Steady-state modeling procedure

The steady-state modeling procedure for each internal component of absorption chiller is discussed in this section. The procedure is based on the dissertation of Determan and Garimella (2012), and the baseline conditions are summarized in Table 3.1, and are based on Air-Conditioning and Refrigeration Institute (ARI) standard rating conditions. The design point chosen for the sample calculation is a heat sink temperature of 35°C and a cooling capacity of 3.54 kW. For the design point calculation, the pumping rate of the concentrated solution is chosen as 0.00975 kg s^{-1}. Other design parameters are summarized in Table 3.1.

Desorber and rectifier

Typical concentrations of refrigerant exiting the desorber are high (~ 0.85 - 0.95), but even these high concentrations are detrimental to overall cooling capacity and performance of the chiller because of the rise in temperature experienced by the ammonia-water mixture as it evaporates, requiring that ammonia concentration be enriched further. Therefore, the rectifier is employed to increase the concentration to the desired nominal concentration at the outlet of the rectifier of 0.9985. Figure 3.4 represents the control volume of the rectifier. It shows the

refrigerant vapor cooled by the concentrated solution. Refrigerant with higher ammonia-concentration, and heated concentrated solution exit the rectifier on the refrigerant and solution sides respectively. The liquid reflux is condensed out of the refrigerant stream, and is collected

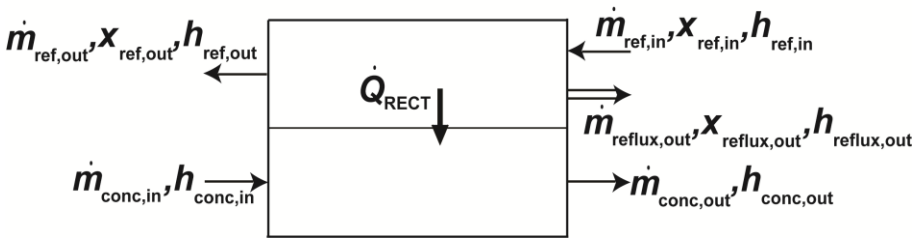

Figure 3.4 Rectifier control volume

in the separation chamber. An energy balance on the rectifier yields the outlet enthalpy of the concentrated solution.

$$\begin{aligned} \dot{Q}_{\text{RECT}} &= \dot{m}_{\text{ref,out}} \cdot h_{\text{ref,out}} + \dot{m}_{\text{reflux,out}} \cdot h_{\text{reflux,out}} - \dot{m}_{\text{ref,in}} \cdot h_{\text{ref,in}} \\ \dot{Q}_{\text{RECT}} &= \dot{m}_{\text{conc,out}} \cdot h_{\text{conc,out}} - \dot{m}_{\text{conc,in}} \cdot h_{\text{conc,in}} \end{aligned} \tag{4.7}$$

The enthalpy of the concentrated solution at inlet and outlet of rectifier are estimated to be -51.96 kJ kg^{-1} and 45.34 kJ kg^{-1} respectively. The enthalpy of the refrigerant at the inlet and outlet of the rectifier are 1533 kJ kg^{-1} and 1333 kJ kg^{-1} respectively, whereas the enthalpy of the liquid reflux at the outlet is found to be 266.1 kJ kg^{-1}. The rectifier heat transfer rate is estimated to be 0.9486 kW.

The corresponding mass and species balances are shown in Equations (3.8) and (3.9).

$$\dot{m}_{\text{ref,in}} = \dot{m}_{\text{ref,out}} + \dot{m}_{\text{reflux,out}} \tag{4.8}$$

$$\dot{m}_{\text{ref,in}} x_{\text{ref,in}} = \dot{m}_{\text{ref,out}} x_{\text{ref,out}} + \dot{m}_{\text{reflux,out}} x_{\text{reflux,out}} \tag{4.9}$$

For the sample point, the concentrated solution flow rate is set to 0.00975 kg s^{-1}. The liquid reflux is assumed to be a saturated liquid in thermal equilibrium with the incoming

refrigerant vapor, and hence its ammonia concentration is estimated to be 0.4249 from a known high-side pressure (2092 kPa) and incoming refrigerant vapor temperature (113.1°C). The refrigerant flow rates at inlet and outlet are estimated to be 0.00335 kg s^{-1} and 0.00309 kg s^{-1} respectively, and that of the liquid reflux is 0.00026 kg s^{-1}. The ammonia concentration of refrigerant at the inlet is known from known desorber outlet conditions to be 0.9535, and the vapor outlet concentration is fixed at 0.9985.

Figure 3.5 represents the control volume of the desorber. Heat transfer between the coupling fluid and solution is used to separate the refrigerant vapor from the solution. The reflux from the rectifier mixes with the concentrated solution entering the desorber. The dilute solution exits the bottom of the desorber and enters the solution heat exchanger. The mass and species balances are carried out inside the desorber.

$$\dot{m}_{\text{conc,des,in}} + \dot{m}_{\text{des,reflux,in}} = \dot{m}_{\text{des,liq,out}} + \dot{m}_{\text{des,vap,out}} \tag{4.10}$$

$$\dot{m}_{\text{conc,des,in}} x_{\text{conc,des,in}} + \dot{m}_{\text{des,reflux,in}} x_{\text{reflux,in}} = \dot{m}_{\text{des,liq,out}} x_{\text{des,liq,out}} + \dot{m}_{\text{des,vap,out}} x_{\text{des,vap,out}} \tag{4.11}$$

For the sample point, the flow rates of the concentrated solution and reflux at the inlet are 0.00975 kg s^{-1} and 0.00026 kg s^{-1} respectively. The exiting refrigerant vapor and incoming solution are assumed to be in thermal equilibrium, and hence from a known high-side pressure (2092 kPa) and solution inlet temperature (105.6°C), the concentration of refrigerant vapor is

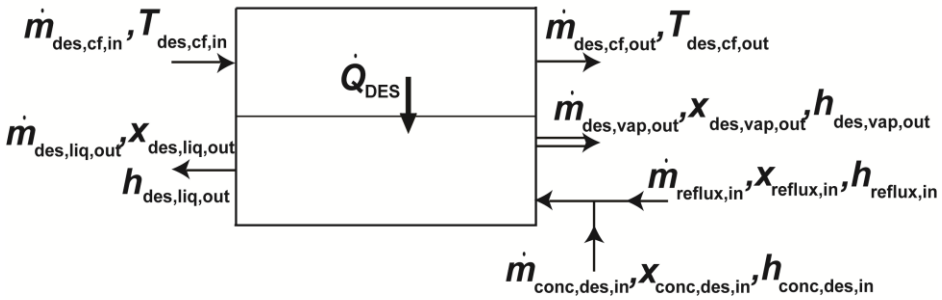

Figure 3.5 Desorber control volume

estimated to be 0.9535. The flow rates of exiting dilute solution and refrigerant vapor are found to be 0.00666 kg s^{-1} and 0.00335 kg s^{-1} respectively. The ammonia concentrations of the concentrated solution and reflux at the inlet are 0.4783 and 0.4249 respectively, whereas the dilute solution outlet concentration is estimated to be 0.2370.

The overall energy balance on the solution side of the desorber is shown in Equation (3.12).

$$\dot{Q}_{\text{des}} = \dot{m}_{\text{des,liq,out}} \cdot h_{\text{des,liq,out}} + \dot{m}_{\text{des,vap,out}} \cdot h_{\text{des,vap,out}} - \dot{m}_{\text{conc,des,in}} \cdot h_{\text{conc,des,in}} - \dot{m}_{\text{des,reflux,in}} \cdot h_{\text{reflux,in}} \quad (4.12)$$

The corresponding heat transfer rate for the coupling fluid side of the desorber is given by:

$$\dot{Q}_{\text{des}} = \dot{m}_{\text{des,cf}} c_{\text{p,cf,des}} (T_{\text{des,cf,in}} - T_{\text{des,cf,out}}) \quad (4.13)$$

The enthalpies of the concentrated solution and reflux at the inlet are determined to be 317 kJ kg^{-1} and 266 kJ kg^{-1}, respectively, whereas the enthalpies of the dilute solution and refrigerant vapor exiting the desorber are estimated to be 520 kJ kg^{-1} and 1533 kJ kg^{-1}, respectively. For the desorber coupling fluid, the flow rate and inlet temperature are set to 0.084 kg s^{-1} and 180°C, respectively. The outlet temperature is estimated to be 155.1°C and the corresponding heat transfer rate in the desorber is determined to be 5.45 kW.

Condenser

Figure 3.6 represents a control volume for the condenser. The refrigerant vapor exits the rectifier with an enriched ammonia concentration of 0.9985 and enters the condenser on the refrigerant side, while propylene glycol/water enters the condenser on the coupling fluid side.

The heat transfer rate on the refrigerant side is:

$$\dot{Q}_{\text{cond}} = \dot{m}_{\text{ref}} (h_{\text{cond,ref,in}} - h_{\text{cond,ref,out}}) \quad (4.14)$$

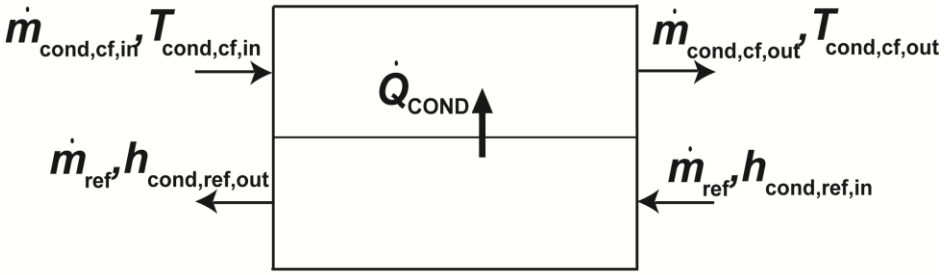

Figure 3.6 Condenser control volume

The corresponding heat transfer rate on the coupling fluid side is given by:

$$\dot{Q}_{cond} = \dot{m}_{cond,cf} c_{p,cf,cond} (T_{cond,cf,out} - T_{cond,cf,in}) \tag{4.15}$$

The flow rate and enthalpy of refrigerant entering the condenser is known from the rectifier outlet conditions to be 0.00309 kg s^{-1} and 1333 kJ kg^{-1} respectively, and the outlet enthalpy is estimated to be 236 kJ kg^{-1}. The flow rate and inlet temperature of the coupling fluid are set to be 0.112 kg $s^{-1}$and 40.5°C respectively, and the outlet temperature is estimated to be 48.1°C. The resulting condenser heat transfer rate is 3.39 kW.

Refrigerant Heat Exchanger

Figure 3.7 represents the control volume for the refrigerant heat exchanger. The refrigerant from the condenser exit flows on high-side, while the refrigerant vapor/two-phase mixture from the evaporator exit flows on the low-pressure side. The heat transfer rate of the refrigerant heat exchanger is evaluated using Equation (3.16), which is in turn used in

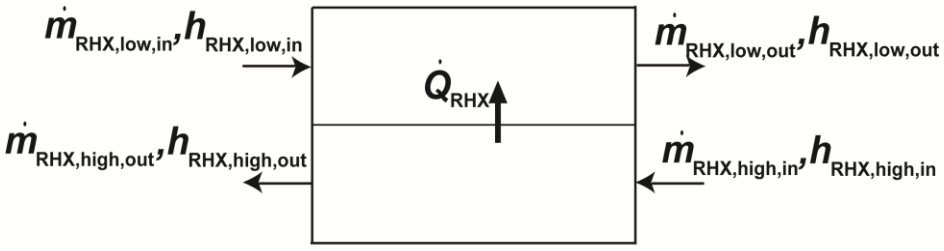

Figure 3.7 Refrigerant heat exchanger control volume

conjunction with an energy balance with the low-pressure side to obtain the lower pressure outlet of the refrigerant heat exchanger (Equation (3.17)):

$$\dot{Q}_{\text{RHX}} = \dot{m}_{\text{ref}} (h_{\text{RHX,high,in}} - h_{\text{RHX,high,out}}) \tag{4.16}$$

$$\dot{Q}_{\text{RHX}} = \dot{m}_{\text{ref}} (h_{\text{RHX,low,out}} - h_{\text{RHX,low,in}}) \tag{4.17}$$

The flow rate of the refrigerant is estimated from condenser exit conditions to be 0.00309 kg s^{-1}. The inlet enthalpy and temperature of the high-side refrigerant are estimated to be 236 kJ kg^{-1} and 49.0°C, respectively, and the corresponding inlet enthalpy and temperature of the low-side refrigerant are determined from the evaporator exit conditions to be 1263 kJ kg^{-1} and 7.2°C, respectively. From the heat transfer rate equations, the outlet enthalpy and temperature of high-side refrigerant are estimated to be 116.2 kJ kg^{-1} and 24.8°C, respectively, whereas the corresponding outlet enthalpy and temperature of the low-side refrigerant are 1383.1 kJ kg^{-1} and 47.8°C, respectively. The resulting heat transfer rate in the RHX is 0.369 kW.

Refrigerant Expansion Valve

The refrigerant expansion valve is isenthalpic, which yields:

$$h_{\text{ref,evap,in}} = h_{\text{RHX,high,in}} \tag{4.18}$$

The refrigerant valve inlet and outlet enthalpy are determined to be 116.2 kJ $kg^{-1}$from RHX exit conditions.

Evaporator

Figure 3.8 shows the control volume for the evaporator. The refrigerant from the expansion valve flows on the refrigerant-side and the coupling fluid flows on the other side. Refrigerant with an inlet temperature and vapor quality of 4.2°C and 0.078, respectively evaporates due to heat supplied by the coupling fluid entering at a temperature 12.7°C. The refrigerant exits the evaporator with a temperature and vapor quality of 7.2°C and 0.987,

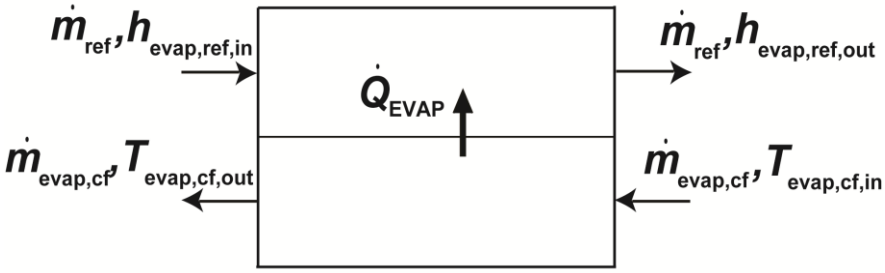

Figure 3.8 Evaporator control volume

respectively.The heat transfer rate of the evaporator is estimated using Equation (3.19) for the refrigerant side and Equation (3.20) for the chilled water side.

$$\dot{Q}_{evap} = \dot{m}_{ref}\,(h_{evap,ref,out} - h_{evap,ref,in}) \tag{4.19}$$

$$\dot{Q}_{evap} = \dot{m}_{evap,cf}\,(h_{evap,cf,in} - h_{evap,cf,out}) \tag{4.20}$$

The refrigerant flow rate and inlet enthalpy are determined to be 0.00309 kg s^{-1} and 116.2 kJ kg^{-1}, respectively, from valve outlet conditions. From a known low-side pressure (500 kPa), set glide temperature of 3 K, and refrigerant concentration (0.9985), the outlet enthalpy is found to be 1263.1 kJ kg^{-1}. The coupling fluid flow rate is set to 0.16 kg s^{-1}, and the outlet temperature of the coupling fluid and evaporator heat transfer rate are estimated to be 7.2°C and 3.54 kW respectively.

Solution Heat Exchanger

Figure 3.9 represents the control volume of the solution heat exchanger. Heat rejected by the dilution solution flowing on one side is used to heat the concentrated solution flowing on the other side. The heat transfer rate between the returning dilute solution and concentrated solution flowing toward the desorber is calculated for the two sides of the solution heat exchanger as follows:

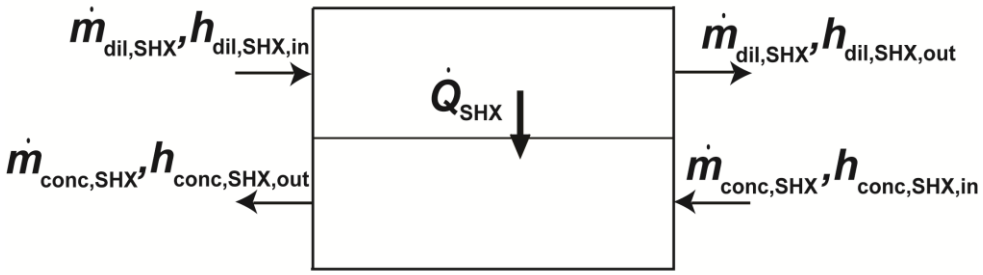

Figure 3.9 Solution heat exchanger control volume

$$\dot{Q}_{SHX} = \dot{m}_{dil,SHX}(h_{dil,SHX,in} - h_{dil,SHX,out})$$
$$\dot{Q}_{SHX} = \dot{m}_{conc,SHX}(h_{conc,SHX,out} - h_{conc,SHX,in}) \quad (4.21)$$

The flow rate and temperature of the dilute solution returning from the desorber are determined to be 0.00666 kg s^{-1} and 154°C, respectively, from desorber outlet conditions. The flow rate of concentrated solution is set to 0.00975 kg s^{-1}, and its temperature and enthalpy are determined from the rectifier outlet conditions to be 63.2°C and 45.1 kJ kg^{-1}, respectively. The effectiveness of SHX is set to 0.97. From a known high-side pressure (2092 kPa), dilute solution concentration (0.237) and SHX effectiveness (0.97), the outlet temperature and enthalpy of dilute solution are estimated to be 65.3°C and 123.2 kJ kg^{-1}, respectively. Similarly, with a known high-side pressure (2092 kPa), concentrated solution concentration (0.478) and SHX effectiveness (0.97), the enthalpy and temperature of concentrated solution at the outlet are estimated to be 317.1 kJ kg^{-1} and 105.1°C, respectively. The heat transfer rate in the solution heat exchanger is found to be 2.64 kW.

Solution expansion valve

The solution expansion valve is assumed to be isenthalpic and is represented by Equation (3.22).

$$h_{dil,abs,in} = h_{dil,SHX,out} \quad (4.22)$$

The enthalpy of the solution at the outlet of the valve is estimated from Equation (3.22), with the ammonia concentration being the same as at the inlet of the valve (0.237). For the sample point, the low-side pressure and dilute solution concentration are estimated to be 500 kPa and 0.237 respectively, and the dilute solution enthalpy at inlet and outlet is estimated to be 123.2 kJ kg^{-1}. The solution temperature at inlet and outlet of valve is found to 65.2°C.

Absorber

Figure 3.10 represents the control volume for the absorber. The refrigerant vapor exiting the refrigerant heat exchanger, and the dilute solution from the solution expansion valve enter the absorber at one end, and mix adiabatically. The solution is then cooled by the coupling fluid, and a concentrated solution exits the absorber.

The inlet conditions of the absorber are fixed from the properties of the solution at the outlet of the expansion valve and low-side refrigerant exit of the RHX, and the absorber heat transfer rate is estimated as follows:

$$\dot{Q}_{abs} = \dot{m}_{abs,ref,in} h_{abs,ref,in} + \dot{m}_{dil,abs,in} h_{dil,abs,in} - \dot{m}_{conc,abs,out} h_{conc,abs,out} \tag{4.23}$$

The corresponding heat transfer rate on the coupling fluid side is given by:

$$\dot{Q}_{abs} = \dot{m}_{abs,cf} c_{p,cf,abs} (T_{abs,cf,out} - T_{abs,cf,in}) \tag{4.24}$$

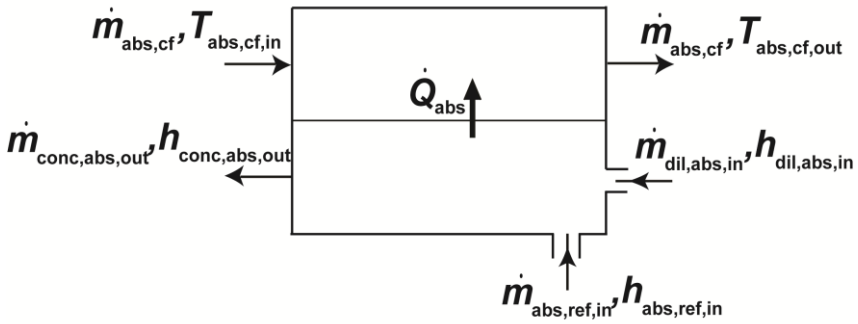

Figure 3.10 Absorber control volume

The flow rate and temperature of the low-side refrigerant at the exit of RHX are 0.00309 kg s^{-1} and 47.9°C, respectively. Similarly, the flow rate and temperature of dilute solution at the inlet are determined from the solution valve outlet to be 0.00666 kg s^{-1} and 65.2°C respectively. The dilute solution and refrigerant form a mixture whose temperature and vapor quality are 76.9°C and 0.277, respectively. The mixture temperature (76.9°C) is significantly higher than the temperature of dilute solution exiting the expansion valve (65.2°C), and a higher absorber inlet temperature increases the LMTD between the solution and coupling fluid, thereby increasing the heat transfer rate in the absorber. The two-phase mixture is cooled to a sub-cooled liquid state at 41.2°C by the coupling fluid, whose flow rate and inlet temperature are set to 0.112 kg s^{-1} and 40.5°C, respectively. The degree of sub-cooling at the absorber outlet was set at 2°C. Based on these values, the absorber heat transfer rate is 5.63 kW, while the outlet temperature of the coupling fluid is 53°C.

Table 3.2 summarizes the output parameters (heat transfer rates, pressures, flow rates and concentration) for the design point considered for the illustration of this sample data point.

3.3.3 System performance

The design parameters for the single-effect ammonia-water absorption chiller (Table 3.1) are used as the basis for the development of the transient model (Chapter 4). The parameters such as sizes of the heat exchangers, the temperatures of the coupling fluids and the pumping rate of the concentrated solution are input from the steady-state model described in this chapter.

The cooling mode COP of the absorption heat pump is calculated as:

$$COP_{cool} = \frac{\dot{Q}_{evap}}{\dot{Q}_{des}} \tag{4.25}$$

Table 3.2 Summary of output parameters

	Description	Parameter	Value	Units
Heat transfer rates/COP	Evaporator	$\dot{Q}_{evap}$	3.54	kW (1 RT)
	Desorber	$\dot{Q}_{des}$	5.45	kW
	Coefficient of Performance	COP	0.65	-
	Absorber	$\dot{Q}_{abs}$	5.63	kW
	Condenser	$\dot{Q}_{cond}$	3.4	kW
	SHX	$\dot{Q}_{SHX}$	2.65	kW
	RHX	$\dot{Q}_{RHX}$	0.37	kW
	Rectifier	$\dot{Q}_{rect}$	0.95	kW
Flow rates	Concentrated solution	$\dot{m}_{conc}$	9.75×10^{-3}	kg s^{-1}
	Dilute solution	$\dot{m}_{dil}$	6.66×10^{-3}	kg s^{-1}
	Refrigerant	$\dot{m}_{ref}$	3.09×10^{-3}	kg s^{-1}
Pressure	High-side pressure	P_{high}	2092	kPa
	Low-side pressure	P_{low}	500	kPa
Ammonia Concentration	Refrigerant	x_{ref}	0.9985	-
	Dilute solution	x_{dil}	0.237	-
	Concentrated solution	x_{conc}	0.4783	-

Figure 3.11 shows the variation of this COP and cooling capacity of the absorption chiller for different ambient temperatures. It can be seen that at an ambient temperature of 35°C, the COP of the chiller is 0.65, and its cooling capacity is 3.54 kW (1 RT). Also, both are found to decrease with an increase in ambient temperature, as expected. This is because a higher ambient temperature requires a higher pressure in the desorber and condenser, thus requiring a greater

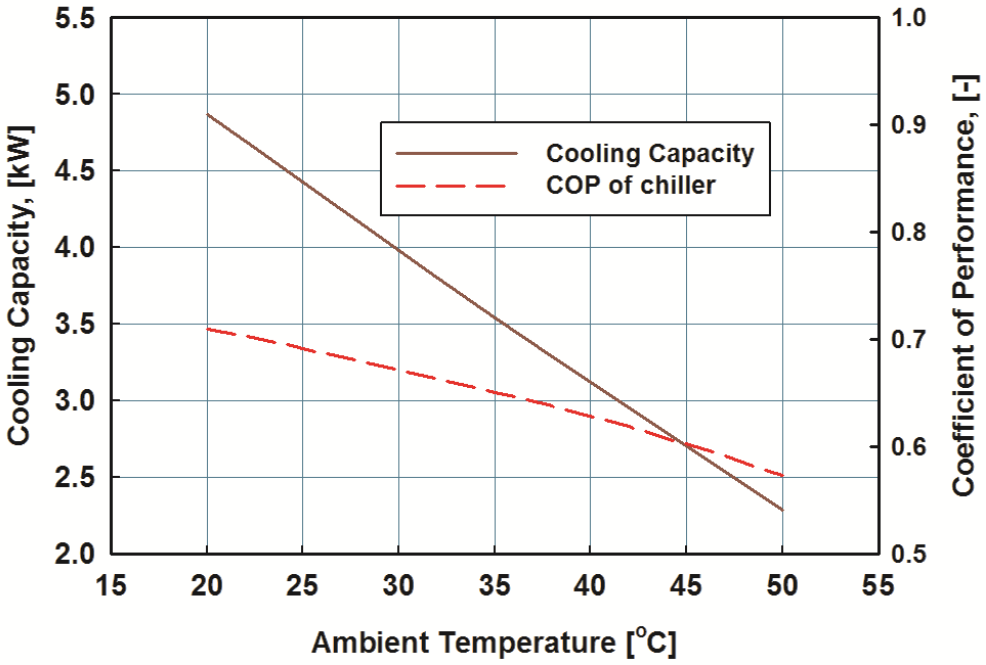

Figure 3.11 Steady-state performance of the absorption chiller

temperature and pressure lift, and a higher heat input in the desorber to maintain the same cooling capacity.

The present chapter addressed the steady-state modeling of the absorption chiller. These thermodynamic modeling details form the basis for the transient model in the following chapter. It should be noted that the input parameters for this model are representative of the chiller reported by Determan and Garimella (2012).

4. DYNAMIC MODELING

This chapter focuses on the dynamic modeling of a single-effect ammonia-water absorption chiller. First, a brief introduction to the dynamic model is provided, in addition to the differences between this model and the steady-state model described in Chapter 3. Second, the different modeling strategies used to address the system transients are summarized. Finally, the component models are explained in detail.

The component models are developed in the Simulink® environment, where they are implemented as individual blocks and integrated to simulate the single-effect ammonia-water absorption cycle.

4.1 Introduction to dynamic model

A dynamic model for a single-effect ammonia-water absorption cycle is developed in this study to address some of the limitations of other similar efforts discussed in the literature review (Chapter 2).

Figure 4.1 shows a schematic of the dynamic model for a single-effect ammonia-water absorption chiller considered here.

The basic components of the cycle are the evaporator (EVAP), condenser (COND), desorber (DES), absorber (ABS), solution tank and refrigerant tank. The recuperative heat exchangers include the solution heat exchanger (SHX), refrigerant heat exchanger (RHX), and rectifier (RECT). Other components, such as the solution pump (P) and the expansion valves (SXV and RXV), are also included. Connecting lines are not included in the present model, because in a microscale absorption chiller, pressure drop in such components is expected to be relatively small compared to total system pressures, and also because these lines are expected to account for less than five percent of system thermal storage capacity.

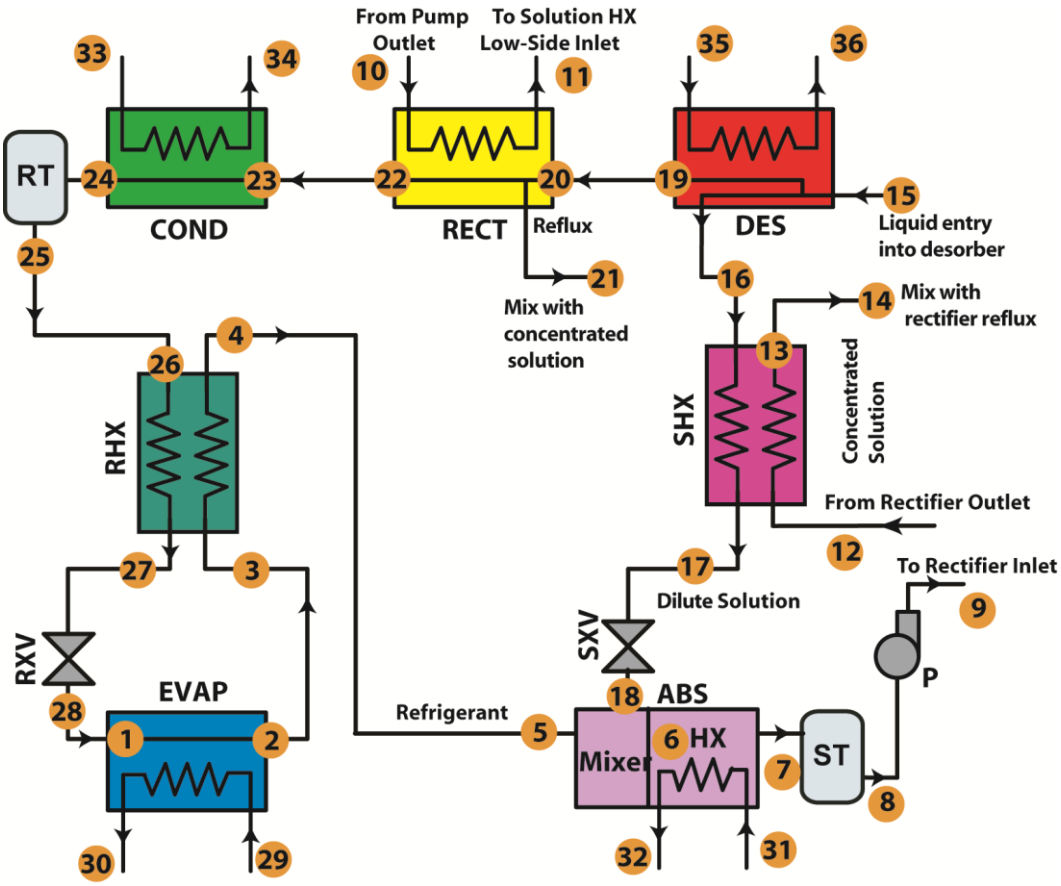

Figure 4.1 Absorption cycle schematic

The schematic includes the heat and mass exchanging components present in the absorption cycle, as explained in connection with the steady-state model in Chapter 3. However, it includes some additional components such as the refrigerant tank and the solution tank. The tanks act as storage devices, allowing expansion and contraction of refrigerant and solution when the system operates during start-up, shut-down or other transient events.

4.2 Salient features of dynamic model

The dynamic model incorporates the following key system parameters to model the transient behavior:

- Heat-transfer areas and thermal masses of heat exchangers

- Valve settings
- Solution flow rates and coupling fluid pumping rate
- System charge
- Volume of storage devices

These parameters are representative of the miniaturized absorption chiller developed by Determan and Garimella (2012).

Transient behavior during chiller start-up is modeled to account for several factors:

- Thermal mass of heat and mass exchanging components
- Gradual pressure evolution in the system
- Flow rates governed by pressure difference across the valve

4.2.1 Dynamic modeling strategies

Heat and Mass exchangers

As explained earlier, the absorption chiller contains several heat and mass exchangers, making the thermal masses of these components very important when determining the transient behavior of the chiller. Heat and mass exchanger walls, and adjacent fluid volumes are assigned thermal energy storage capacities. Individual heat and mass exchangers are modeled in a segmented fashion to yield detailed predictions of heat transfer and thermal energy storage. Simulation resolution can be increased by further refining the segmented heat and mass exchanger models. Flow rates and species concentrations are assumed to be uniform along the length of the heat exchanger for components without absorption or desorption. For example, the evaporator fluid flow rates and ammonia concentration in each segment are identical at a given instant.

System pressures

The dynamics of system pressures are much faster than the dynamics of heat and mass transfer in the components. Thus, the system is characterized by two distinct pressures at any instant, the high-side pressure and the low-side pressure. For example, a change in the high-side pressure is propagated to other high-side components almost instantly ($\tau \sim 0.002$ s), at the speed of sound. However, heat transfer rate propagation is at the velocity of the flow (~ 0.2-0.5 m/s) between the components ($\tau \sim 1$ s). Any pressure drop internal to the components is neglected, thus eliminating the need for modeling of the momentum balance in the components.

System pressures are determined from vapor-liquid equilibrium conditions in the storage tanks. The high-pressure components (desorber, rectifier, condenser and SHX) are assumed to be at the pressure set by the refrigerant tank, supplied with refrigerant from the condenser outlet. Frictional pressure drops in the components are assumed to be negligible compared to an approximately 1.5 MPa difference between the high- and low-side pressures. The low-pressure components (evaporator and absorber) are assumed to be at the pressure set by the solution tank, supplied with liquid from the absorber outlet.

Flow rates and concentration

As mentioned earlier, segmented models are employed for the heat and mass exchangers. Flow rates and concentration inside the components are assumed to be uniform in individual components, where concentration is defined as the mass fraction of ammonia in the mixture. Mass storage is assumed to occur solely in the refrigerant and solution tanks, because the chiller developed by Determan and Garimella (2012) consists of microchannel heat and mass exchangers that have minimal fluid inventories in comparison to the inventory in the storage devices.

The governing mass, species and energy balances are carried out inside individual components that are developed in Simulink® and assembled to constitute a complete absorption cycle. The system parameters used in the model, such as heat exchanger sizes, flow rates, and coupling fluid temperatures, are representative of the chiller developed by Determan and Garimella (2012).

4.3 Dynamic model formulation

First, a segmented heat exchanger model is presented followed by the heat transfer rate estimation for each component. Then the heat and mass transfer modeling pertaining to desorber is summarized, and a specialized solver developed for this purpose is explained.

The modeling of other components such as the pump and the valve is also explained, followed by a brief summary of the thermodynamic property routines and model implementation, concluding with a sensitivity analysis of the segmented heat exchanger model.

4.3.1 Heat exchanger model

Heat transfer in the evaporator, condenser, RHX, SHX and absorber is modeled in a segmented fashion. This approach enables detailed prediction of the temperature evolution during transient processes, and yields more realistic prediction of component-level heat transfer rates than 2-point LMTD estimations for the highly zeotropic ammonia-water mixtures. Each component segment includes an internal dividing wall and two adjacent fluid volumes. Each wall segment is assigned a thermal capacity (mc_p) and thermal energy storage is tracked in each fluid segment. A schematic of such a heat exchanger with *N* segmental control volumes is presented in Figure 4.2. Figure 4.3 shows the control volumes for the wall and fluids, corresponding to the i^{th} segment of the heat-exchanger component.

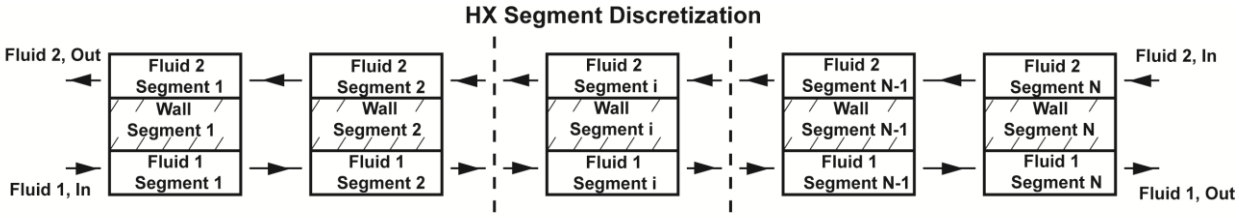

Figure 4.2 Discretized model of Heat Exchanger

The heat transfer rate is modeled as shown in Equations (4.1)-(4.3).

$$\frac{dU_{1f,i}}{dt} = \dot{m}_{1f}\,(h_{1f,in} - h_{1f,out}) - \dot{Q}_{1f,i} \tag{4.1}$$

$$\frac{dU_{2f,i}}{dt} = \dot{Q}_{2f,i} - \dot{m}_{2f,i}\,(h_{2f,out} - h_{2f,in}) \tag{4.2}$$

$$(Mc_p)_{w,i}\,\frac{dT_{w,i}}{dt} = \dot{Q}_{1f,i} - \dot{Q}_{2f,i} \tag{4.3}$$

The rates of thermal energy storage in fluids 1 and 2 are explained in Equations (4.1) and (4.2), respectively. The heat transfer rates between fluid 1 and the wall ($\dot{Q}_{1f,i}$), and the rate of

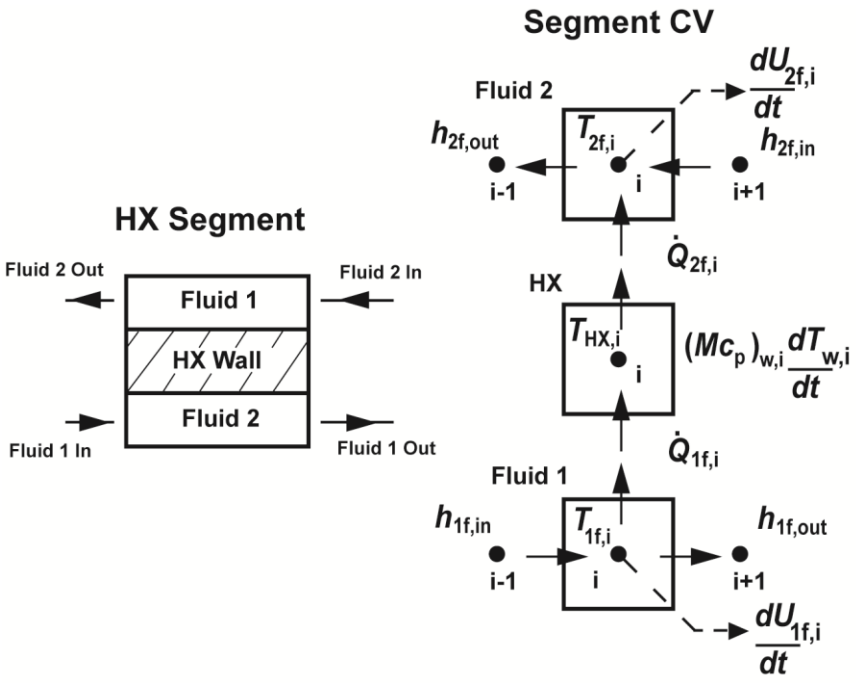

Figure 4.3 Segmental Control Volume of Heat Exchanger

enthalpy change for fluid 1 ($\dot{m}_{1f}(h_{1f,in} - h_{1f,out})$) are different during transient start up, and this difference is the rate of energy stored $\frac{dU_{1f,i}}{dt}$ in fluid 1. Similarly, the heat transfer rate between wall and fluid 2 ($\dot{Q}_{2f,i}$), and the rate of enthalpy change for fluid 2 ($\dot{m}_{2f}(h_{2f,in} - h_{2f,out})$) are different during transient start up, and this difference is the rate of energy stored $\frac{dU_{2f,i}}{dt}$ in fluid 2. Equation (4.3) represents the thermal energy storage in the wall due to its thermal mass. The difference in heat transfer rates between fluid 1 and wall ($\dot{Q}_{1f,i}$), and fluid 2 and wall ($\dot{Q}_{2f,i}$) account for the rate of thermal energy storage $(Mc_p)_{w,i}\frac{dT_{w,i}}{dt}$ in the wall. At steady state, the heat transfer rate across the wall ($\dot{Q}_{1f,i}, \dot{Q}_{2f,i}$) and the rates of enthalpy change in the fluids ($\dot{m}_{1f}(h_{1f,in} - h_{1f,out}), \dot{m}_{2f}(h_{2f,out} - h_{2f,in})$) are identical. The net heat input in each segment is equal to the rate of enthalpy change for the fluid on either side of wall.

Here the enthalpies at the inlet and outlet are evaluated using a first-order upwind scheme (Patankar, 1980). According to Patankar (1980), the use of upwind scheme is preferred over central differencing in advection-related problems. It guarantees a stable solution, whereas the use of a central difference scheme can lead to the occurrence of oscillations. The quantities at the inlet and outlet of the control volume (Figure 4.3) are evaluated based on the upwind scheme.

$$\begin{aligned} h_{1f,in} &= h_{1f,i-1}, \quad h_{1f,out} = h_{1f,i} \\ h_{2f,in} &= h_{2f,i+1}, \quad h_{2f,out} = h_{2f,i} \end{aligned} \tag{4.4}$$

The internal heat transfer rates $\dot{Q}_{1f,i}$ and $\dot{Q}_{2f,i}$ in the i^{th} segment are expressed in terms of the fluid temperatures, $T_{1f,i}$, $T_{2f,i}$, wall temperature $T_{w,i}$, and their respective heat transfer coefficients and transfer areas, $\alpha A_{1f,i}$, $\alpha A_{2f,i}$ as shown in Equation (4.5).

$$\dot{Q}_{1f,i} = (\alpha A)_{1f,i} \cdot (T_{1f,i} - T_{w,i})$$
$$\dot{Q}_{2f,i} = (\alpha A)_{2f,i} \cdot (T_{w,i} - T_{2f,i}) \quad (4.5)$$

Table 4.1 summarizes the fluid stream conditions for the heat exchangers in an absorption cycle. For components such as the evaporator, condenser and absorber, 1f represents the ammonia-water mixture and 2f represents the coupling fluid whereas for the SHX and RHX, both 1f and 2f represent the ammonia-water mixture. Although the absorber has two inlet ports, only the heat exchanging section is modeled using the segmented model, and hence, 1f inlet

Table 4.1 Summary of heat exchanger fluids

	Fluid 1	**Fluid 2**
Evaporator	Two-phase NH_3/H_2O mixture	Water/propylene glycol (25% glycol concentration) as coupling fluid
Condenser /Absorber	Two-phase NH_3/H_2O mixture	Water/propylene glycol (25% glycol concentration) as coupling fluid
SHX	Concentrated NH_3/H_2O solution	Dilute NH_3/H_2O solution
RHX	NH_3/H_2O solution at high pressure	NH_3/H_2O two-phase mixture/vapor at low pressure
Desorber	Liquid and vapor phases of NH_3/H_2O mixture	Heated Paratherm™ as coupling fluid

represents the ammonia-water mixture after vapor-liquid mixing, while 1f outlet marks the liquid outlet in the absorber, and 2f represents the coupling fluid. For the ammonia-water mixture and the coupling fluids, the internal energy and specific enthalpy are related as $U = M(h - Pv)$.

An initial mass of ammonia-water M_f, is assumed to be present inside the component, based on the component fluid volume and an assumed initial density. Initially, the mass is distributed equally between heat exchanger segments. The mass of fluid inside the component prior to start up, M_f , depends on the initial density (~800 kg m^{-3} for saturated liquid) and fluid volume inside the component $(M_f = \rho_f V_{f,HX})$. Initial fluid density is determined from a known initial temperature, pressure and ammonia concentration. Flow rates, thermal capacities, heat transfer resistances, and material properties are adopted from the steady-state system model explained in Chapter 3. Specifications for the heat exchangers are summarized in Table 4.2.

Frictional pressure drop across the components is assumed negligible compared to the high-to-low side pressure difference (~1.5 MPa at steady state). Thus, each segment pressure is set to the respective overall component pressure. The system under consideration consists of microchannel heat exchangers, and any change in the fluid inventory inside these heat exchangers is considered negligible compared to inventories in the solution and refrigerant tanks. This assumption enables solution without the added complexity of solving for frictional pressure drops and non-linear momentum equations. However, thermal energy storage in the fluids and wall thermal masses are accounted for in these heat exchangers. The thermal masses (5-10% of heat exchanger thermal mass) of connecting lines are small compared to heat exchanger thermal masses.

Table 4.2 Properties of EVAP, COND, ABS, DES, RHX and SHX

	Description	Units	Parameter	Component					
				EVAP	COND	ABS	DES	SHX	RHX
Coupling fluid/fluid 2	Specific heat	kJ kg^{-1} K^{-1}	$c_{p,cf}$	3.97	3.99	3.99	2.54	-	-
	Density	kg m^{-3}	ρ_{cf}	1010	1010	1010	800	800	29
	Fluid volume	m^3	V_{cf}	3×10^{-5}	5×10^{-5}	10^{-4}	4×10^{-5}	10^{-5}	3×10^{-5}
	Mass of fluid	kg	m_{cf}	0.03	0.05	0.1	0.033	0.008	0.001
	Flow rate	kg s^{-1}	$\dot{m}_{cf}$	0.16	0.112	0.112	0.084	-	-
Wall	Specific heat	kJ kg^{-1} K^{-1}	$c_{p,w}$	0.48					
	Mass of wall	kg	m_w	3	5	10	20	1.9	2.8
Ammonia-water/fluid 1	Initial density	kg m^{-3}	ρ_f	29	29	800	800	800	29
	Fluid volume	m^3	V_f	2×10^{-5}	6×10^{-5}	10^{-4}	4×10^{-5}	2×10^{-5}	3×10^{-5}
	Mass of fluid	kg	m_f	0.0006	0.002	0.08	0.03	0.016	0.001
	No. of segments	-	N	5	5	5	3	3	3
	Heat transfer conductance	W K^{-1}	$(\alpha A)_{1f}$	2200	950	1650	720	360	80
	Heat transfer conductance	W K^{-1}	$(\alpha A)_{2f}$	1060	2050	4270	330	510	1000

4.3.2 Heat exchanger parameters

The specifications for the heat exchangers such as the evaporator, condenser, desorber, absorber and the recuperative heat exchangers (RHX and SHX) are summarized in Table 4.2. The parameters such as fluid volumes, heat transfer areas, specific heats, wall mass, and others are representative of the absorption chiller developed by Determan and Garimella (2012).

An initial temperature of 20°C and pressure of 400 kPa are assumed for all components. Then, the properties of ammonia-water mixture and the coupling fluid prior to start up are estimated based on the volume and type of fluid in the heat exchanger. Table 4.1 shows the type of fluids circulated in the heat exchangers.

Coupling fluid

The coupling fluid for the evaporator, condenser, and absorber is a water/propylene glycol solution with 25% glycol concentration. A constant specific heat of 3.99 kJ kg^{-1} K^{-1} at an average temperature of 45°C is assumed for the water/propylene glycol solution in the condenser and absorber, whereas a specific heat of 3.97 kJ kg^{-1} K^{-1} at an average temperature of 9°C is assumed for water/glycol solution inside the evaporator (Klein, 2010). A coupling fluid volume of 3×10^{-5} m^3 and an initial density of 1010 kg m^{-3} leads to an initial coupling fluid mass of 0.03 kg inside the evaporator. The coupling fluid mass is then equally divided between the five evaporator segments. Similarly, the coupling fluid mass inside each component is estimated, and the corresponding thermal mass ($Mc_{p,cf}$) is accounted for in the heat transfer rate estimation.

The coupling fluid used in the desorber is heated Paratherm^{TM}, which has density of 800 kg m^{-3} and specific heat of 2.54 kJ kg^{-1} K^{-1} at an average temperature of 165°C. These properties are estimated based on curve fits for thermal properties of Paratherm NF® heat transfer fluid (Paratherm, 2012). A coupling fluid volume of 4×10^{-5} m^3 in the desorber yields an initial coupling fluid mass of 0.033 kg.

The flow rates of the coupling fluids are chosen based on the steady-state model described in Chapter 3. The flow rates are matched with the steady-state model so that performance of the dynamic model upon achieving steady state can be used for comparison.

Ammonia-water mixture

The initial density for the ammonia-water mixture is estimated based on an initial temperature (20°C), pressure (400 kPa) and vapor quality of the ammonia-water mixture in the components. Initial vapor qualities inside the RHX, condenser and evaporator are assumed to be 0.1, identical to the vapor quality in the refrigerant tank (0.1), whereas the absorber and SHX are

assumed to be filled with solution (saturated liquid). For example, an evaporator fluid volume of $V_{sol} = 2 \times 10^{-5}$ m^3 and an initial density of 29 kg m^{-3} result in an initial ammonia-water mass of $M_{sol} = 0.0006$ kg. The initial mass in each of the components is estimated in this manner.

Heat exchanger wall

The absorption heat pump under consideration uses microchannel plate heat exchangers. The heat exchanger wall is assumed to be made of stainless steel with specific heat of $c_{p,w} = 0.48$ kJ kg^{-1} K^{-1} at a temperature of 27°C (Incropera and DeWitt, 1996)

Heat transfer areas

The steady-state model described in Chapter 3 employs overall UA values to estimate the heat transfer coefficients and transfer areas. However, the segmented model uses a known value of heat transfer coefficient and transfer area for the solution- and coupling fluid- sides for each component. Thus, the heat transfer area A_{HX} is distributed equally between N segments while the heat transfer coefficient α is assumed to be identical for each segment for a given heat exchanger.

The heat transfer conductances listed in Table 4.2 for the solution side and coupling fluids, are representative of the absorption chiller developed by Determan and Garimella (2012). The thermal conductances of the components listed in Table 4.2 are estimated based on the analysis by Determan and Garimella (2012). Microchannel heat exchangers with channel hydraulic diameters of 306 μm are employed in the calculations. The thermal conductance estimations are summarized in Appendix A.

The number of segments is chosen as five (N = 5) for the evaporator, condenser and absorber, whereas the recuperative heat exchangers (SHX and RHX) each consist of three

segments (N = 3). Sensitivity analysis is performed by varying the number of heat exchanger segments, and the results are summarized in the final section (4.3.11) of this chapter.

The absorber has a higher heat transfer conductance $(\alpha A)_2 = 4270\ \text{W K}^{-1}$ on the coupling fluid side compared to the ammonia-water side $(\alpha A)_1 = 1650\ \text{W K}^{-1}$, confirming the fact that absorber is limited by the heat transfer on the working-fluid side. The evaporator has a higher working-fluid-side heat transfer conductance $(\alpha A)_1 = 2200\ \text{W K}^{-1}$ compared to the coupling fluid-side conductance, $(\alpha A)_2 = 1060\ \text{W K}^{-1}$, due to phase-change in the ammonia-water mixture inside evaporator. In the RHX, the hot-side heat transfer coefficient $(\alpha A)_2 = 1000\ \text{W K}^{-1}$ is higher than the cold-side value, $(\alpha A)_1 = 80\ \text{W K}^{-1}$, due to the higher temperature and pressure of the ammonia-water on the high side than on the low side.

A segmental analysis is required to model the heat transfer rates in the components because temperature and quality of ammonia-water vary along the components.

4.3.3 Evaporator and condenser

The refrigerant in the evaporator and condenser is assumed to be homogenous, such that the vapor and liquid phases are in equilibrium and flow at the same velocity. Thus, the enthalpy of ammonia-water at each segment outlet is estimated using the governing Equations (4.1)-(4.5).

Once the inlet and outlet enthalpies are obtained, the component heat transfer rates are estimated between corresponding state points in EVAP and COND (Figure 4.1).

$$\dot{Q}_{\text{EVAP}} = \dot{m}_1 (h_2 - h_1) \tag{4.6}$$

$$\dot{Q}_{\text{COND}} = \dot{m}_{23} (h_{24} - h_{23}) \tag{4.7}$$

4.3.4 SHX and RHX

Segmental information for the recuperative heat exchangers (SHX and RHX) are summarized in Table 4.1. During transient operation, the heat transfer rates for the two fluids in SHX and RHX are different due to thermal storage in the heat exchanger wall. Figure 4.4 represents the control volume of the solution heat exchanger. The heat transfer rate between the returning the dilute solution and SHX wall is $\dot{Q}_{\text{SHX,cool}}$ and the corresponding rate between wall and concentrated solution is $\dot{Q}_{\text{SHX,heat}}$. At steady-state, both heat transfer rates are identical.

$$\begin{aligned} \dot{Q}_{\text{SHX,cool}} &= \dot{m}_{16}(h_{16} - h_{17}) \\ \dot{Q}_{\text{SHX,heat}} &= \dot{m}_{12}(h_{13} - h_{12}) \\ Mc_{p,w}\frac{dT_w}{dt} &= \dot{Q}_{\text{SHX,cool}} - \dot{Q}_{\text{SHX,heat}} \end{aligned} \tag{4.8}$$

Figure 4.5 represents the RHX control volume. It shows the incoming high-pressure

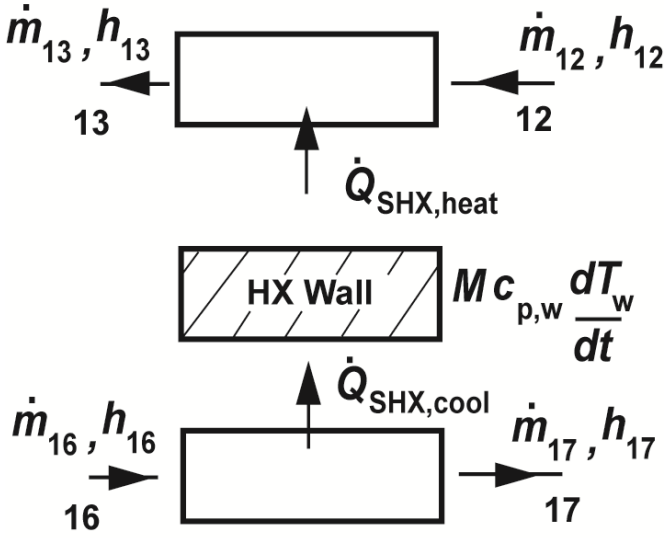

Figure 4.4 Segmental Control volume of Solution Heat Exchanger

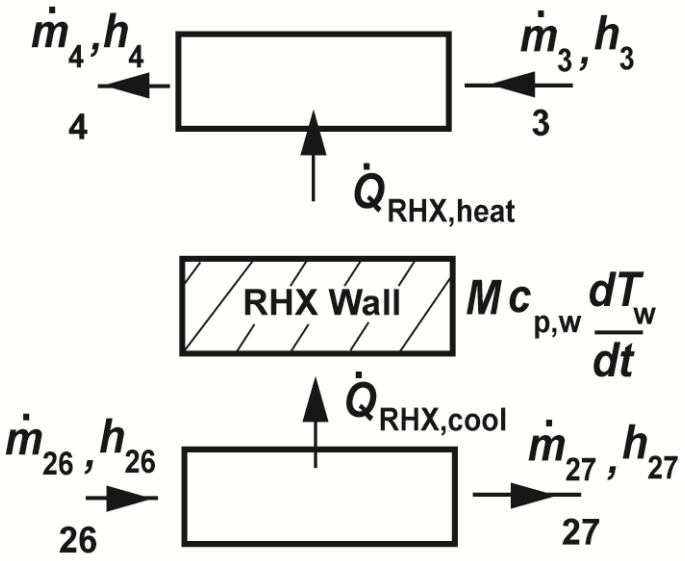

Figure 4.5 Segmental Control Volume of Refrigerant Heat Exchanger

refrigerant losing heat to the RHX wall and the low-pressure refrigerant from the evaporator gaining heat from the RHX wall. At steady-state, both heat transfer rates are identical.

$$\begin{aligned} \dot{Q}_{\text{RHX,cool}} &= \dot{m}_{26}(h_{26} - h_{27}) \\ \dot{Q}_{\text{RHX,heat}} &= \dot{m}_3(h_4 - h_3) \\ Mc_{p,w}\frac{dT_w}{dt} &= \dot{Q}_{\text{RHX,cool}} - \dot{Q}_{\text{RHX,heat}} \end{aligned} \tag{4.9}$$

4.3.5 Absorber

The absorber is modeled as a combination of an adiabatic pre-mixing section and a heat exchanger section. In the pre-mixing section, the incoming ammonia vapor at (5) in Figure 4.1 and, the dilute ammonia-water solution at (18) mix and reach thermal equilibrium (6). The geometry of the absorber is assumed to accomplish thorough mixing of the liquid and vapor phases. The well-mixed fluid is cooled by the coupling fluid as it flows through the absorber heat exchanger section (Figure 4.1).

The mass transfer resistance between the liquid and vapor phases in the absorber is neglected in the dynamic model because an exclusive component model would be required for a falling-film absorber, which would involve very detailed and complex modeling of mass transfer processes inside the absorber. Including such a detailed analysis in an overall system level model substantially increases the complexity of the model, and increases computational time because it involves solving a non-linear 1-D momentum equation and solving for local pressure drops and interfacial areas.

In the present study, the focus is on performing a system level analysis during start-up, shut-down and other transient events. Thus, the heat transfer due to cooling and condensing of the liquid-vapor mixture from two-phase to single-phase liquid state is estimated as the heat duty of the absorber. The two fluid phases are assumed to be in thermal equilibrium throughout the heat exchanger section.

The mass, species and energy balances are carried out for the pre-mixing section in the absorber.

$$\begin{aligned} \dot{m}_{18} + \dot{m}_5 &= \dot{m}_6 \\ \dot{m}_{18} x_{18} + \dot{m}_5 x_5 &= \dot{m}_6 x_6 \\ \dot{m}_{18} h_{18} + \dot{m}_5 h_5 &= \dot{m}_6 h_6 \end{aligned} \tag{4.10}$$

The heat transfer rate for the absorber is:

$$\dot{Q}_{\mathrm{ABS}} = \dot{m}_6 (h_6 - h_7) \tag{4.11}$$

4.3.6 Desorber and rectifier

Desorber

A counterflow desorber is modeled in the present study. In this configuration, the downward flowing ammonia-water solution is heated through direct contact with the desorber

walls, countercurrent to the heating coupling fluid. The generated refrigerant vapor rises countercurrent to the solution flow. The component configuration is presented schematically in Figure 4.6 (a).

In the present model, the desorber is divided into three segments of equal transfer area (N = 3). Heat and mass transport in individual segments is presented in Figure 4.6 (b) for the i^{th} segment.

To reduce the complexity of the desorber model, the following assumptions are made:

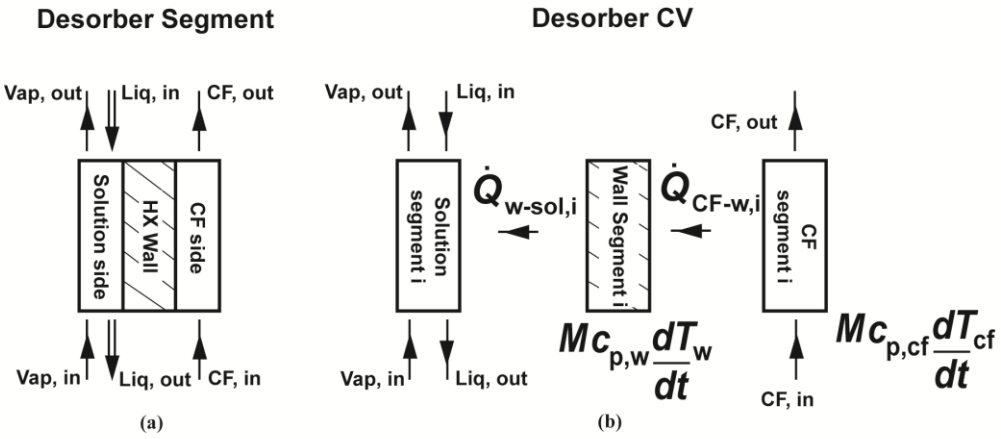

Figure 4.6 (a) Segmented model of desorber (b) Control Volume of desorber

- Thermal storage capacity of the ammonia-water mixture is considered negligible compared to that in the desorber wall and the coupling fluid.
- The liquid and vapor phases are at saturated thermodynamic states throughout the desorber.

Neglecting the thermal storage in the ammonia-water mixture inside the desorber greatly simplifies the energy balance given in Equation (4.14) and eases convergence of the iterative solver described later in this section. Properties (enthalpy, concentration, etc.) and flow rates at

the segment boundaries are identical to the ones upstream of the control volume, according to the upwind scheme (Patankar, 1980). The governing mass, species and energy balance equations for the ammonia-water mixture (solution side CV) in each desorber segment are:

$$\dot{m}_{\text{liq,i+1}} + \dot{m}_{\text{vap,i-1}} = \dot{m}_{\text{liq,i}} + \dot{m}_{\text{vap,i}} \tag{4.12}$$

$$\dot{m}_{\text{liq,i+1}} x_{\text{liq,i+1}} + \dot{m}_{\text{vap,i-1}} x_{\text{vap,i-1}} = \dot{m}_{\text{liq,i}} x_{\text{liq,i}} + \dot{m}_{\text{vap,i}} x_{\text{vap,i}} \tag{4.13}$$

$$\dot{m}_{\text{liq,i+1}} h_{\text{liq,i+1}} + \dot{m}_{\text{vap,i-1}} h_{\text{vap,i-1}} + (\alpha A)_{\text{liq,i}} (T_{\text{w,i}} - T_{\text{liq,i}}) = \dot{m}_{\text{liq,i}} h_{\text{liq,i}} + \dot{m}_{\text{vap,i}} h_{\text{vap,i}} \tag{4.14}$$

The energy balance for the coupling fluid and internal dividing wall segments are:

$$(M.c_p)_{\text{cf}} \frac{dT_{\text{cf,i}}}{dt} = \dot{m}_{\text{cf}} c_{\text{p,cf}} (T_{\text{cf,i-1}} - T_{\text{cf,i}}) - (\alpha A)_{\text{cf,i}} (T_{\text{cf,i}} - T_{\text{w,i}}) \tag{4.15}$$

$$(M.c_p)_{\text{w,i}} \frac{dT_{\text{w,i}}}{dt} = (\alpha A)_{\text{cf,i}} (T_{\text{cf,i}} - T_{\text{w,i}}) - (\alpha A)_{\text{liq,i}} (T_{\text{w,i}} - T_{\text{liq,i}}) \tag{4.16}$$

The desorber segmental heat transfer coefficients and material properties are summarized in Table 4.2. Thus, there are eight unknowns for each segment at the solution-side of the desorber: $(\dot{m}_{\text{liq,i}}, \dot{m}_{\text{vap,i}}, x_{\text{liq,i}}, x_{\text{vap,i}}, h_{\text{liq,i}}, h_{\text{vap,i}}, T_{\text{liq,i}}, T_{\text{vap,i}})$.

The liquid inlet conditions at the top of the desorber (concentrated solution inlet at (15) in Figure 4.1) are obtained from the SHX outlet, and because no vapor enters the desorber at the bottom, the bottom-most segment has a zero vapor inflow rate $(\dot{m}_{\text{vap,0}} = 0)$.

$$\begin{aligned} T_{\text{liq,N+1}} &= T_{15}, \quad x_{\text{liq,N+1}} = x_{15} \\ h_{\text{liq,N+1}} &= h_{15}, \quad \dot{m}_{\text{liq,N+1}} = \dot{m}_{15} \end{aligned} \tag{4.17}$$

Desorber Solver

A specialized solver is developed to iteratively determine the unknown vapor and liquid states at the outlet of each segment of the desorber, during each time step. The unknown desorber solution-side quantities are evaluated using the secant-method based solver described in the

following section. This specialized solver is developed to reduce the computation time compared to the Simulink® built-in solver. The guess values for the vapor and liquid outflow rates in a segment are set to the inflow values.

$$\dot{m}_{\text{liq,i}} = \dot{m}_{\text{liq,i+1}} \text{ , } \dot{m}_{\text{vap,i}} = \dot{m}_{\text{vap,i-1}} \tag{4.18}$$

- The pressure on the solution-side of the desorber is obtained from the specified inlet pressure at (15) in Figure 4.1.
- The saturated vapor-phase concentration and enthalpy ($x_{\text{vap,i}}$,$h_{\text{vap,i}}$) are evaluated using the phase equilibrium relations at the vapor phase temperature $(T_{\text{vap,i}} = T_{\text{liq,i+1}})$ and the high-side pressure.
- Mass and species balances shown in Equations (4.12) and (4.13) are performed to determine the liquid-phase concentration $x_{\text{liq,i}}$. The saturated liquid-phase properties ($T_{\text{liq,i}}$, $h_{\text{liq,i}}$) are then evaluated using the phase equilibrium relations, at the known pressure and concentration ($x_{\text{liq,i}}$).
- Finally, the residual energy is evaluated from the energy balance on the solution side (Equation (4.14)) and is used to update the vapor flow rate.

$$R_{\text{en}} = \dot{m}_{\text{liq,i+1}} h_{\text{liq,i+1}} + \dot{m}_{\text{vap,i-1}} h_{\text{vap,i-1}} + (\alpha A)_{\text{liq,i}} (T_{\text{w,i}} - T_{\text{liq,i}}) - \dot{m}_{\text{liq,i}} h_{\text{liq,i}} - \dot{m}_{\text{vap,i}} h_{\text{vap,i}} \tag{4.19}$$

$$d\dot{m}_{\text{vap,i}} = \frac{R_{\text{en}}}{(h_{\text{vap,i}} - h_{\text{liq,i}})} \tag{4.20}$$

Species balance and other subsequent steps are performed iteratively until convergence is reached for the residual energy. The iterative desorber solver algorithm consists of the following steps:

1. Receive liquid and vapor inlet properties such as flow rates, concentration, enthalpy, wall temperature and high-side pressure.

2. Guess the flow rates of liquid and vapor phases as shown in Equation (4.18).
3. Use the vapor-liquid equilibrium relations to determine vapor outlet properties such as temperature, concentration and enthalpy ($T_{vap,i}$, $x_{vap,i,}$ $h_{vap,i}$).
4. Apply the species balance (Equation (4.13)) and use liquid equilibrium relations to estimate liquid outlet properties ($x_{liq,i}$, $T_{liq,i}$ and $h_{liq,i}$).
5. Use the energy balance to evaluate heat transfer rate and energy residual (Equation (4.20)).
6. Update vapor flow rate using the energy residual, as shown in Equation (4.21).
7. Check for convergence and continue iteration (step 3) or terminate the solver.

The steps used in the desorber solver are summarized in Figure 4.7. The desorber heat transfer rate is calculated from the net rate of energy change for the solution side in the desorber.

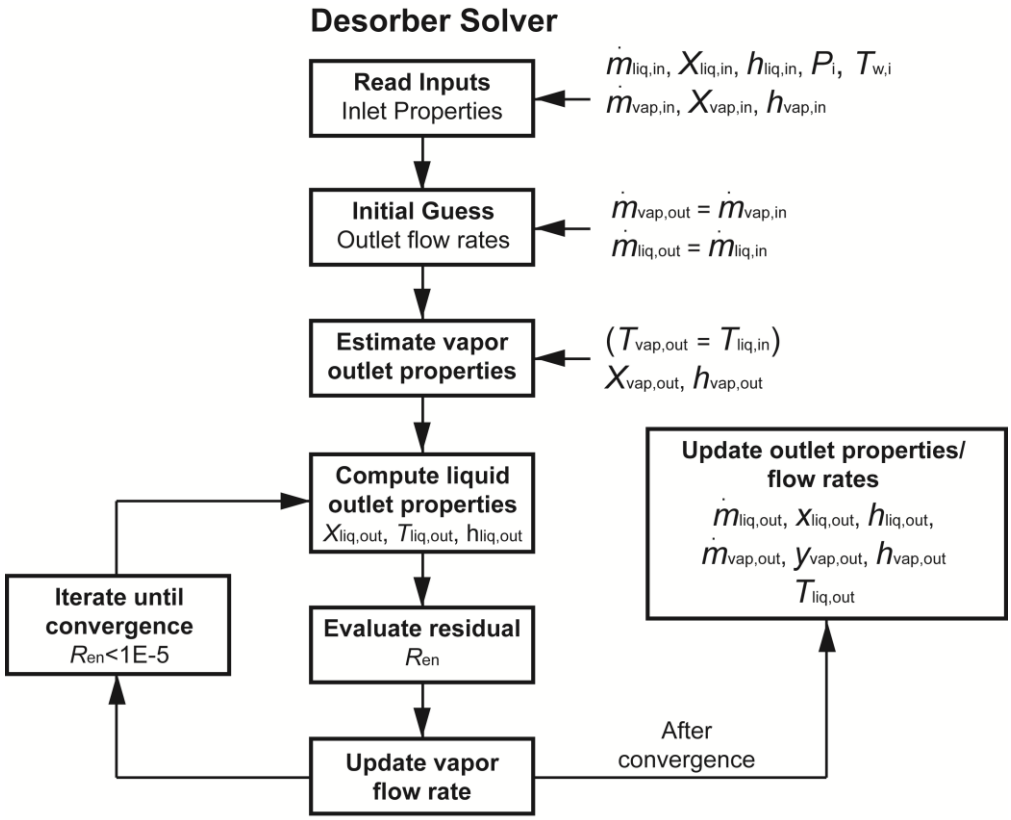

Figure 4.7 Desorber solver - flowchart

$$\dot{Q}_{DES} = \dot{m}_{19} h_{19} + \dot{m}_{16} h_{16} - \dot{m}_{15} h_{15} \tag{4.21}$$

Rectifier

A solution-cooled rectifier is considered in the current study in which heat is removed by the concentrated solution flowing from the pump. In this study, the rectifier outlet concentration is assumed fixed, to simplify the coupled heat and mass transfer analyses that would otherwise be required in this component. In concert with this assumption, no energy or mass storage is assumed in this component. The refrigerant concentration at the outlet of the rectifier is assumed to be 0.992. The assumption of constant outlet concentration is deemed acceptable for this system-level transient model. Component level modeling of the rectifier could incorporate detailed mass transfer modeling to predict the outlet concentration more accurately. Mass, species and energy balances are presented in Equations (4.23)-(4.26).

$$\dot{m}_{20} = \dot{m}_{21} + \dot{m}_{22} \tag{4.22}$$

$$\dot{m}_{20} x_{20} = \dot{m}_{21} x_{21} + \dot{m}_{22} x_{22} \tag{4.23}$$

$$\dot{Q}_{RECT} = \dot{m}_{20} h_{20} - \dot{m}_{21} h_{21} - \dot{m}_{22} h_{22} \tag{4.24}$$

$$\dot{Q}_{RECT} = \dot{m}_{11} h_{11} - \dot{m}_{10} h_{10} \tag{4.25}$$

4.3.7 Storage tank model

Mass storage is only modeled in the refrigerant and solution tanks. These simulated tanks allow for expansion and storage of fluid during transient conditions. The key assumptions employed in modeling the storage tank are as follows:

- The liquid and vapor phases are in thermodynamic equilibrium at each instant.
- The tank is well-mixed and fluid flowing out of the tanks are always saturated liquid.

- The pressures inside the tanks are transmitted to neighboring components in the cycle instantaneously.

The mass, concentration and specific internal energy of the mixtures inside the tanks are employed to determine the pressures and temperatures of mixtures using liquid-vapor equilibrium relations.

The equilibrium pressure inside the refrigerant tank is communicated to the high-side components (DES, COND, RECT, RHX and SHX) and the pressure inside the solution tank is communicated to the low-side components (ABS, RHX and EVAP), almost instantly.

Figure 4.8 represents the control volumes of the refrigerant and solution tanks. Mass, species and energy balances are carried out for the mixture inside the refrigerant tank and the solution tank.

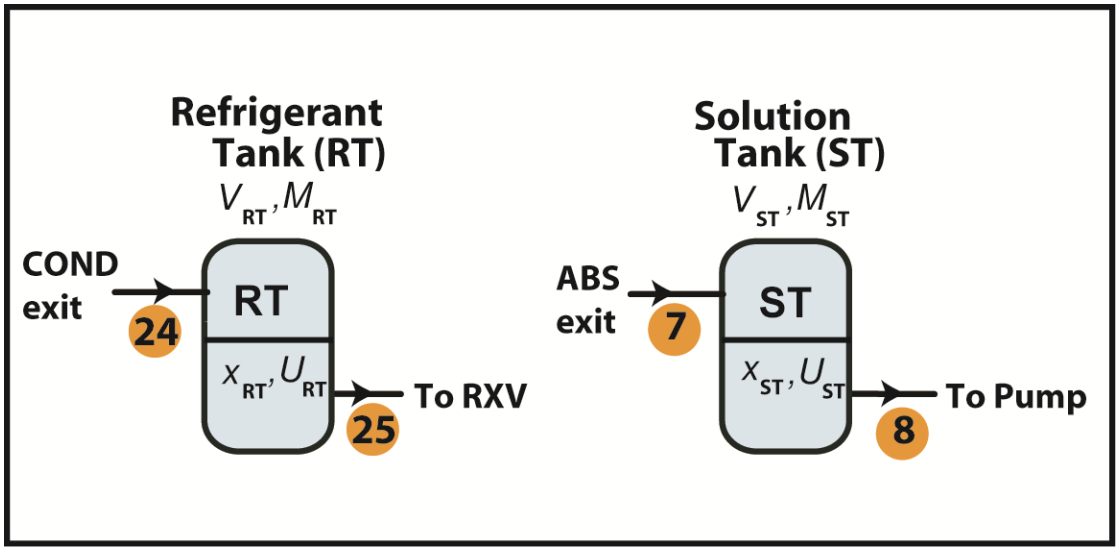

Figure 4.8 Storage tank - schematic

Conservation equations (4.27)-(4.29) are used to determine the properties of the solution inside the tanks (mass, concentration and enthalpy) at any instant.

$$\left(\frac{dm}{dt}\right)_{RT} = \dot{m}_{24} - \dot{m}_{25}; \quad \left(\frac{dm}{dt}\right)_{ST} = \dot{m}_{7} - \dot{m}_{8} \tag{4.26}$$

$$\left(\frac{d(mx)}{dt}\right)_{RT} = \dot{m}_{24}x_{24} - \dot{m}_{25}x_{25}; \quad \left(\frac{d(mx)}{dt}\right)_{ST} = \dot{m}_{7}x_{7} - \dot{m}_{8}x_{8} \tag{4.27}$$

$$\left(\frac{dU}{dt}\right)_{RT} = \dot{m}_{24}h_{24} - \dot{m}_{25}h_{25}; \quad \left(\frac{dU}{dt}\right)_{ST} = \dot{m}_{7}h_{7} - \dot{m}_{8}h_{8} \tag{4.28}$$

4.3.8 Expansion valve and pump

The flow rate of the refrigerant through the expansion valve is determined using a flow coefficient model. The model assumes the pressure difference across the valve as the driving force for the flow, and an adjustable flow coefficient, $C_{valve,}$ represents the relative valve restriction.

$$\dot{m}_{ref} = C_{valve} \cdot \sqrt{\Delta P} \tag{4.29}$$

The expansion valve in the line connecting the absorber and solution heat exchanger is modeled as a simple flow valve that causes a pressure reduction but does not affect the fluid flow rate.

A constant solution flow rate through the pump is assumed at all times. The positive displacement pumps typically employed in absorption chillers show little variation of flow rate with difference pressure; therefore, the constant flow rate pump assumption is applicable.

4.3.9 Thermodynamic properties

The thermodynamic properties of the saturated ammonia-water mixtures are evaluated using property routines developed by Rattner and Garimella (in preparation, 2013). These property routines enable fast and accurate evaluation of state points and, are easily accessible from the Matlab® and Simulink® environment.

4.3.10 Solution methods

Component models are developed as re-usable blocks in the Simulink® environment. The ordinary differential equations and other constitutive relations along with the property calls are solved in the Simulink® environment and integrated using the Runge-Kutta algorithm. The time step for numerical integration is limited to a maximum of 0.5 s, and is automatically adjusted to satisfy the relative tolerance of 1×10^{-3} for the residuals of dependent variables.

4.3.11 Sensitivity analysis

An analysis of the sensitivity of the dynamic performance predictions to the number of heat exchanger segments was conducted. Four different cases were simulated and the heat transfer rates in the components during steady state were compared for these cases. The model was simulated using a valve coefficient of $c_{\text{valve}} = 2.51\times10^{-6}$ kg s^{-1}Pa$^{-0.5}$ and reduced wall thermal masses of the components wall ($(Mc_{\text{p}})_{\text{w}} = 1000$ J K^{-1}) allowing the parameters to reach steady state at t = 350 s. Table 4.3 shows the heat transfer rates for different components during steady state when the number of segments was varied.

Cases 1 and 2 represent an increase in the number of segments (N) for evaporator, condenser and absorber from baseline (N = 5) to N = 8 and N = 10 respectively, while the number of segments is maintained at N = 3 for SHX, RHX and desorber. It can be seen that the variation of heat transfer rates is less than 2% for all the components, except for the RHX, where a 25% decrease in the heat transfer rate is observed. The decrease can be attributed to a lower value of low-side pressure during steady state for these cases (~440 kPa) than for the baseline (~ 460 kPa). A higher evaporator glide ($T_{\text{glide}} = T_{\text{evap,out}} - T_{\text{evap,in}}$) is observed at lower pressures for the ammonia-water mixture. For the baseline case, the evaporator glide observed is 3.5 K and an evaporator outlet temperature of 7.4°C, whereas the glide and evaporator outlet temperatures for

Table 4.3 Sensitivity analysis

	Description	Units	Parameter	Component					
				EVAP	COND	ABS	DES	SHX	RHX
Baseline	Number of segments	-	N	5	5	5	3	3	3
	Heat transfer rates	kW	$\dot{Q}$	3.42	3.58	5.49	5.66	2.48	0.43
	Pressure	kPa	P_{high}			1954			
			P_{low}			466			
Case 1	Number of segments	-	N	8	8	8	3	3	3
	Heat transfer rates	kW	$\dot{Q}$	3.45	3.58	5.55	5.67	2.50	0.32
	Deviation from baseline (%)	-	-	0.88	0.00	1.09	0.18	0.80	-25.60
	Pressure	kPa	P_{high}			1924			
			P_{low}			445			
Case 2	Number of segments	-	N	10	10	10	3	3	3
	Heat transfer rates	kW	$\dot{Q}$	3.45	3.57	5.56	5.68	2.51	0.32
	Deviation from baseline (%)	-	-	0.88	-0.28	1.27	0.35	1.2	-25.6
	Pressure	kPa	P_{high}			1913			
			P_{low}			439			
Case 3	Number of segments	-	N	5	5	5	5	5	5
	Heat transfer rates	kW	$\dot{Q}$	3.52	3.62	5.53	5.63	2.75	0.37
	Deviation from baseline (%)	-	-	2.92	1.11	0.73	-0.53	10.9	-11.11
	Pressure	kPa	P_{high}			1960			
			P_{low}			440			

cases 1 and 2 are equal to 10.2 K and 12.5°C, respectively. This leads to a higher temperature of the refrigerant at the inlet of the RHX and hence a reduced RHX heat transfer rate. The large magnitude of variation is due to the low baseline value of the RHX heat transfer rate (0.43 kW).

Case 3 represents an increase in the number of segments for the desorber, SHX and RHX (N = 3 to N = 5), while maintaining the number of segments for the evaporator, condenser and

absorber (N = 5). The high-side pressure value is nearly the same (1955 kPa) as for the baseline case, whereas the low-side pressure (440 kPa) is lower than the baseline value (466 kPa). A maximum absolute variation of 11.1 % is observed in the RHX heat transfer rate, whereas the SHX heat transfer rate for case 3 is 10.9 % higher than that for the baseline case. A lower low-side pressure leads to a higher evaporator glide (9.4 K) and a greater refrigerant temperature of 11.5°C at the evaporator outlet for Case 3, and hence a lower RHX heat transfer rate. The ammonia concentration of concentrated solution in Case 3 is 0.46, compared to a solution concentration of 0.48 for the baseline case. Hence, a higher SHX heat transfer rate (2.75 kW) is needed to raise the temperature of the concentrated solution in Case 3, compared to the baseline case (2.48 kW).

Overall, it is seen that increasing the number of segments in the components increases the evaporator duty due to lower low-side pressure, and thereby saturation temperature. Increasing the number of segments in the desorber, RHX and SHX has a stronger effect on the evaporator duty than the increase in the evaporator, condenser and absorber segments. For the dynamic start up, the baseline case is chosen as the representative case due to its relatively lower computational time requirement. Also, it is to be noted an optimal evaporator glide (3.5 K) is achieved using the baseline case, although the requirement of 1 RT (3.52 kW) is not exactly met during steady state (3.42 kW).

5. RESULTS AND DISCUSSION

This chapter summarizes the results on dynamic performance of a single-effect ammonia-water absorption chiller obtained using the dynamic model described in Chapter 4.

First, the dynamic model is used to simulate the start-up process of a single-effect ammonia-water absorption chiller from ambient conditions. Second, the chiller performance during steady state is compared with the results from the steady state model (Chapter 3). Finally, a detailed study on system response is performed by observing the variation in key output parameters (e.g., flow rates, concentration, heat transfer rates and others) in response to changing operating conditions.

5.1 Transient start-up of the absorption chiller

The transient start-up behavior of the modeled absorption chiller is analyzed in this section. The initial conditions and other transient model parameters are listed in Table 5.1.

The initial temperature of 20°C and specified mass of solution and refrigerant fixes the

Table 5.1 Initial Conditions

Quantity	Value
Temperature (°C)	20
Pressure (kPa)	400
Volume of tanks (L)	5
Mass of solution (g)	142
Mass of refrigerant (g)	142
Vapor quality of mixture in tanks (-)	0.1
Pumping rate (g s^{-1})	9.75
Valve coefficient (kg s^{-1} $Pa^{-0.5}$)	2.51×10^{-6}

initial system pressure of 400 kPa. A constant flow rate of solution through the pump, $\dot{m}_8 = 0.00975$ kg s^{-1}, is applied at all times. An initial vapor quality of 0.1 is established in the refrigerant and solution tanks based on an initial mass of solution (140 g), mass of ammonia (92.4 g) and total internal energy of fluid in the tank (-523.01 J).

The inlet temperatures of the coupling fluids are smoothly ramped from 20°C to their steady state values during the first ninety seconds of start-up to minimize the influence of the thermal behavior of the auxiliary systems on the absorption system transient results. The steady state values of the coupling fluid temperatures after ninety seconds of start-up are summarized in Table 5.2. The coupling fluid temperature at the desorber inlet is smoothly ramped to its steady-

Table 5.2 Coupling fluid inlet temperatures

Component	Temperature of coupling fluid	Units
Evaporator	12.77	°C
Desorber	176.6	°C
Condenser	40	°C
Absorber	40	°C

state value within the first minute of start-up.

The coupling fluid temperatures at the inlets of the components during steady state are matched with those in the steady state model (Chapter 3). As explained earlier, the objective is to study the chiller start-up and then compare the steady state performance predicted by the transient and steady state models.

The transient model is simulated with the input parameters explained earlier. The transient performance of an absorption chiller can be characterized in terms of its time-varying

heating and cooling duties, pressures, concentrations, and flow rates. This transient performance is illustrated in the following sections.

5.1.1 Variations of system pressure and temperature

The pressure and refrigerant flow rate (across valve) variations during start-up are shown in Figure 5.1. It was stated earlier that the initial pressure in the system is 400 kPa.

The high-side pressure increases from 400 kPa to 1956 kPa from t = 0 to t = 550 s. The increase in the high-side pressure is expected during start-up. The increase in the desorber heat transfer rate results in an increased vapor generation in the desorber. Hot refrigerant vapor enters the condenser, but is not condensed completely. This is because of a low cooling rate in the condenser during first 90 s due to a relatively small difference in temperature between the refrigerant vapor and the coupling fluid, as seen in Figure 5.2. This allows high energy fluid (vapor/two-phase) to enter the refrigerant tank downstream of the condenser. Thus, an increase in the vapor pressure of the refrigerant tank is communicated to other high-side components as

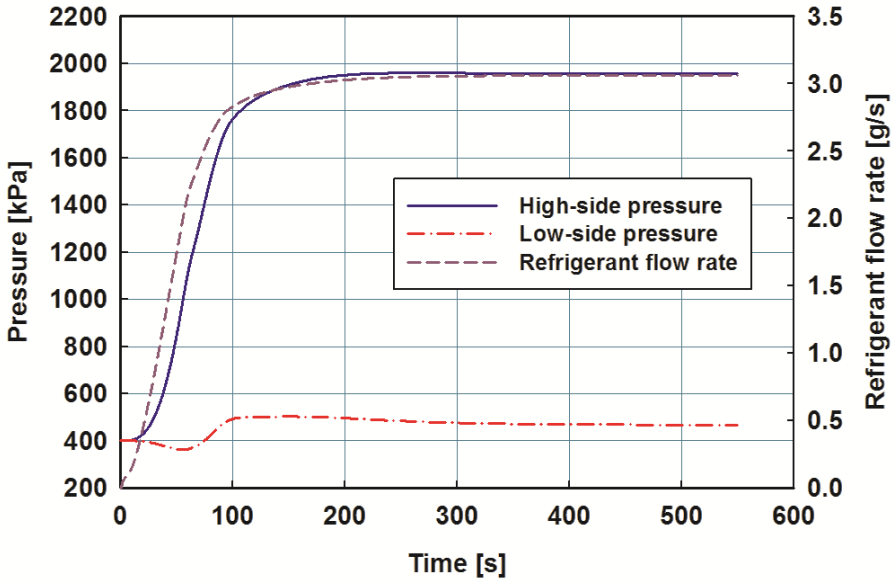

Figure 5.1 Variation of system pressure and refrigerant flow rate during start-up

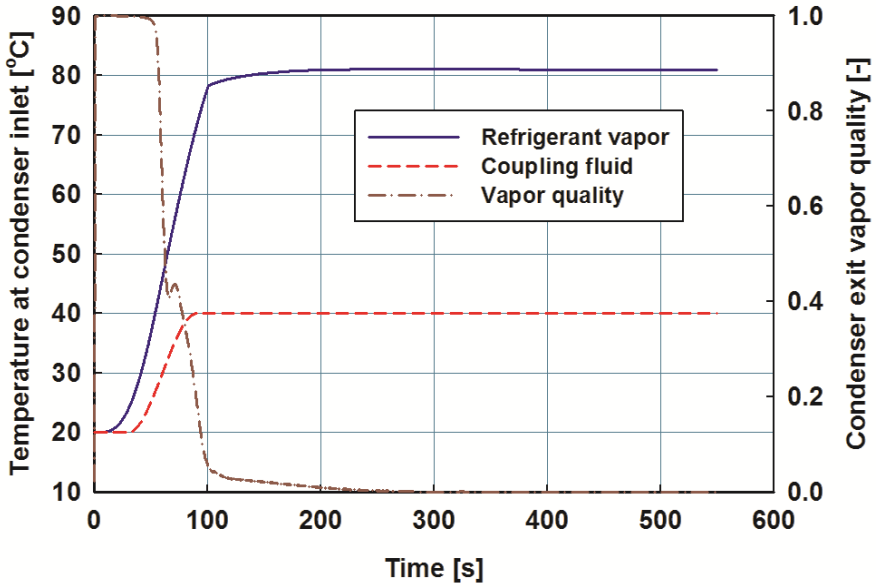

Figure 5.2 Variation of condenser temperature and exit quality during start-up

an increase in the high-side pressure. The rate of increase in the high-side pressure decreases after the first minute, as can be seen from the shift in the slope of high-side pressure variation at t ~ 60 s. This is because of a steep drop in the condenser exit vapor quality at t ~ 60 s, as shown in Figure 5.2. The high-side pressure variation decreases after t = 100 s when the exit vapor quality approaches zero (~ 0.1).

The low-side pressure increases from 400 kPa to 468 kPa from t = 0 to t = 550 s. The low-side pressure decreases initially, which can be attributed to an instantaneous increase in the solution pumping rate (0 to 9.75 g s^{-1}) at t = 0. A constant pumping rate, coupled with a low initial refrigerant flow rate across the valve (Figure 5.1) draws solution out of the solution tank, and reduces the pressure inside the solution tank. It is communicated as a decrease in the low-side pressure to other components.

An increase in the low-side pressure after t ~ 60 s can be understood as a direct consequence of an increase in the absorber fluid outlet temperature as shown in Figure 5.3. A peak is observed in the low-side pressure at t ~124 s due to a local peak in the absorber fluid

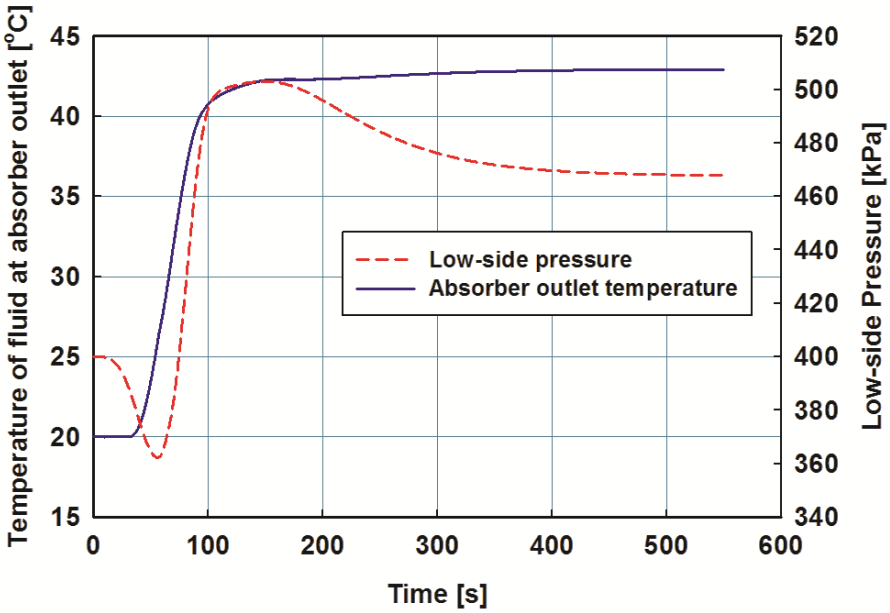

Figure 5.3 Variations of absorber fluid outlet temperature and low-side pressure during start-up

outlet temperature (Figure 5.3), and thereby an increased energy of fluid flowing into the solution tank. However, an eventual decrease in the ammonia concentration due to constant solution outflow from the tank lowers the pressure in the solution tank, and thus, the low-side pressure decreases later to 468 kPa at steady state (t = 550 s).

It can be seen that the high-side pressure dynamics are much faster than the low-side dynamics. The high-side pressure variation settles to within 2% of its steady-state value in ~ 300 s, whereas the low-side pressure variation takes ~ 500 s to settle to within 2% of its steady-state value. Hence, the system is governed by two distinct time responses.

The refrigerant flow rate across the valve is represented in Figure 5.1. It increases from 0 to 3.06 g s^{-1} from t = 0 to t = 550 s. This is governed solely by the pressure difference across the valve for a fixed valve setting. An increase in the pressure difference increases the refrigerant flow rate. The rate of increase in the flow rate decreases at t = 200 s because the high-side pressure reaches a nearly constant value at t = 200 s, and the low-side pressure does not change appreciably after t = 200 s.

Figure 5.2 represents the variations in the temperatures of coupling fluid and refrigerant vapor at the condenser inlet. Also, the condenser exit vapor quality is shown on the right y-axis. The coupling fluid temperature is ramped from 20°C to 40°C from t = 0 to t = 90 s. The condenser vapor inlet temperature increases steeply from 20°C to 80°C from t = 20 s to t = 100 s as the refrigerant vapor generated in the desorber enters the condenser. The rate of increase in the refrigerant vapor temperature at the inlet of the condenser is significantly reduced after t ~ 100 s (Figure 5.2) as the condenser exit vapor quality decreases to a low value (~ 0.1).

The condenser exit quality increases quickly from 0.02 to 0.99 from t = 0 to t = 1 s. The slight delay is due to the desorber wall thermal mass, which causes a delay in vapor generation in the desorber. The quality stays high until t ~ 60 s when a significant difference in the vapor inlet temperature and coupling fluid temperature results in cooling of the refrigerant vapor in the condenser. There is a local peak at t ~ 70 s due to condenser thermal mass, which causes a slight delay in the cooling of the refrigerant vapor. However, as the refrigerant vapor temperature

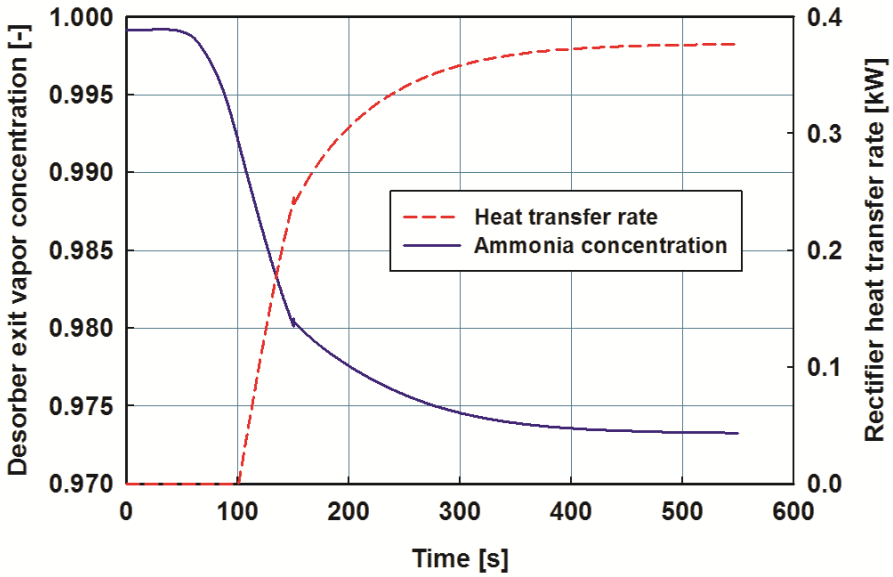

Figure 5.4 Variation of desorber vapor outlet concentration and rectifier heat transfer rate during start-up

increases, and the condenser thermal mass is overcome, the vapor quality decreases to zero at t ~ 300 s.

Figure 5.4 represents the heat transfer rate in the rectifier and ammonia concentration of refrigerant vapor at the desorber outlet. In practice, the rectifier also adds a thermal lag due to cooling of refrigerant vapor in the rectifier before it reaches the condenser. But the present rectifier model assumes saturated vapor states at the inlet and outlet of the rectifier, and a constant outlet vapor outlet concentration of 0.992. A high ammonia concentration (~ 0.999) for the refrigerant vapor at the desorber outlet during first 100 s results in zero rectifier cooling until the concentration drops below 0.992 at t ~ 100 s, as shown in Figure 5.4. The decrease in ammonia concentration is understandable as a larger fraction of water is vaporized in the desorber at higher temperatures and pressures. A slight oscillation in the ammonia concentration at t ~ 167 s can be attributed to an oscillation during property estimation in the rectifier at that instant.

5.1.2 Variation of system flow rates

The variations in the refrigerant, concentrated solution and dilute solution flow rates are shown in Figure 5.5. The flow rate of refrigerant exiting the desorber is also shown in Figure 5.5.

The flow rate of the concentrated solution is maintained at a constant value of 9.75 g s^{-1} by the solution pump. The dilute solution flow rate decreases from to 9.75 g s^{-1} to 6.69 g s^{-1} from t = 0 to t = 550 s. The dilute solution flow rate at time t = 0 is equal to the pumping rate. This is as expected because there is no vapor generation in the desorber at t = 0. As time progresses, an increase in the desorber heating rate increases the vapor generation, resulting in a decrease in the returning dilute solution flow rate. The flow rate of the refrigerant vapor generated in the desorber increases from 0 to 3.18 g s^{-1} from t = 0 to t = 550 s. The increase in the refrigerant

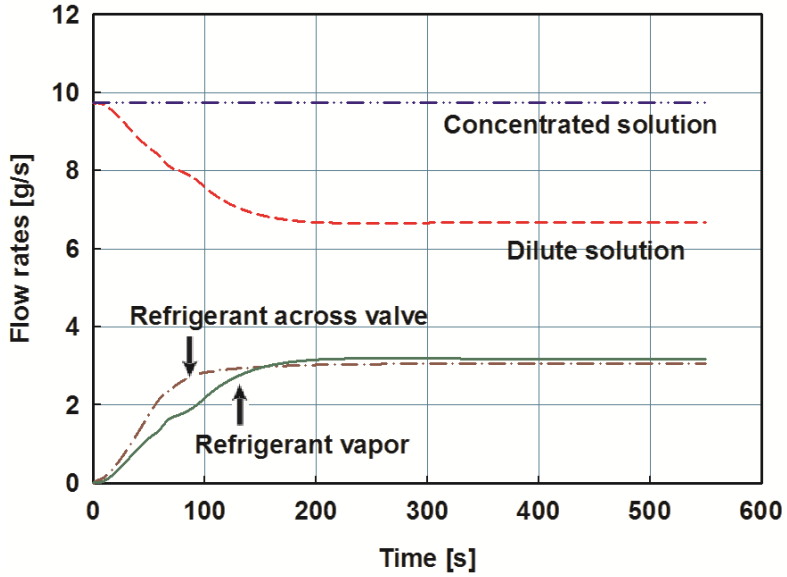

Figure 5.5 Variations of system flow rates during start-up

vapor flow rate is a direct consequence of increased heat transfer rate and resultant vapor generation in the desorber. The variation of refrigerant flow rate across the valve was explained earlier along with the system pressure variation. The refrigerant flow rate across the valve increases from 0 to 3.06 g s^{-1} from t = 0 to t = 550 s.

Changes in slope are observed at t = 62 s for the flow rates of refrigerant vapor and dilute solution. This is because of the change in slope in the high-side pressure variation at that instant (Figure 5.1). Another change in slope is seen at t = 84 s which could be attributed to the desorber wall thermal mass, which delays the heat transfer rate between the desorber wall and solution. The delay in heat transfer reduces the rate of vapor generation, and thereby increases the dilute solution flow rate and lowers the refrigerant vapor flow rate.

5.1.3 Variation of system concentration during start up

The variations in the ammonia concentration of the refrigerant, concentrated solution, and dilute solution are shown in Figure 5.6.

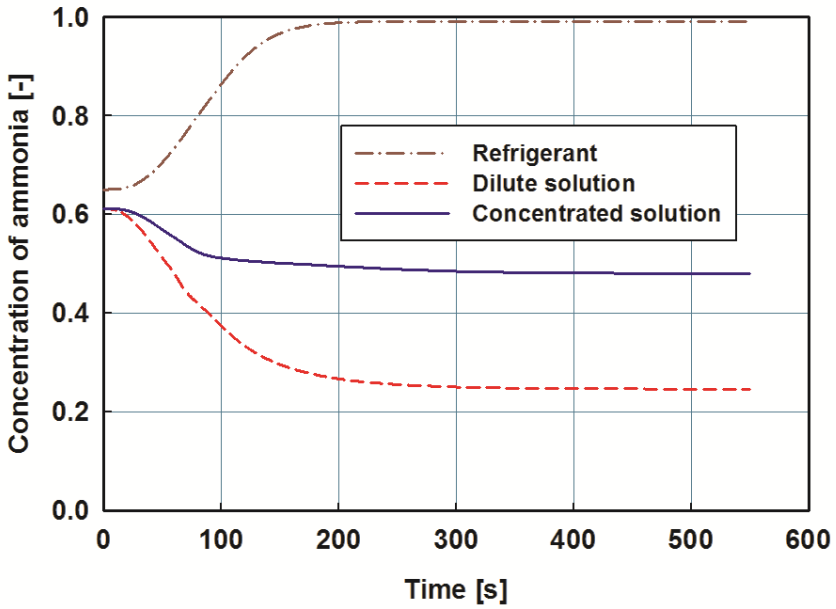

Figure 5.6 Variations of ammonia concentration in the system during start-up

The concentration of refrigerant increases from 0.650 to 0.992 from t = 0 to t = 550 s due to the increased vapor generation in the desorber during start-up. The higher rate of ammonia-vapor entry into the refrigerant tank increases the overall concentration inside the refrigerant tank. The concentration of refrigerant is assumed equal to the well-mixed tank concentration and thus, an increase is observed during start-up. As the concentration of liquid refrigerant from the refrigerant tank increases, it compensates for the decrease in ammonia concentration inside the solution tank. This is reflected as a decrease in the slope of the concentrated solution concentration at t ~ 90 s (Figure 5.6). The refrigerant concentration reaches a near constant value at t ~ 200 s due to the high-side pressure and refrigerant flow rate nearing their steady state values at t ~ 200 s (Figure 5.1).

The concentrated solution concentration decreases from 0.612 to 0.481 from t = 0 to t = 550 s (Figure 5.6). The decrease in concentration of the concentrated solution is due to the constant pumping rate of solution from the tank, which depletes ammonia from the solution tank

during start-up. The concentrated solution concentration shown is the liquid-phase concentration of the solution pumped from the solution tank. The refrigerant flow evolves slowly with time, thus gradually reflecting the difference in concentration between the concentrated and returning dilute solution.

The dilute solution concentration decreases from 0.612 at t = 0 to 0.246 from t = 0 to t = 550 s (Figure 5.6). Initially, there is no vapor generation in the desorber and thus, the returning dilute solution carries the same ammonia content as the incoming concentrated solution. As time progresses, the decrease is expected because of the increased vapor generation in the desorber during start-up. An increased vapor generation decreases the ammonia fraction in the returning solution, and a corresponding decrease in the dilute solution concentration is observed. A change in slope is observed in the dilute solution concentration at t ~ 62 s due to the similar variation in the slope of the high-side pressure at that instant (Figure 5.1).

5.1.4 Heat transfer rates and COP variation

The variations of heat transfer rates for major components such as the evaporator, condenser, desorber and absorber during start-up of the chiller are shown in Figure 5.7. Also, the evolution of recuperative heat transfer rates is shown.

The evaporator and desorber heat transfer rates during start-up are shown as positive values because heat is entering the system, while the condenser and absorber cooling rates are shown as negative values. The recuperative heat exchangers experience both heating and cooling. However, when the system is not at steady state, the two values are different due to thermal storage in the heat exchanger wall.

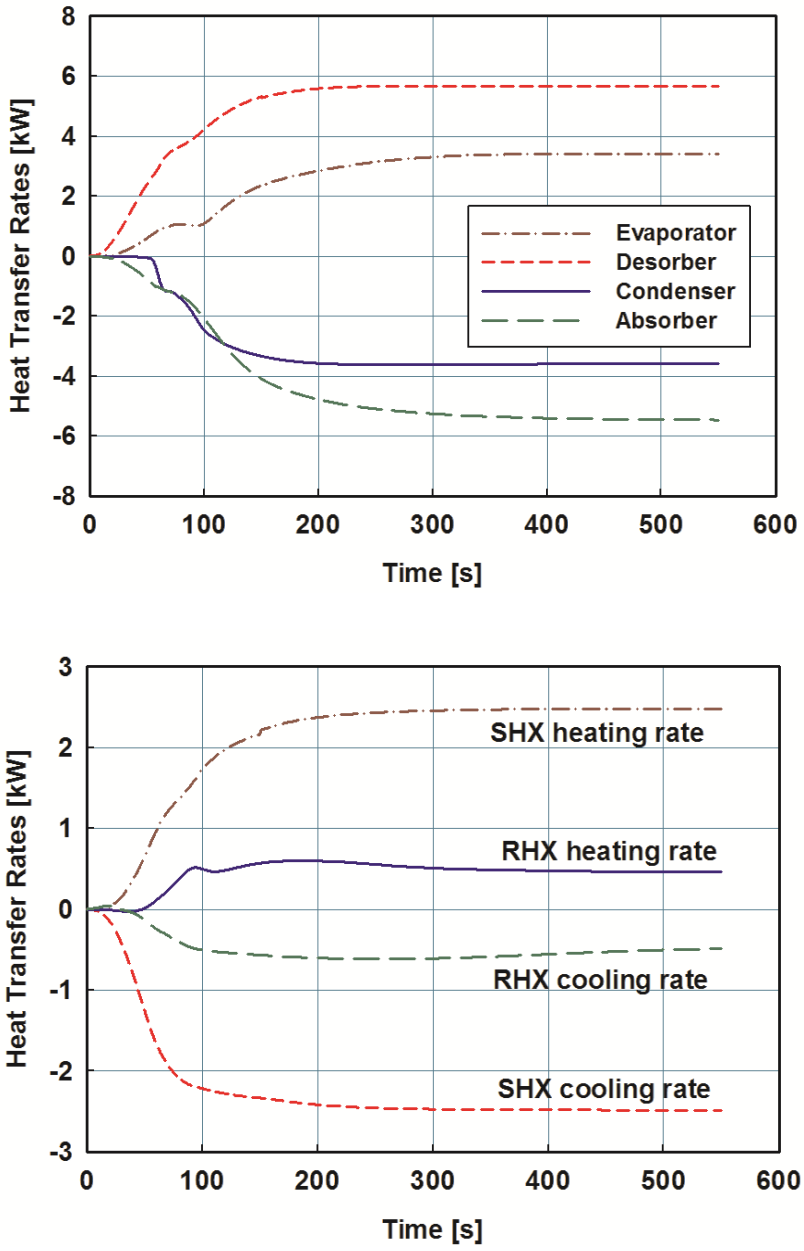

Figure 5.7 Variations of heat transfer rates in the system during start-up

It is found that during start-up, the desorber heat transfer rate rises sharply, followed by the absorber heat transfer rate, whereas the evaporator and condenser heat transfer rates evolve slowly. The desorber heat transfer rate increases from 0 to 5.66 kW, whereas the evaporator heat transfer rate increases from 0 to 3.41 kW, from t = 0 to t = 550 s. The condenser heat transfer

rate increases from 0 to 3.59 kW, while the absorber heat transfer rate increases to 5.46 kW from t = 0 to t = 550 s. The heating and cooling rates in the SHX reach 2.48 kW at t = 550 s, whereas the heating and cooling rates in the RHX rise to 0.46 kW and 0.48 kW respectively at t = 550 s.

The rapid increase in the desorber heat transfer rate is understandable, because the coupling fluid in the desorber is heated up to a temperature of approximately 176°C within t = 60 s. This results in a high heat transfer rate in the desorber (Figure 5.7) and vapor generation in the first minute of start-up. A change in slope is observed in the desorber heating rate at t ~ 70 s, due to a change in slope of the high-side pressure observed at the same time instant (Figure 5.1). The cooling rate in the absorber rises relatively slowly but it is expected because there is not much absorption taking place initially because of low rate of refrigerant flow across the valve and into the absorber (Figure 5.5), during the first few seconds of the start-up. The slope of the absorber heat transfer rate increases sharply at t ~ 59 s due to a steep increase in the low-side pressure at that instant (Figure 5.3).

The vapor from the desorber flows into the condenser and raises its temperature as shown in Figure 5.2. The vapor does not condense completely because of wall thermal mass, and resultant heat absorption by the condenser wall, resulting in a zero condenser heat transfer rate until t ~ 43 s. Therefore, a two-phase mixture exits the condenser and enters the refrigerant tank during start-up (Figure 5.2). The vapor accumulates in the refrigerant tank and increases the high-side pressure (Figure 5.1), and thereby the condenser inlet temperature (Figure 5.2). An increase in the condenser inlet temperature and increased refrigerant vapor generation increase the condenser heat transfer rate. A sharp change in slope is observed in the condenser duty at t ~ 70 s due to a sharp decrease in the condenser exit quality at that instant (Figure 5.2). The liquid refrigerant drains out of the refrigerant tank and flows through the expansion device to the

evaporator. The pressure difference across the valve governs the refrigerant flow rate. The pressure difference is initially zero, therefore the refrigerant flow rate starts at zero and increases as the high-side pressure rises (Figure 5.1). The evaporator temperature is close to the ambient temperature during start-up, as shown in Figure 5.8. The evaporator pressure decreases as the high-side pressure increases and more liquid-phase refrigerant is expanded from the refrigerant tank to the evaporator pressure. As a result, the evaporator heat transfer rate is low during the first minute of operation (Figure 5.7). The refrigerant from the evaporator outlet is further heated in the RHX before it reaches the absorber.

It can be observed from Figure 5.8 that the evaporator temperature has a change in slope at t ~ 29 s, and a local minimum and maximum at t ~ 70 s and t ~ 97 s respectively. These variations can be attributed to similar changes in slope for the low-side pressure, although those are observed slightly earlier. Slope changes in the refrigerant inlet temperature at the evaporator (Figure 5.8) are reflected as slope changes in the evaporator heat transfer rate (Figure 5.7).

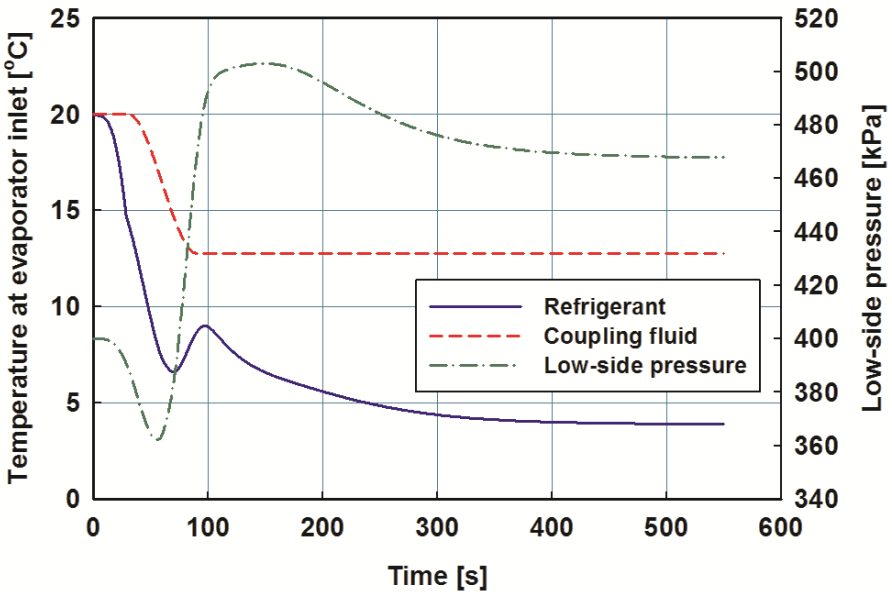

Figure 5.8 Variations of refrigerant and coupling fluid temperature at inlet of evaporator during start-up

Figure 5.7 also shows variations in SHX and RHX heating and cooling rates. The SHX cooling rate increases faster than the heating rate due to thermal mass of SHX wall which delays the heat transfer between the hot returning dilute solution from the desorber, and the concentrated solution from the rectifier. A change in slope observed in the SHX heating rate at t ~ 60 s can be attributed to a change in slope for the high-side pressure at that instant (Figure 5.1). For the RHX, a change of slope in its heating rate is observed at t ~ 90 s, and the heating rate increases from 0.47 kW to 0.59 kW from t = 115 s to t = 180 s, and later reduces to 0.46 kW at t = 550 s. These variations can be attributed to RHX thermal mass which causes a delay in the heat transfer and similar slope variations for the low-side pressure (Figure 5.2).

Figure 5.9 represents the evaporator cooling duty, desorber heat duty and COP of the system during start up. The COP is the ratio of evaporator cooling duty to desorber heat transfer rate. The cooling duty of the evaporator increases from 0 to 3.41 kW from t = 0 to t = 550 s, while the desorber duty increases from 0 to 5.66 kW. The variations of the evaporator and desorber heat transfer rates were discussed earlier in this section. The COP of the chiller increases from 0 to 0.602 from t = 0 to t = 550 s. A local maximum and minimum are observed in COP variation at t ~ 67 s and t ~ 98 s, respectively. These variations in COP are due to a similar peak and valley observed in the evaporator cooling duty at these instants (Figure 5.9). The change in slope at t ~ 70 s in COP variation is due to a similar slope change observed in the desorber duty. The time taken for the cooling capacity variation to settle to within 2% of its steady-state value is 320 s.

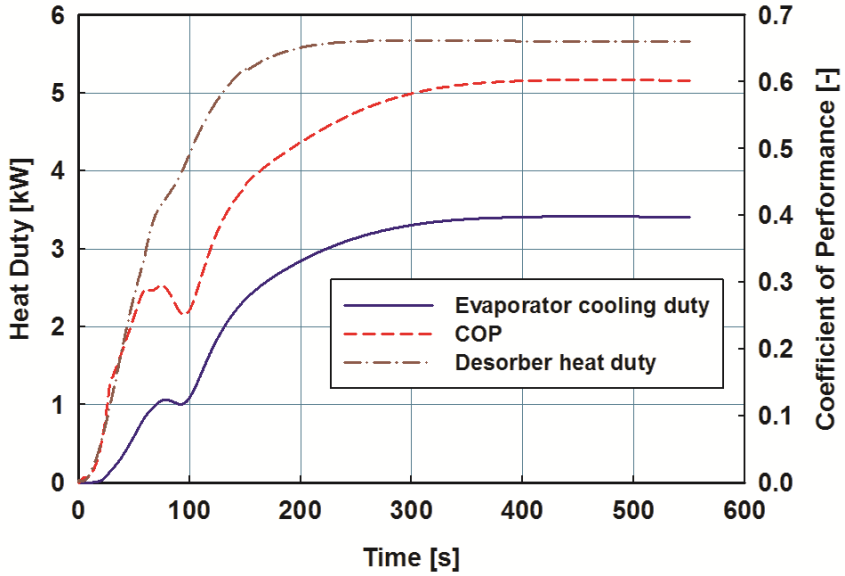

Figure 5.9 Variations of evaporator cooling capacity, desorber heat input, and COP during start-up

5.2 Steady state performance

The steady state behavior of the dynamic model is compared with the results from a previously developed steady state system model (Determan and Garimella, 2012) with equivalent configuration and operating parameters.

Output values from the dynamic model are assumed to be at steady state by t = 550 s, because the system pressures, concentrations, flow rates and heat transfer rates have attained their steady state values.

5.2.1 Mass and species balance

There are primarily three different mass flow rates and concentrations involved in the absorption chiller. The flow rates and concentrations of the refrigerant across the valve, concentrated solution, and dilute solution must balance during steady state.

From the transient model, the mass flow rate of the refrigerant flowing across the valve during steady state is 3.062 g s^{-1}, the flow rate of the concentrated solution is 9.750 g s^{-1} and the

flow rate of dilute solution is 6.687 g s^{-1}. The net mass imbalance after t = 550 s is shown in Equation (5.1).

$$\begin{aligned} \dot{m}_{imb} &= \dot{m}_{conc} - \dot{m}_{ref} - \dot{m}_{dil} \\ \dot{m}_{imb} &= (9.750 \text{ g s}^{-1} - 3.062 \text{ g s}^{-1} - 6.687 \text{ g s}^{-1}) \\ \dot{m}_{imb} &= 0.001 \text{ g s}^{-1} \end{aligned} \tag{4.30}$$

A mass imbalance of 0.001 g s^{-1} (0.01% of concentration solution flow) is observed after t = 550 s due to the attainment of near steady state by the chiller variables. The mass imbalance is a direct consequence of storage in the refrigerant and solution tanks. The imbalance in flow rate is 0.03 % of the refrigerant flow rate during steady state, and thus can be considered acceptable.

The steady state concentration of refrigerant exiting the refrigerant tank, flowing toward the evaporator, is 0.9920. The concentration of the concentrated solution pumped out of the solution tank during steady state is 0.4805. The steady-state dilute solution concentration is 0.2463. The net species imbalance after t = 550 s is estimated using Equation (5.2).

$$\begin{aligned} \dot{m}_{amm,imb} &= \dot{m}_{conc} x_{conc} - \dot{m}_{ref} x_{ref} - \dot{m}_{dil} x_{dil} \\ \dot{m}_{amm,imb} &= (9.75 \text{ g s}^{-1} \cdot 0.4805 - 3.062 \text{ g s}^{-1} \cdot 0.9920 - 6.687 \text{ g s}^{-1} \cdot 0.2463) \\ \dot{m}_{amm,imb} &= 0.0003 \text{ g s}^{-1} \end{aligned} \tag{4.31}$$

An imbalance of 0.0003 g s^{-1} (0.003% of concentrated solution flow rate) is observed in the ammonia flow rate in the chiller, which can be considered negligible. . The system attains near steady state at t = 550 s, because most of the system parameters such as system pressures, flow rates and concentrations attain values close to their steady state values.

5.2.2 Energy balance

The component heat transfer rates are due to differences in states of the refrigerant/solution stream between the outlet and inlet states. The energy imbalance of the entire

chiller is estimated from the algebraic sum of heat transfer rates during steady state, and implies thermal energy storage in the heat exchangers and the fluids due to their thermal masses.

The start-up performance of the chiller was demonstrated in a previous section. As stated earlier, the evaporator heat transfer rate at t = 550 s is 3.410 kW, whereas the desorber heat transfer rate is 5.663 kW. The absorber and condenser cooling rates at t = 550 s are estimated to be 5.459 kW and 3.590 kW respectively. The heating and cooling rates in the SHX are estimated to be 2.481 kW each, while the heating and cooling rates of RHX are 0.461 kW and 0.485 kW, respectively.

The other heat exchanging component is a solution cooled rectifier. The rectifier does not contribute to the energy imbalance due to the assumption that it has a negligible thermal mass, and hence is not included in the computation. Assuming a pump efficiency of 0.7, the work done by the pump is calculated as follows:

$$\begin{aligned} &\dot{W}_{\mathrm{P}} = \dot{m}_{\mathrm{conc}}(v\Delta P)/\eta_{\mathrm{P}}\,;\dot{m}_{\mathrm{conc}} = 9.75\times10^{-3}\,\mathrm{kg\ s^{-1}};v = 0.0012\ \mathrm{m^3\ kg^{-1}} \\ &\Delta P = (1956-468)\ \mathrm{kPa};\ \eta_{\mathrm{P}} = 0.7 \\ &\dot{W}_{\mathrm{P}} = 0.017\ \mathrm{kW} \end{aligned} \tag{4.32}$$

The net energy imbalance is estimated as shown in Equation (5.4).

$$\begin{aligned} \dot{Q}_{\mathrm{net}} &= \dot{Q}_{\mathrm{evap}} + \dot{Q}_{\mathrm{des}} - \dot{Q}_{\mathrm{cond}} - \dot{Q}_{\mathrm{abs}} - \dot{Q}_{\mathrm{RHX,cool}} + \dot{Q}_{\mathrm{RHX,heat}} - \dot{Q}_{\mathrm{SHX,cool}} + \dot{Q}_{\mathrm{SHX,heat}} \\ &\quad - \dot{W}_{\mathrm{P}} \\ \dot{Q}_{\mathrm{net}} &= (3.410 + 5.663 - 3.590 - 5.459 + 0.485 - 0.461 + 2.481 - 2.481 \\ &\quad - 0.017)\ \mathrm{kW} \\ \dot{Q}_{\mathrm{net}} &= 0.031\ \mathrm{kW} \end{aligned} \tag{4.33}$$

A net heat imbalance of 0.031 kW is observed after t = 550 s. The imbalance is less than 1% of the evaporator cooling capacity (3.41 kW).

5.2.3 Steady state comparison

From the mass and energy imbalance analysis, the results obtained for the chiller parameters after 550 s are assumed to represent steady-state behavior of the chiller. The results are summarized in Table 5.3, where they are compared with the steady state model results from Chapter 3.

It can be seen that these values match closely with the results from the steady- state system model. The cooling duty of the evaporator estimated from the dynamic model is 3.41 kW

Table 5.3 Steady-state comparison

Quantity	Dynamic Model	Steady-state Model	Percent deviation
Desorber heat load (kW)	5.66	5.44	4.0
Absorber heat load (kW)	5.46	5.62	- 2.8
Evaporator heat load (kW)	3.41	3.54	- 3.7
Condenser heat load (kW)	3.59	3.39	5.9
Coefficient of Performance (-)	0.60	0.65	- 7.7
Flow rate of concentrated solution (g s^{-1})	9.75	9.75	-
Flow rate of dilute solution (g s^{-1})	6.69	6.66	0.5
Flow rate of refrigerant (g s^{-1})	3.06	3.09	- 0.1
High-side pressure (kPa)	1956	2094	- 6.5
Low-side pressure (kPa)	468	501	- 6.5
Concentration of ammonia vapor (-)	0.992	0.9985	- 0.7
Concentration of ammonia-rich solution (-)	0.481	0.478	0.6
Concentration of dilute solution (-)	0.246	0.237	3.8

which is slightly less than the desired 3.52 kW (1 RT).

An important factor contributing to this disparity is the assumed refrigerant concentration at the outlet of the rectifier. The steady state system model assumes a relatively higher refrigerant concentration of 0.9985. The dynamic model assumes a refrigerant concentration of 0.992 at the rectifier outlet to avoid problems of stability at high concentrations during ammonia-water property estimations. At 470 kPa, a refrigerant concentration of 0.992 corresponds to a dew point temperature of 46.4°C, whereas a concentration of 0.9985 at the same pressure results in a dew point temperature of 28.1°C, despite similar bubble point temperatures of -1.7°C and -0.4°C, respectively. Thus, for the fixed evaporator coupling fluid inlet temperature of 12.8°C, the higher refrigerant concentration employed in the steady-state model yields greater delivered cooling. Future models can be designed to incorporate the UA-value of the rectifier to model the transient heat transfer in the rectifier, and the concentration of the refrigerant outlet can be then estimated as a direct result of mass, species and energy balances.

Overall, the dynamic model represents the absorption chiller under consideration with reasonable accuracy. Thus, the validated dynamic model is used to further understand the transient behavior of the chiller in the following sections.

5.3 Transient response to a change in the desorber coupling fluid temperature

The dynamic response of the chiller to a step increase in the coupling fluid temperature at the desorber inlet is investigated. This type of situation can occur when the driving waste heat temperature is suddenly raised.

In this analysis, the original chiller model is evaluated for 550 s, when it reaches nearly steady-state behavior, and a 10 K step increase is applied to the inlet temperature of the desorber coupling fluid. The coupling fluid temperatures at the inlet of the absorber and evaporator are

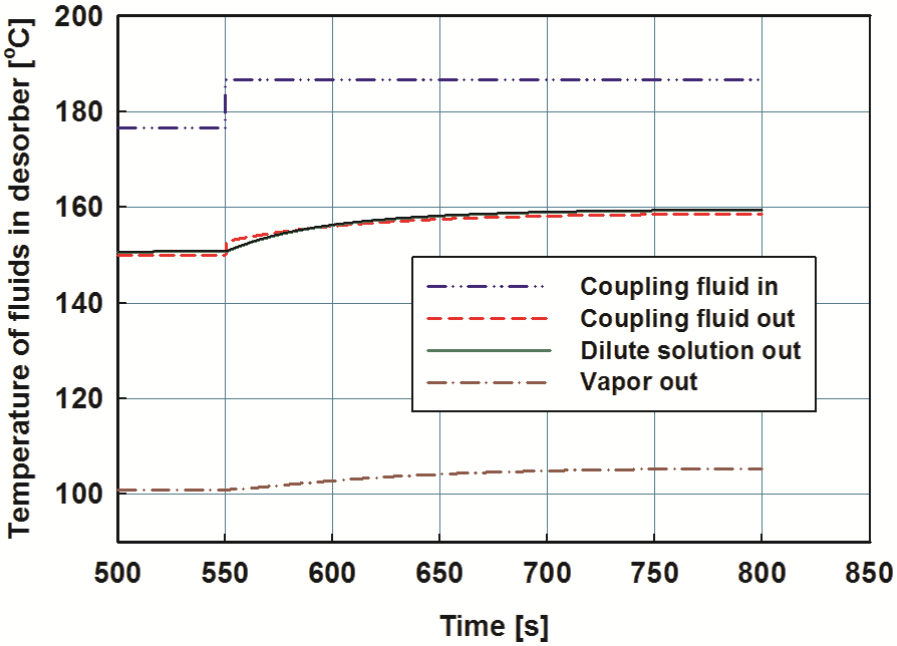

Figure 5.10 Temperature response of desorber to the simulated 10 K step increase in the desorber coupling fluid

unchanged. The simulation is continued until t = 800 s, when the system reaches a new, near steady-state condition.

5.3.1 Temperature response of desorber

The temperature responses of the desorber to the increased coupling fluid temperature are presented in Figure 5.10.

The desorber coupling fluid temperature at the inlet is stepped up by 10 K at t = 550 s. As a result, the coupling fluid outlet temperature increases by 8.6 K. The outlet temperature change lags behind the initial step change and requires approximately 200 s to reach a new steady state value.

The dilute solution exiting the bottom of the desorber is hotter than the vapor at the top due to heat supplied by the hot coupling fluid, which enters from the bottom of the desorber. It can be seen that a large increase in the liquid outlet temperature occurs (8.8 K), whereas a relatively smaller increase is seen in the vapor outlet temperature (4.4 K).

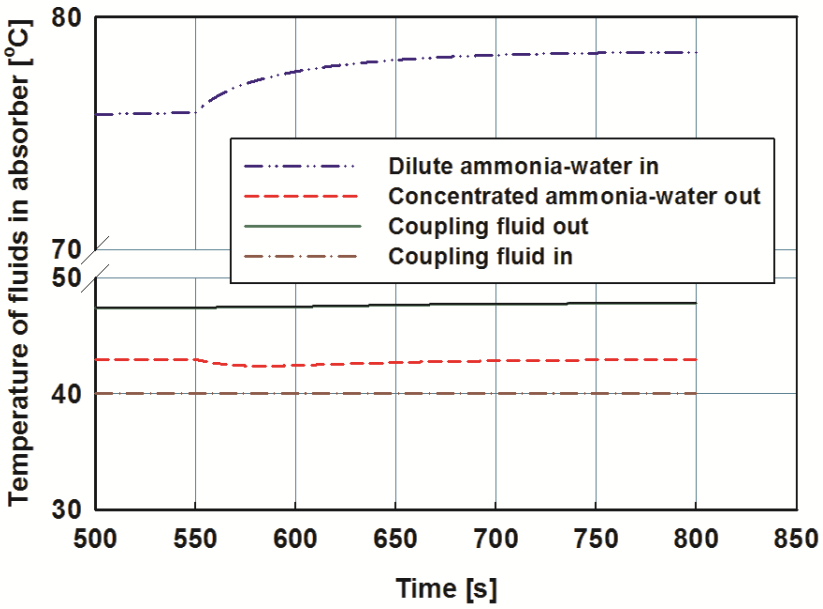

Figure 5.11 Temperature response of absorber to the simulated 10 K step increase in the desorber coupling fluid temperature

5.3.2 Temperature response of absorber

The temperature responses of the absorber to the increased coupling fluid temperature are presented in Figure 5.11. The coupling fluid temperature at the inlet of the absorber is maintained unchanged at the previous steady-state value of 40°C. The coupling fluid temperature at the outlet increases by 0.4 K due to the higher heat rejection in the absorber arising from the increased system heat input at the desorber.

The temperature of the dilute ammonia-water mixture at the absorber inlet increases by 2.6 K from t = 550 s to t = 800 s, whereas the concentrated solution outlet temperature decreases initially, but later increases in response to the increasing absorber inlet temperature. The initial drop in the absorber outlet temperature is due to higher heat rejection in the absorber around t = 550 s.

The gradual increase of fluid outlet temperature in the absorber can be attributed to the thermal inertia of the fluid in the absorber. The higher temperature of the returning dilute

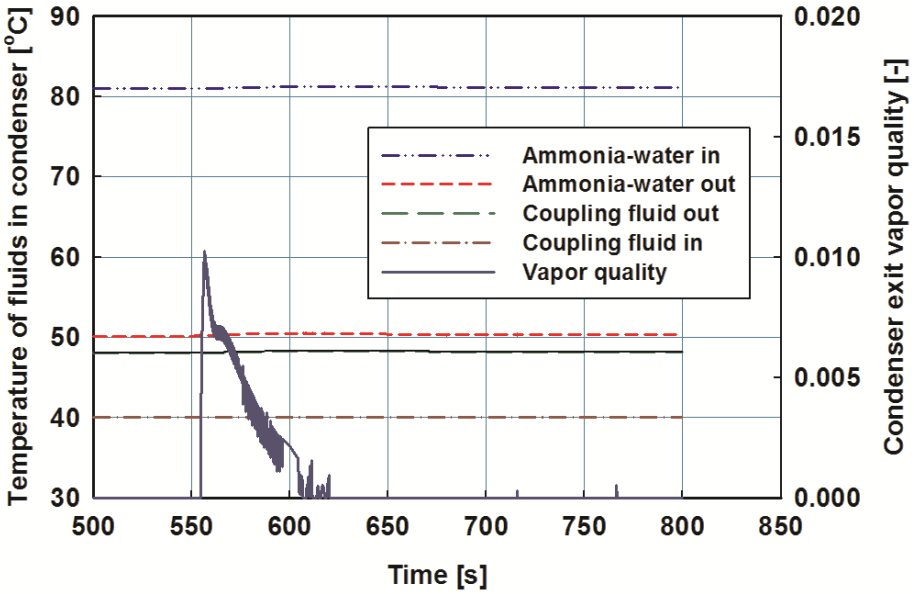

Figure 5.12 Temperature and exit quality response of condenser to the simulated 10 K step increase in the desorber coupling fluid temperature

solution from the desorber (Figure 5.10) results in higher enthalpy of the solution entering the absorber. The increased inlet temperature of the solution is a direct consequence of an increase in the enthalpy of the dilute solution entering the absorber.

5.3.3 Temperature and exit vapor quality response of condenser

Figure 5.12 shows the temperature and quality response of the condenser fluids to a step increase in the desorber coupling fluid temperature.

The coupling fluid temperature at the inlet of condenser is maintained at 40°C whereas the outlet temperature increases by 0.2 K, again due to the higher condenser duty from this higher desorber coupling fluid temperature input. The delay of ~ 8 s in the temperature response can be attributed to the thermal inertia of the condenser wall and coupling fluid.

The temperature of the ammonia-water mixture at the inlet and outlet of the condenser increase by 0.1 K from t = 550 s to t = 760 s. Increased heat transfer in the desorber raises the condenser refrigerant vapor flow rate and inlet temperature. . An increase in the outlet

temperature is observed near t = 550 s, which can be attributed to a peak in the exit vapor quality at the condenser. The condenser is unable to reject the higher heat duty due to the additional vapor generation at the desorber after the simulated change (t = 550 s to 600 s). As time progresses, the exit quality of the condenser decreases to zero due to sufficient cooling of the vapor in the condenser, resulting in a saturated liquid exit and a decrease in the ammonia-water temperature at the outlet. Also, the high-side pressure increases slightly, increasing the driving temperature difference for condenser heat rejection. The oscillations seen in the condenser exit vapor quality are due to numerical instabilities in the property estimation routines at low vapor qualities. They can be removed if simulations are run repeatedly, and the property estimations are saved for those low quality data points. However, the qualitative nature of the results would still be the same.

5.3.4 Temperature response of evaporator

Figure 5.13 shows the temperature response of the evaporator fluids. The coupling fluid temperature at the inlet is maintained at 12.77°C, while the outlet temperature decreases by 0.2 K from t = 550 s to t = 800s, due to a higher evaporator cooling capacity with the larger refrigerant flow rate. The oscillations in the outlet temperature can be attributed to a relatively low coupling fluid mass (0.02 kg) assumed in the evaporator, which causes large oscillations in temperature estimation.

The temperature of ammonia-water at the evaporator inlet decreases by 2.6 K from t = 550 s to t = 800 s, whereas its outlet temperature increases by 5.6 K. The inlet temperature decreases due to a 43 kPa reduction in the low-side pressure. The outlet temperature increases due to the larger evaporator glide (11 K) observed at lower pressures. There is an abrupt change in the nature of oscillations at t ~ 700 s, which could be attributed to the type of solver (ode45 –

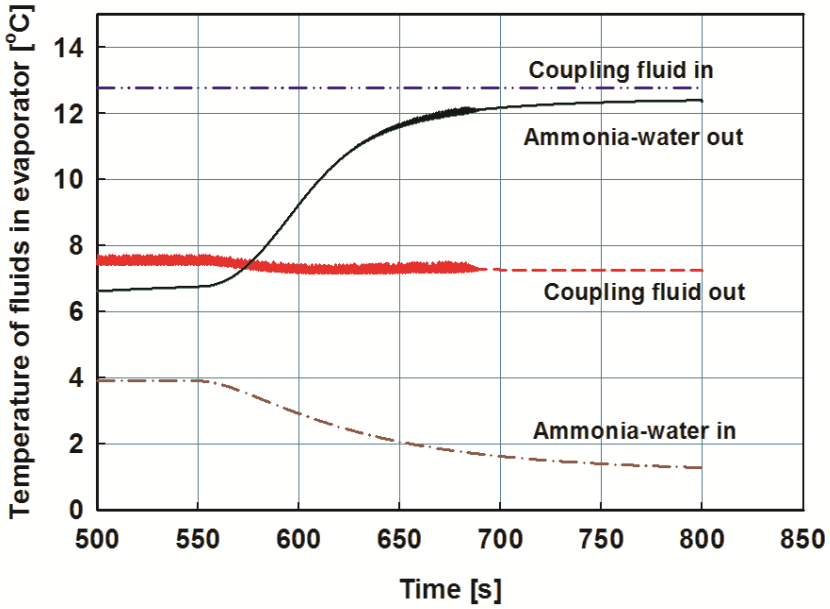

Figure 5.13 Temperature response of evaporator to the simulated 10 K step increase in the desorber coupling fluid temperature

explicit; for a non-stiff system) used in the model. In future simulations, an implicit solver such as ode15s that could handle a stiff system of equations can be used to address this issue.

5.3.5 Pressure response

The variations of the pressures and refrigerant flow rate in response to the simulated increase in the desorber coupling fluid temperature are presented in Figure 5.14.

The high-side pressure increases from 1,956 kPa to 1,967 kPa from t = 550 to 800 s. The increase in the high-side pressure can be attributed to the higher vapor generation inside the desorber, which allows more vapor to accumulate in the refrigerant tank, thus causing the build-up in the high-side pressure. This 11 kPa increase in the high-side pressure increases the condenser saturation temperature at the outlet by 0.16 K.

The low-side pressure decreases from 469 kPa to 426 kPa from t = 550 s to t = 800 s.The low-side pressure decreases after t = 550 s, but takes longer to reach a new steady-state value compared to the high-side pressure. The low-side pressure is set by the solution tank, which

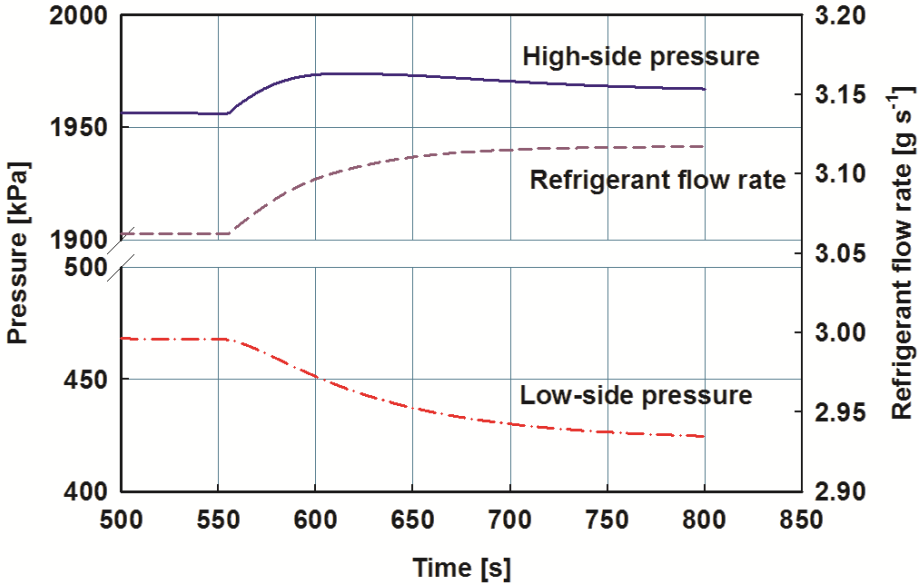

Figure 5.14 Pressure and refrigerant flow rate response to a simulated 10 K step increase in the desorber coupling fluid temperature

receives cooled solution from the absorber. The decrease in the low-side pressure can be attributed to a drop in the concentration of dilute solution entering the absorber inlet. Low inflow of ammonia into the solution tank downstream of absorber depletes the ammonia content in the tank, thus reducing the low-side pressure. The lower concentration of the solution entering the absorber results in a lower fraction of ammonia entering the solution tank, because the concentration of the refrigerant flowing through the condenser and expansion valve is nearly constant. As a result, the ammonia concentration inside the solution tank decreases, and reduces the low-side pressure.

The refrigerant flow rate across the valve increases from 3.062 g s^{-1} to 3.117 g s^{-1} from t = 550 s to t = 800 s. The increased flow rate is due to higher vapor generation in the desorber and an increased pressure difference across the valve. The rate of increase is gradual due to storage in the refrigerant tank. A short delay is observed just after t = 550 s, after which the flow rate starts

to increase. The high-side pressure also presents a similar delay during this period and subsequently starts to rise. The delay is also due to fluid accumulation in the refrigerant tank.

5.3.6 Flow rate response

Figure 5.15 shows the transient variation in the flow rates of the refrigerant, concentrated and dilute solutions, and refrigerant vapor at the desorber outlet in response to the simulated increase in the desorber coupling fluid temperature. The concentrated solution flow rate is maintained at 9.75 g s^{-1} by the solution pump and is unaffected by the simulated change in desorber coupling fluid temperature.

The refrigerant flow rate across the valve increases from 3.062 g s^{-1} to 3.117 g s^{-1} from t = 550 s to t = 800 s, as explained in the previous section. The refrigerant vapor flow rate exiting the desorber increases from 3.18 g s^{-1} to 3.28 g s^{-1} from t = 550 s to t = 800 s. This increase is a direct consequence of the higher heat duty in the desorber. The increase is gradual due to the

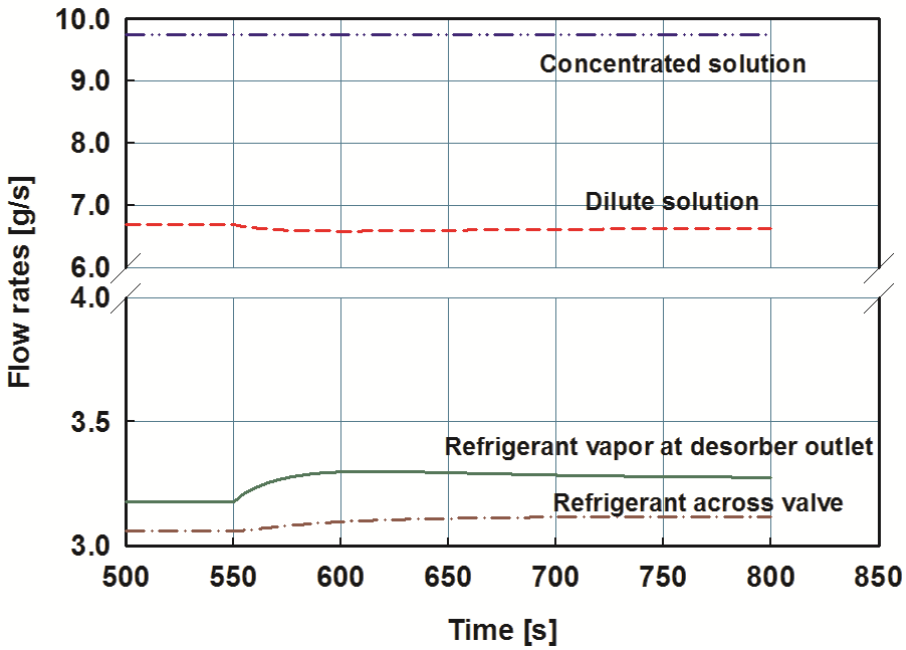

Figure 5.15 Flow rates response to 10 K step increase in the desorber coupling fluid temperature

thermal mass of the desorber wall. After the initial increase, the flow rate of vapor in the desorber decreases, and reaches steady state at t = 800 s, because the desorber vapor and liquid temperatures increase to reflect the coupling fluid temperature increase (Figure 5.10) and decrease the rate of vapor generation in the desorber.

The concentrated solution flow rate is maintained at 9.75 g s^{-1} by the solution pump and is unaffected by the simulated change in desorber coupling fluid temperature. However, the dilute solution flow rate decreases slightly from 6.68 g s^{-1} to 6.63 g s^{-1} from t = 550 s to t = 760 s. This is expected because a higher rate of ammonia vapor generation reduces the desorber solution outlet flow rate.

5.3.7 Concentration variation

Figure 5.16 summarizes the concentration response to a step increase in the desorber coupling fluid temperature. The ammonia concentration of the refrigerant is shown at the outlet of the refrigerant tank. It is unchanged by the simulated increase in the desorber coupling fluid

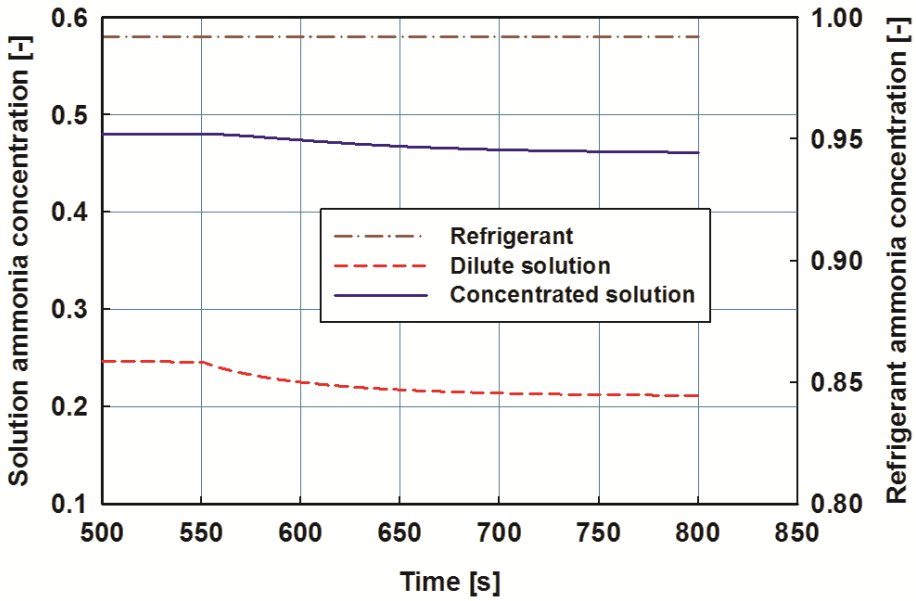

Figure 5.16 Concentration response to 10 K step increase in the desorber coupling fluid temperature

temperature. This is because the rectifier model assumes a fixed concentration of 0.992 to exit the rectifier at all times. Thus, any change in the concentration upstream of the rectifier does not influence the ammonia concentration of refrigerant exiting the valve (downstream of the rectifier).

The concentration of solution exiting the pump and the solution tank (concentrated solution in Figure 5.16) decreases gradually, from 0.481 to 0.462 from t = 550 s to t = 800 s, whereas the dilute solution concentration returning from the desorber undergoes a sharp decrease from 0.247 to 0.212 from t = 550 s and t = 800 s. Increased ammonia-vapor generation at the desorber decreases the concentration of the dilute solution. . The concentrated solution exiting the solution tank experiences a smooth variation despite the sharp transient at the inlet of tank (returning dilute solution), due to species and mass storage inside the tank. Thus, the concentrated solution exiting the tank has a relatively smaller decrease in ammonia concentration.

5.3.8 Heat transfer rate and COP variation

Figure 5.17 shows the evolution of heat transfer rates in the chiller in response to the step increase in the desorber coupling fluid temperature.

It can be seen from Figure 5.17 that the high-side component heat transfer rates (desorber and condenser) undergo sharp transients, whereas the low-side component heat transfer rates (evaporator and absorber) undergo slower transient changes. This behavior is expected after the step increase in the coupling fluid temperature at the high side of the chiller. It increases the heat transfer and the vapor generation in the desorber. Higher rates of vapor generation result in a larger refrigerant flow into the condenser, and a correspondingly higher heat duty needs to be rejected by the condenser. The desorber heat transfer rate decreases gradually to reach steady

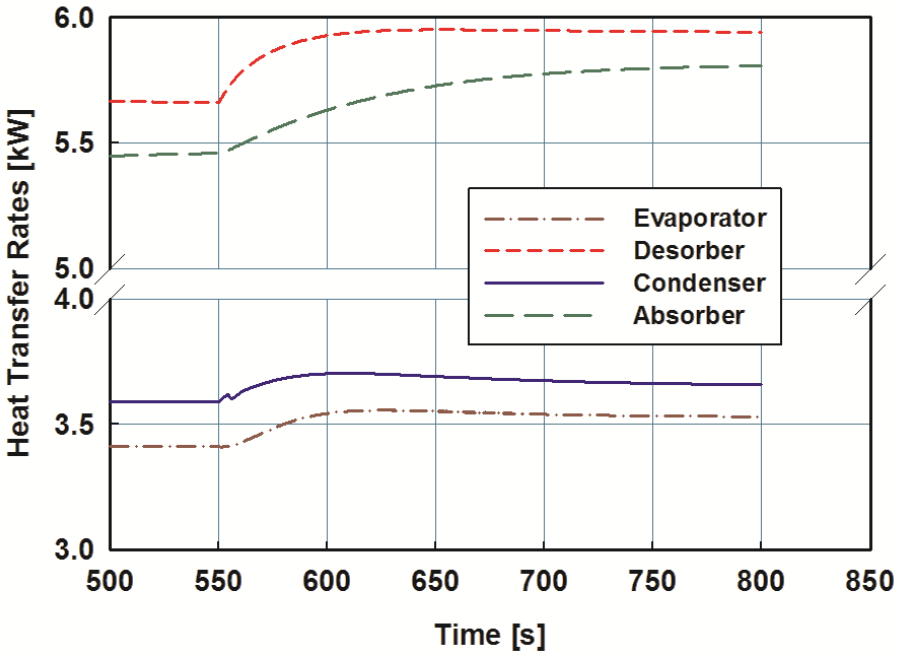

Figure 5.17 Heat transfer rate response to 10 K step increase in the desorber coupling fluid temperature

state after the initial increase. This is because the temperature of ammonia-water (dilute solution in Figure 5.10) at the outlet increases and thereby reduces the temperature difference between the coupling fluid and ammonia-water (Figure 5.10) and lowers the heat transfer rate in the desorber. The condenser duty also decreases after the initial increase due to a decrease in the vapor flow rate into the condenser after the initial increase (Figure 5.15). The kink observed in the condenser duty at t = 550 s could be attributed to the sharp increase in the condenser exit vapor quality and ammonia-water outlet temperature (Figure 5.12) at that instant. The increase in the absorber duty is due to increased flow of refrigerant into the absorber, which increases the heat rejection in the component.

The desorber heat transfer rate is observed to increase from 5.66 kW to 5.94 kW, whereas the increase in the evaporator heat transfer rate is from 3.41 kW to 3.53 kW. Similarly, increasing trends in the absorber and condenser heat loads are observed. The absorber heat duty

increases from 5.46 kW to 5.80 kW, while the condenser duty increases from 3.59 kW to 3.66 kW. Thus, the COP of the system decreases from 0.602 to 0.594, as shown in Figure 5.18.

From Figure 5.18, it can be seen that an increase in the evaporator cooling capacity due to an increase in the liquid refrigerant flow rate (Figure 5.15) occurs after a time delay (t ~ 555 s) due to refrigerant storage in the refrigerant tank. The increase in the cooling capacity is also because of a decrease in the low-side pressure and ammonia-water temperature at the inlet of the evaporator (Figure 5.13). The cooling capacity decreases later and reaches steady state because of an increased evaporator glide as the low-side pressure decreases, which reduces the heat transfer rate in the evaporator. An increase of 0.12 kW is observed in the cooling capacity from t = 550 s to t = 800 s. The time taken for the cooling capacity variation to settle to within less than 2% of this increase is 210 s. The COP decreases initially due to an increase in the desorber duty, and later increases to account for the increase in evaporator duty. As the evaporator duty

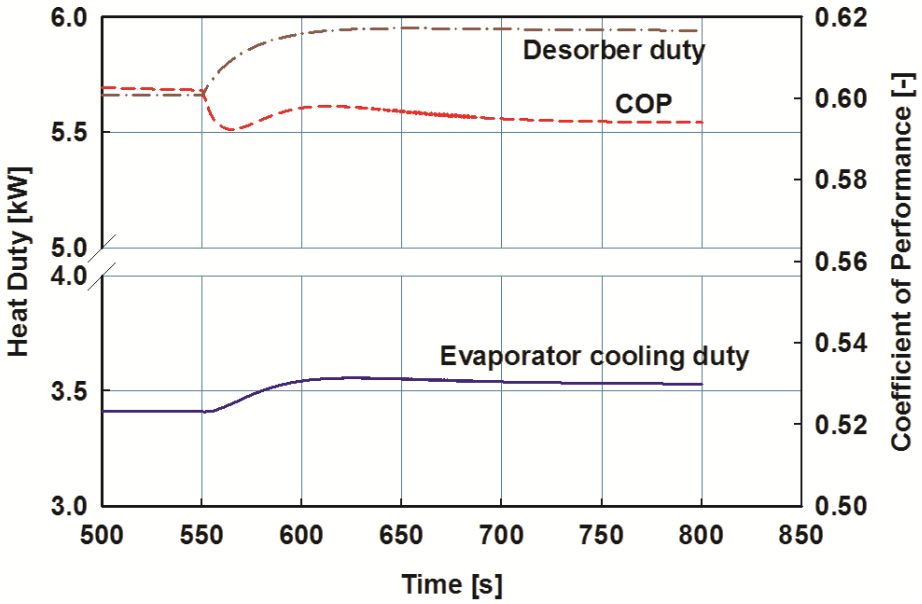

Figure 5.18 Evaporator cooling capacity, desorber heat input and COP response to 10 K step increase in the desorber coupling fluid temperature

decreases and reaches steady state, the COP follows the same trends.

It can be concluded that the step change of 10 K introduced in the desorber coupling fluid temperature leads to a 0.12 kW increase in the cooling capacity and slight reduction in the COP. Therefore, a step increase or decrease in the driving waste heat temperature can be used as an effective way to control the cooling duty and COP of the chiller during transient operation.

5.3.9 Conclusions

The analysis in this section details the absorption chiller response to a 10 K step increase in the desorber coupling fluid temperature. The variations of key system parameters such as temperature, pressure, flow rate, concentration and heat duties to a 10 K step increase in the desorber coupling fluid temperature were discussed in this section. An increase in the desorber coupling fluid temperature results in higher desorber heat duty, which leads to an increase in ammonia vapor generation. The heat duties of the other components are also found to increase in response to this simulated change. The high-side component heat duties (condenser and desorber) have a faster dynamic response compared to the low-side component heat loads (evaporator and absorber). The cooling capacity of the chiller increases from 3.41 kW to 3.53 kW, while the COP decreases from 0.602 to 0.594 from t = 550 s to t = 800 s. The time taken for the cooling capacity variation to settle to within 2% of the increase is 210 s. Therefore, waste heat temperature can be tuned to effectively to control the performance of the chiller. The temperature responses of the ammonia-water mixture and the coupling fluids of the respective components reflect an increase in the component heat duties. A sharp increase in the condenser exit quality confirms the increased rate of ammonia vapor generation in the desorber. The transient response of system pressures demonstrated high-side pressure build-up and a reduction in the low-side pressure. An increased pressure difference between the high- and low- sides

resulted in a higher refrigerant flow through the expansion valve. The transient response of the concentration revealed a decrease in the ammonia concentration of both the concentrated and dilute solutions, and an unchanged ammonia concentration of the refrigerant exiting the valve.

5.4 Transient response to increase in the desorber coupling fluid flow rate

The second scenario investigated is a step increase in the desorber coupling fluid flow rate. This can occur during two situations. First, the driving waste heat stream flow rate can vary on a given day, depending on the source. Second, depending on the type of coupling fluid pump control (i.e., variable or fixed speed pump), the flow rate of the heated coupling fluid can increase or decrease during operation.

The simulation is carried out over a duration that allows adequate time for the system parameters to attain near steady state, until t = 550 s. At t = 550 s, a 0.017 kg s^{-1} (20%) step increase in the desorber coupling fluid flow rate is introduced. All other parameters are maintained the same and simulation is conducted until t = 800 s, when the system parameters attain new steady state values. The focus of the following sections is to analyze the transient variation of the chiller parameters at times from t = 550 s to t = 800 s.

5.4.1 Pressure variation

Figure 5.19 summarizes the pressure variation in response to the simulated change in the desorber coupling fluid flow rate.

The high-side pressure is increased from 1956 kPa to 1959 kPa from t = 550 s to t = 800 s, while the low-side pressure decreases from 468 kPa to 457 kPa during this period. These changes are relatively lower than the pressure response to the 10 K step increase in the desorber coupling fluid temperature (10 kPa and 49 kPa for the high- and low-sides respectively). A

0.017 kg s^{-1} (20%) increase in the coupling fluid flow rate does not increase the rate of vapor generation enough to cause a substantial increase in the high-side pressure.

The increase in the high-side pressure is expected because a higher rate of ammonia-vapor generation in the desorber, which results in a greater vapor flow into the condenser. A 20 s delay is observed in the increase due to mass storage in the refrigerant tank. The condenser is unable to cool the vapor initially. This causes low quality mixture to enter the refrigerant tank, thereby raising the vapor pressure of the mixture inside the refrigerant tank.

The low-side pressure decreases due to the reduced ammonia flow into the absorber and solution tank. The 10 s delay is due to mass and species storage in the solution tank, which delays the decrease in ammonia concentration in the tank, thus causing a reduction in the low-side pressure. The net ammonia flow rate and concentration of the dilute solution returning to the absorber is reduced and is not sufficiently compensated for by the increased refrigerant flow rate from the evaporator into the absorber. Thus, the vapor pressure in the solution tank (also the low-

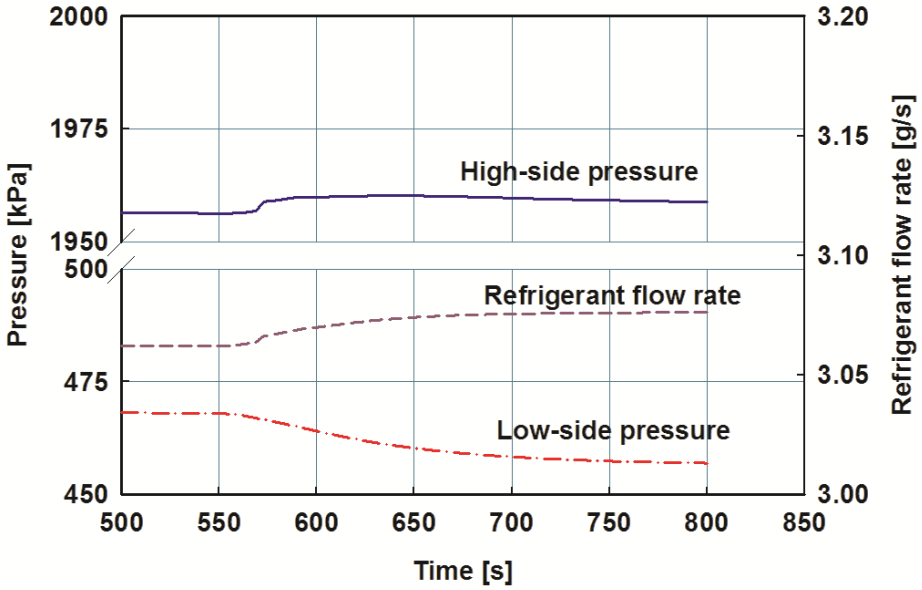

Figure 5.19 Pressure and liquid refrigerant flow rate response to 0.017 kg s^{-1} (20%) step increase in the desorber coupling fluid flow rate

side pressure) decreases.

The refrigerant flow rate across the valve is also shown in Figure 5.19. The increase in the high-side pressure occurs only at t = 570 s, although the increase in the desorber coupling fluid flow rate happens at t = 550 s. This delay is the reason for a 20 s delay in the increase in refrigerant flow rate. The refrigerant flow rate increases from 3.062 g s^{-1} to 3.076 g s^{-1} from t = 550 s to t = 800 s due to an increase in the pressure difference across the valve.

5.4.2 Flow rate variation

Figure 5.20 explains the variation of flow rates of solution and refrigerant in the chiller during the transient operation period from t = 550 s to t = 800 s.

The flow rate of the liquid refrigerant across the valve increases from 3.062 g s^{-1} to 3.076 g s^{-1} from t = 550 s to t = 800 s, as explained in the earlier section. The flow rate of the refrigerant vapor exiting the desorber is also shown in Figure 5.2. The flow rate of the vapor

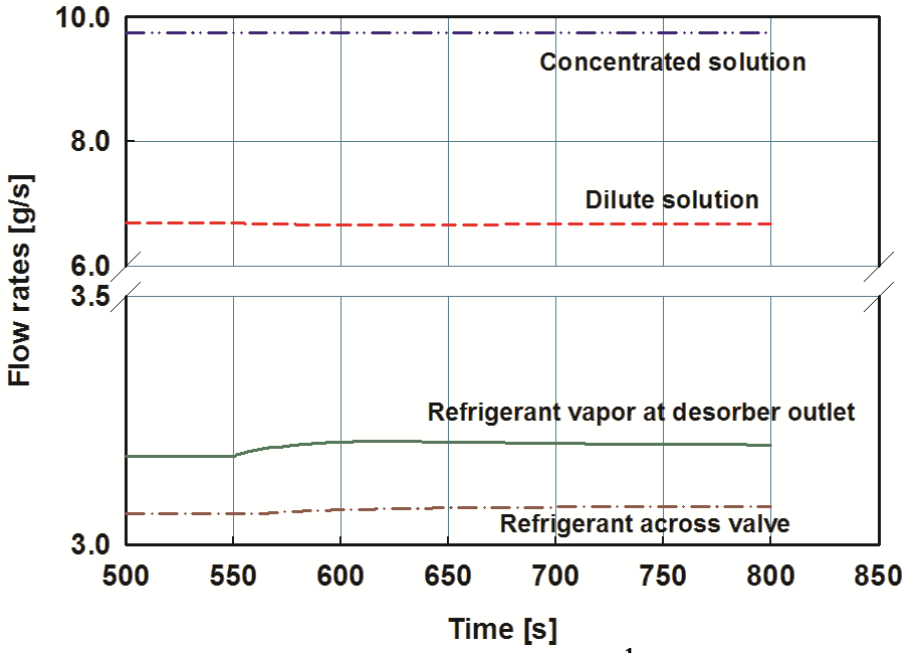

Figure 5.20 Flow rate response to 0.017 kg s^{-1} (20%) step increase in the desorber coupling fluid flow rate

increases from 3.18 g s^{-1} to 3.20 g s^{-1} from t = 550 s to t = 800 s. The increase in vapor flow rate is a direct consequence of an increase in the heat transfer rate of the desorber, and a resultant increase in vapor generation. The initial increase in the vapor flow rate is followed by a gradual decrease, because the high-side pressure increases to account for an increase in vapor generation, thereby raising the temperature of the vapor outlet (by 1 K), and decreasing the heat transfer rate in the desorber.

The dilute solution flow rate decreases from 6.69 g s^{-1} to 6.67 g s^{-1} during the period from t = 550 s to t = 800 s. The decrease is expected because there is additional ammonia vapor generation inside the desorber due to surplus heat supplied by the heated coupling fluid.

The concentrated solution flow rate remains unaffected because it is maintained constant by the solution pump.

5.4.3 Concentration variation

Figure 5.21 shows the transient variations in the concentrations of the solution and

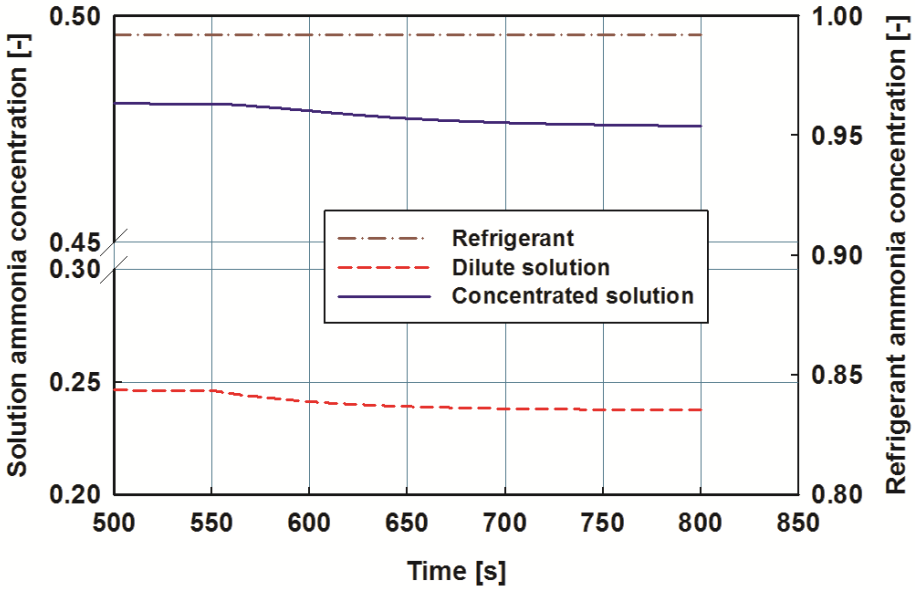

Figure 5.21 Concentration response to 0.017 kg s^{-1} (20%) step increase in the desorber coupling fluid flow rate

refrigerant circulated during chiller operation. The variation in concentration is shown from t = 550 s to t = 800 s.

The dilute solution concentration decreases from 0.2463 to 0.2377 from t = 550 s to t = 800 s as a result of an increase in desorber coupling fluid flow rate. . As expected, higher heat duty in the desorber results in a higher rate of ammonia vapor generation, thus reducing the ammonia content in the dilute solution returning from the desorber. This leads to the immediate response in the concentration of dilute solution close to t = 550 s.

The ammonia concentration in the concentrated solution is observed to decrease from 0.4806 to 0.4759 from t = 550 s to t = 800 s. But the decrease is observed gradually, and not instantly when the increase in coupling fluid flow rate is made at t = 550 s, due to storage of solution in the solution tank. The increase in desorber heat transfer rate decreases the concentration and flow rate of dilute solution returning to the absorber. The effect is then transmitted to the concentrated solution pumped out of the solution tank. Due to storage of solution inside the solution tank, a gradual decrease is observed.

The refrigerant concentration stays constant at 0.992 and is not affected by the simulated increase in the desorber coupling fluid flow rate, because the present model assumes constant refrigerant concentration at the rectifier outlet.

5.4.4 Heat transfer rates variation

Figure 5.22 shows the variation in heat transfer rates from t = 550 s to t = 800 s. In general, it can be seen that the heat transfer rates tend to increase after t = 550 s in response to the simulated step increase in the desorber coupling fluid flow rate. The increase in the heat transfer rates is expected, because a higher flow rate of the heated coupling fluid enhances the heat transfer in the desorber due to the increased heat transfer performance and mean

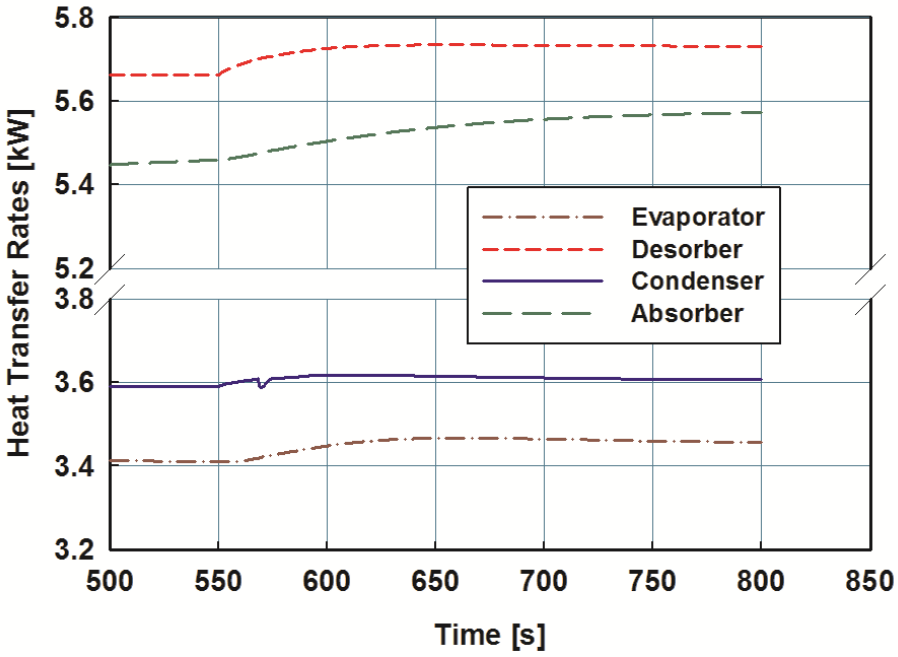

Figure 5.22 Heat transfer rate response to 0.017 kg s^{-1} (20%) step increase in the desorber coupling fluid flow rate

temperature difference. The increased heat transfer in turn increases the rate of ammonia vapor generation.

The evaporator heat transfer rate increases from 3.41 kW to 3.46 kW from t = 550 s to t = 800 s, whereas the desorber heat transfer rate rises from 5.66 kW to 5.73 kW during the same time period. The heat transfer rates of the condenser and absorber increase from 3.59 kW to 3.61 kW and 5.46 kW to 5.57 kW, respectively. The ammonia vapor also exits the desorber with an increased enthalpy and flows to the condenser, thereby increasing the required rate of heat rejection in the condenser. The local minima in the condenser duty at t ~ 570 s can be attributed to the increase in high-side pressure at that instant. The increase in the high-side pressure results in the temperature increase in the condenser (0.05 K). Also, the evaporator duty decreases after the initial increase due to the increased evaporator glide (a 3 K increase) for the ammonia-water at the lower low-side pressure.

A higher pressure in the high-side components results due to increased rate of heat transfer and vapor generation in the desorber. It increases the pressure difference between the high- and low- side components, thus forcing higher flow rate of refrigerant through the expansion valve. An increase in the refrigerant flow rate through the expansion valve increases the heat duty of the evaporator. Furthermore, the evaporator heat duty is enhanced by the decrease in refrigerant temperature at the inlet (decrease by 0.6 K) because of the lower low-side pressure (lower by 9 kPa). The dilute solution returns to the absorber from the desorber at a lower concentration due to an augmented rate of ammonia vapor generation. The higher refrigerant flow rate and the lower ammonia concentration of the incoming dilute solution contribute to a higher heat rejection requirement for the absorber. The condenser heat rejection capacity is not substantial enough to condense the entire vapor entering the component, just after the step increase in the desorber coupling fluid flow rate.

The time taken for heat duties to attain steady state value varies for each component. For instance, the desorber attains steady state the earliest, whereas the absorber and evaporator attain steady state relatively slowly. The reason for this behavior is that the simulated increase in flow rate directly improves the desorber heat transfer, but the effect is felt by other components gradually due to thermal inertia, and storage of solution and refrigerant during the transient operation. The simulated increase is transmitted to other components due to effects (higher rate of ammonia-vapor generation and higher pressure difference) described in the previous section.

Figure 5.23 shows the variation of coefficient of performance (COP) due to a simulated step increase in the desorber coupling fluid flow rate. The increase in the evaporator cooling capacity from 3.41 kW to 3.46 kW, and the desorber duty from 5.66 kW to 5.73 kW from t = 550

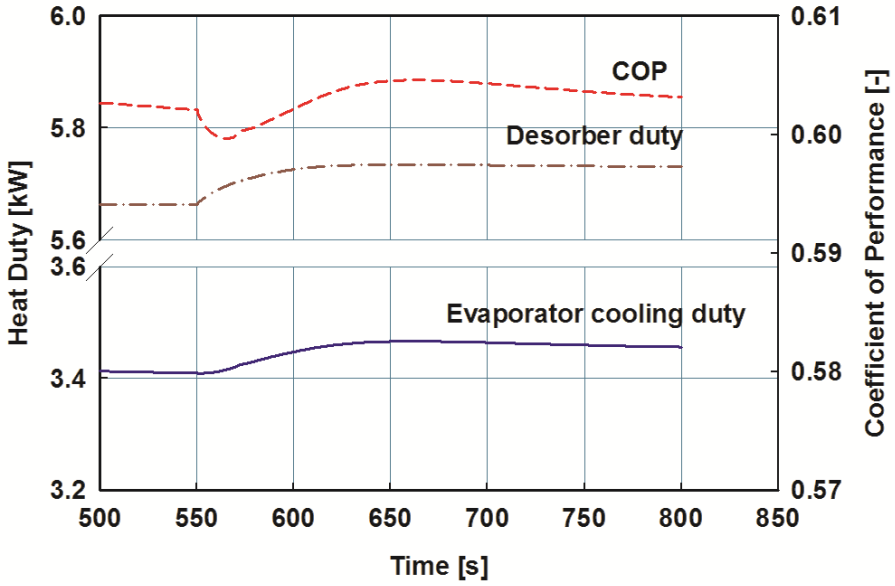

Figure 5.23 Cooling capacity, desorber heat input, and COP response to 0.017 kg s^{-1} (20%) step increase in the desorber coupling fluid flow rate

s to t = 800 s was explained in the previous section. The cooling capacity variation settled to within 2% of this increase in 190 s.

The COP of the chiller increases from 0.602 to 0.604 during the period from t = 550 s to t = 800 s. An initial decrease in the COP can be attributed to a faster increase of the desorber duty than the evaporator duty. As the evaporator duty increases, and the desorber duty reaches a steady value, the COP also increases and reaches its steady-state value of 0.604. After the initial decrease, the COP increases first and then decreases smoothly to reach its steady-state value. These trends can be attributed to similar variations in the evaporator cooling capacity, because the desorber duty reaches its steady-state value quickly, while the evaporator duty increases gradually, and later decreases to reach its steady-state value.Thus, an increase in the coupling fluid flow rate (20%) results in a slight increase in the COP of the chiller, while an increase in the evaporator cooling duty of 0.05 kW is achieved.

5.4.5 Conclusions

The desorber coupling fluid flow rate is increased by 0.017 kg s^{-1} (20%) at t = 550 s when the chiller output parameters have attained steady state values. The overall effect is an increase in vapor generation in the desorber and an increase in the refrigerant flow rate across the valve from 3.062 kg s^{-1} to 3.076 kg s^{-1} from t = 550 s to t = 800 s. The component heat duties increase in response to the simulated change. The desorber and condenser heat duties rise the fastest whereas the absorber and evaporator heat duties increase slowly because of storage of refrigerant and solution in the storage tanks. A 0.05 kW increase in the evaporator cooling duty is observed because of the step change. The time taken for the cooling duty variation to settle to within 2% of this increase is 190 s. The increase in the evaporator cooling duty is slightly larger than the increase in the desorber heat duty, and is reflected in the increased COP of the chiller from 0.602 to 0.604. The cooling capacity of the evaporator increases from 3.41 kW to 3.46 kW from t = 550 s to t = 800 s. The high-side pressure increases and low-side pressure decreases in response to the simulated change. A higher pressure difference across the valve is a direct consequence of the increased refrigerant flow from the desorber to the refrigerant tank via the condenser. The concentration response showed that the refrigerant concentration at the outlet of the refrigerant tank remains unaffected by the simulated change, whereas the dilute and concentrated solution concentrations decrease during the observed time period.

5.5 Transient response to step increase in the solution pumping rate

A third scenario is a step increase in the solution pumping rate. This can take place in two different cases. First, depending on the type of pump control (variable speed pump) used, the flow rate of the solution (set by the pump) can increase or decrease during operation. Second, the

load on the pump motor can vary depending on the pressure difference existing in the solution loop.

As before, the dynamic model is run until t = 550 s, allowing the system parameters to attain near steady state values. At t = 550 s, a 2 g s^{-1} (20%) step increase is introduced to the pumping rate of the solution. Other parameters are maintained the same and the model simulation continues until t = 780 s to study the dynamic behavior of the absorption system. This simulated change is a step increase in an internal system parameter without any change in the external parameters such as the coupling fluid temperatures or flow rates. The focus of the following sections is to analyze the variation of system parameters from t = 550 s to t = 780 s.

5.5.1 Pressure and refrigerant flow rate variation

Figure 5.24 summarizes the pressure variations at the high- and low- sides and refrigerant flow rate across the valve in response to the increased pumping rate during chiller operation.

The high-side pressure increases from 1957 kPa to 1964 kPa during the transient period from t = 550 s to t = 780 s. The rate of increase is steep just after t = 550 s, due to the increased pumping rate and higher rate of refrigerant vapor generation in the desorber. Increased vapor generation in the desorber results in higher refrigerant flow into the condenser and the refrigerant tank, raising the high-side pressure. The initial increase is followed by a decrease in the high-side pressure because the additional refrigerant vapor generated is cooled in the condenser and the condenser exit quality decreases to zero, after the initial peak just after t = 550 s, as shown in Figure 5.24.The low-side pressure is set by the solution tank. A higher pumping rate causes more solution to be drawn out of the solution tank near t = 550 s. The increase in the refrigerant flow rate (Figure 5.24) is gradual whereas the pumping rate increases instantaneously. Thus, the ammonia content in the solution tank decreases sharply just after t = 550 s, lowering the low-side

pressure. It reduces the vapor pressure of the mixture inside the tank, which decreases the low-side pressure.

The low-side pressure decreases from 469 kPa to 434 kPa from t = 550 s to t = 780 s. There is a delay of ~ 1 s between the instants when the low-side pressure encounters a sharp

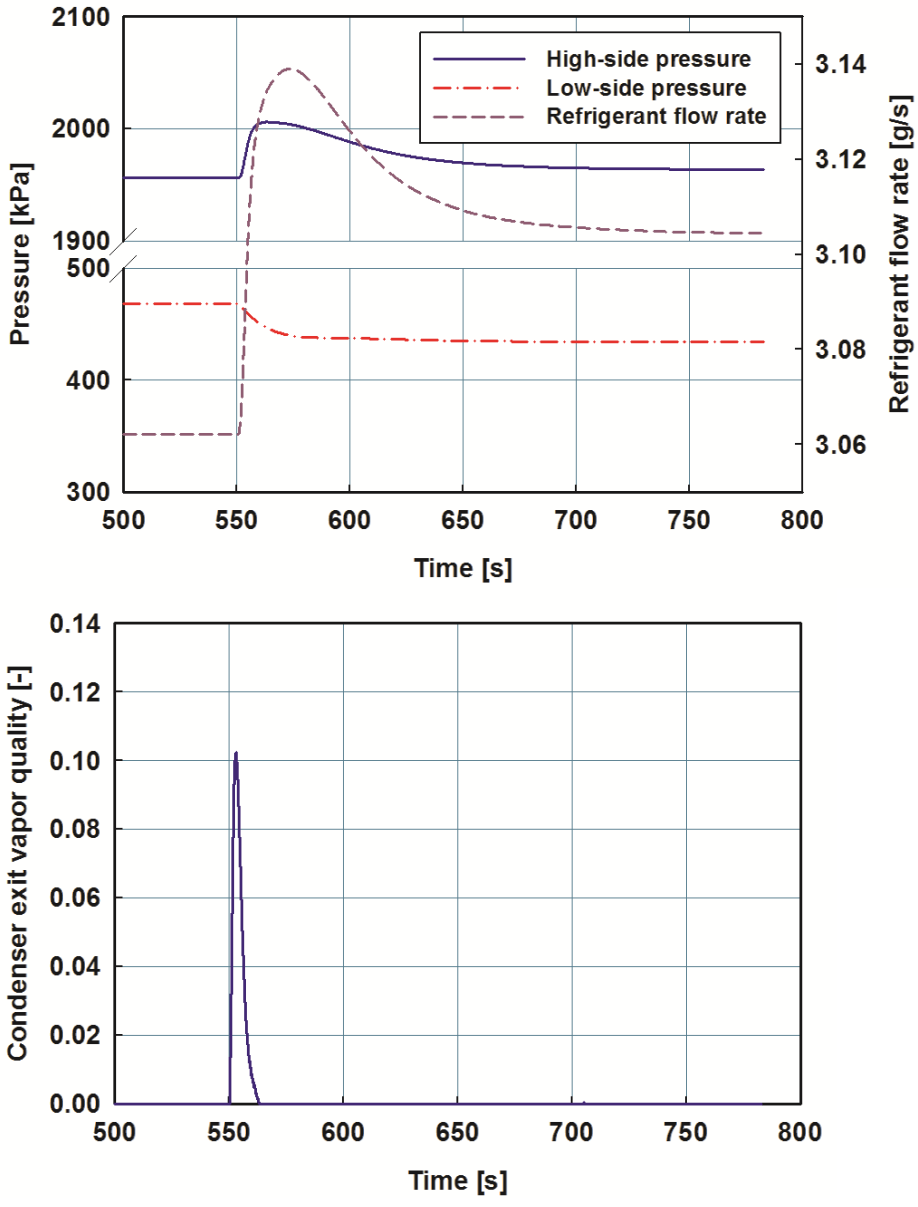

Figure 5.24 Pressure and refrigerant flow rate responses to 2 g s^{-1} (20%) step increase in the solution pumping rate

decrease and, the high-side pressure starts to increase. This delay is expected because the increased pumping rate directly affects the low-side pressure. It takes time for the desorber to vaporize the excess incoming solution. In addition, the delay can be attributed to mass and species storage in the refrigerant tank.

The refrigerant flow rate across the valve is also shown in Figure 5.24. The refrigerant flow rate increases from 3.062 g s^{-1} to 3.105 g s^{-1} from t = 550 s to t = 780 s. The increase in refrigerant flow rate is a direct result of an increase in the pressure difference across the valve. The flow rate increases almost instantaneously after the increase in the solution pumping rate due to a decrease in the low-side pressure. The flow rate follows the trends observed in the high-side pressure. It increases initially and later decreases smoothly to reach its steady-state value.

5.5.2 Flow rate variation

Figure 5.25 illustrates the flow rates variation in response to the step increase in the pumping rate of solution. The flow rate of the concentrated solution is increased from 9.75 g s^{-1}

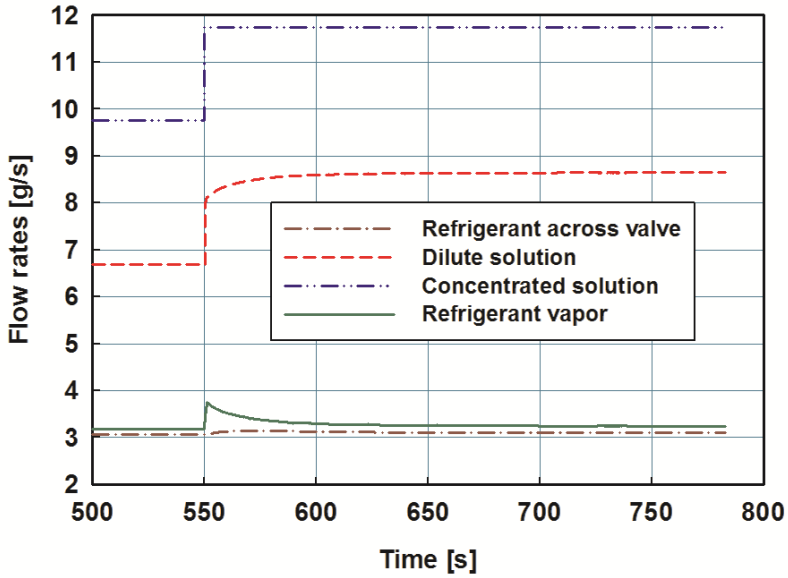

Figure 5.25 Flow rate response to 2 g s^{-1} (20%) step increase in the solution pumping rate

to 11.75 g s^{-1} (20%) at t = 550 s.

The dilute solution flow rate increases from 6.69 g s^{-1} to 8.65 g s^{-1} during the time period from t = 550 s to t = 780 s. The dilute solution flow rate is increased because of the increased pumping rate. A higher solution inflow to the desorber produces an increased rate of returning dilute solution almost instantly at t = 550 s, because the present model neglects any storage of solution in the desorber. Thus, a 2 g s^{-1} increase in the pumping rate produces a 1.96 g s^{-1} increase in the returning dilute solution flow rate.

The flow rate of the refrigerant across the expansion valve increases from 3.062 g s^{-1} to 3.105 g s^{-1} from t = 550 s to t = 780 s as explained in the earlier section. The refrigerant flow rate increases from 3.095 g s^{-1} to 3.119 g s^{-1}. The flow rate of refrigerant vapor exiting the desorber is also shown in Figure 5.25. The refrigerant vapor flow rate increases from 3.18 g s^{-1} to 3.24 g s^{-1} from t = 550 s to t = 780 s. The vapor flow rate increases sharply at t = 550 s due to the increase in the pumping rate. The vapor flow rate decreases after this initial increase due to the increase in the high-side pressure, which raises the solution temperature, and thereby, decreases the heat transfer rate in the desorber.

5.5.3 Concentration variation

Figure 5.26 depicts the variation in the concentrations of the concentrated and dilute solutions and the refrigerant in response to the increased pumping rate from t = 550 s to t = 780 s. The concentration of the concentrated solution decreases from 0.4807 to 0.4597 from t = 550 s to t = 780 s. The decrease in the ammonia content of the solution tank is a direct consequence of an increased pumping rate, which drains ammonia out of the tank. The dilute solution concentration increases from 0.2463 to 0.2685 from t = 550 s to t = 780 s. The concentration of the dilute solution returning from the desorber toward the low-side components is shown in

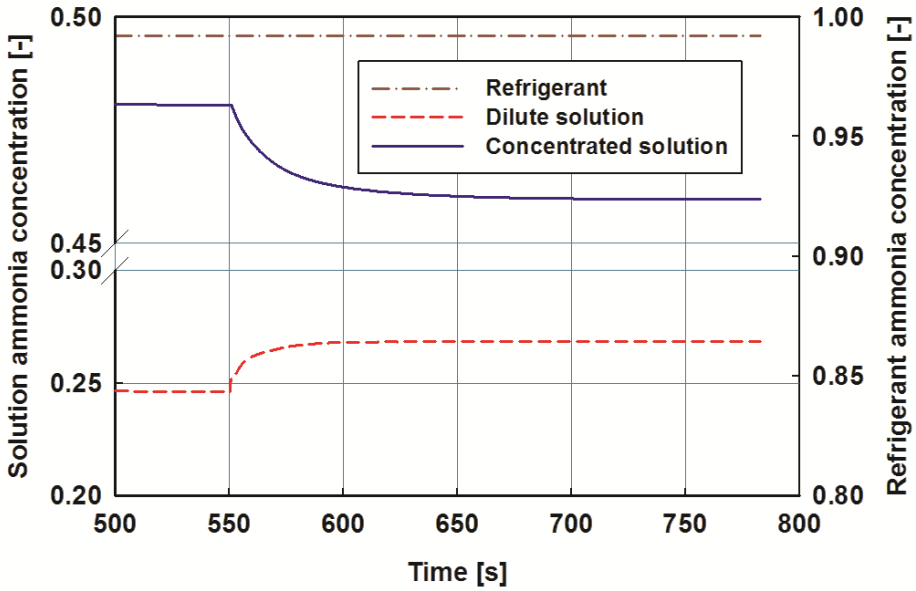

Figure 5.26 Concentration responses to 2 g s^{-1} (20%) step increase in the solution pumping rate

Figure 5.26. An increased flow rate of the concentrated solution (9.75 g s^{-1} to 11.75 g s^{-1}) offsets the decrease in the concentrated solution concentration (0.4807 to 0.4597), thus resulting in a net higher rate of ammonia flow out of the refrigerant tank into the desorber. The larger ammonia inflow into the desorber (concentrated solution) results in higher concentrations of the ammonia vapor generated in the desorber and the returning dilute solution.

The concentration of the liquid refrigerant exiting the tank is shown in Figure 5.26. The model assumes a constant concentration of refrigerant downstream of the rectifier flowing into the refrigerant tank. Thus, the refrigerant concentration remains unaffected by the sharp increase in the solution pumping rate.

5.5.4 Heat transfer rate and COP variation

Figure 5.27 represents the variation of heat transfer rates in response to the simulated increase in the pumping rate. The general trend seen is that the heat transfer rates increase with an increase in solution flow rate.

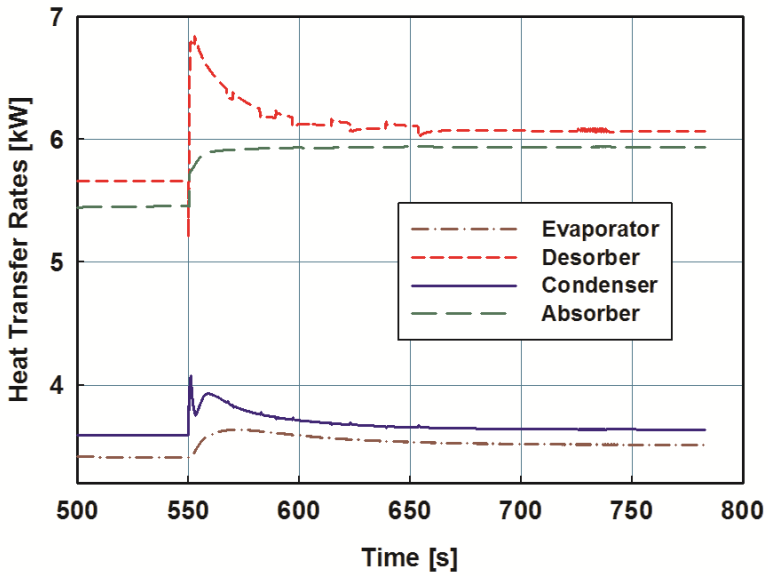

Figure 5.27 Heat transfer rate response to 2 g s^{-1} (20%) step increase in the solution pumping rate

The desorber heat transfer rate increases from 5.66 kW to 6.07 kW from t = 550 s to t = 780 s. The increased pumping rate therefore increases the desorber heat demand. A sharp peak is observed in the desorber heat transfer rate, in response to the step increase in the incoming solution flow rate. The sharp initial decrease in the desorber duty at t = 550 s can be attributed to the time it takes for the increase in solution flow to increase the enthalpy of dilute solution exiting the desorber at the other side. The desorber heat transfer rate rises more quickly than other component heat transfer rates, and later decreases gradually because the high-side pressure and thereby the desorber temperature increase to resolve the higher heat demand in the desorber. The oscillations in the desorber duty from t = 560 s to t = 650 s can be attributed to oscillations caused by the step change in the pumping rate on the desorber solver and its related ammonia-water property estimations. These oscillations can be decreased if a smooth ramp is introduced instead of a step change in the pumping rate.

The condenser heat transfer rate increases from 3.59 kW to 3.64 kW from t = 550 s to t = 780 s. The increase in the condenser heat duty is expected due to the larger refrigerant vapor

flow rate into the condenser. A sharp peak is observed in the condenser heat duty near t = 550 s as a result of the sudden increase in the pumping rate. A second peak in the condenser heat duty is observed due to a local maximum in the high-side pressure at that instant. A higher condenser pressure (high-side pressure) raises the enthalpy and temperature of the incoming vapor, and results in higher heat rejection requirements. As the exit vapor quality decreases to zero, the condenser duty decreases smoothly to reach its steady-state value.

The absorber heat duty increases from 5.45 kW to 5.94 kW during the time period from t = 550 s to t = 780 s. The increase in the absorber heat duty is a direct consequence of the increased flow rates of the returning dilute solution and circulated refrigerant at the inlet of the absorber. A reduction in the low-side pressure lowers the enthalpy of the incoming mixture. However, the increase in the flow rate of refrigerant-absorbent mixture at the absorber inlet raises the enthalpy of the mixture (i.e, refrigerant and absorbent mixture) significantly, and thus increases the heat duty of the absorber.

The evaporator heat duty increases from 3.41 to 3.51 kW in response to the increase in the pumping rate, from t = 550 s to t = 800 s. The rise in the evaporator heat duty is a direct consequence of a higher refrigerant flow into the evaporator from the refrigerant tank. A higher pressure difference across the valve causes more amount of refrigerant to be drawn from the refrigerant tank, and thereby increases the evaporator duty. The cooling capacity is decreased after the initial increase because the refrigerant flow rate across the valve also decreases with a decrease in the pressure difference, as shown earlier in Figure 5.24. A 0.1 kW increase is observed in the evaporator duty from t = 550 s to t = 780 s. The time taken for the evaporator duty variation to settle to within 2% of this increase is 176 s.

Figure 5.28 illustrates the variation of evaporator cooling capacity and coefficient of performance from t = 550 s to t = 780 s, in response to the simulated increase in the pumping rate. The evaporator cooling duty increases from 3.41 kW to 3.51 kW from t = 550 s to t = 780 s, while the desorber duty increases from 5.66 kW to 6.07 kW during the same period, as explained earlier. The COP of the chiller decreases from 0.602 to 0.579 during the period from t = 550 s to t = 780 s. The decrease in the COP is expected because the increase in the desorber heat demand (5.66 kW to 6.07 kW) more than offsets the improvement in the evaporator cooling duty (3.41 kW to 3.51 kW). The COP experiences a sharp decrease just after t = 550 s. As can be seen in Figure 5.27, the dynamics of the desorber heat transfer rate are faster than those of the evaporator heat transfer rate. The initial rise in the COP can be attributed to the sharp decrease followed by an increase in the desorber duty at t = 550 s. The oscillations seen in the COP can be attributed to similar oscillations in the desorber heat transfer rate. The initial rise in the COP can be attributed to the sharp decrease followed by an increase in the desorber duty at t = 550 s. The oscillations

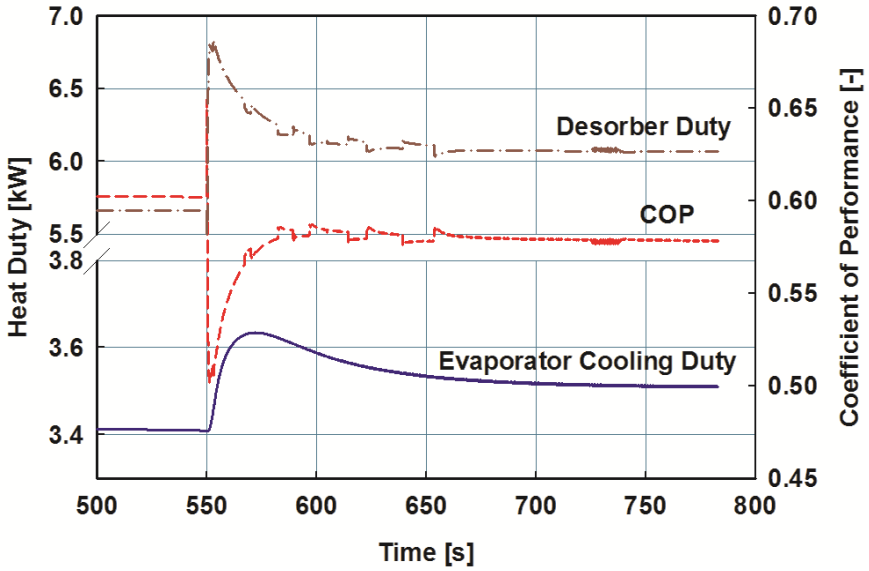

Figure 5.28 Cooling capacity, desorber heat input and COP responses to 2 g s^{-1} (20%) step increase in the solution pumping rate

seen in the COP can be attributed to similar oscillations in the desorber heat transfer rate.

5.5.5 Conclusions

The pumping rate is increased from 9.75 g s^{-1} to 11.75 g s^{-1} (20%) at t = 550 s when the chiller parameters have attained near steady state values. A higher pumped solution flow rate increases the refrigerant and dilute solution flow rates and concentrations. However, it depletes ammonia from the solution tank, which is reflected in the reduced concentration of concentrated solution exiting the solution tank. The heat transfer rates show an increasing trend in response to the higher solution pumping rate. The desorber and condenser heat duties rise sharply after t = 550 s, whereas the absorber and evaporator heat duties increase gradually. The increase in the evaporator heat duty from 3.41 to 3.51 kW is slightly lower than the increase in the desorber heat duty (5.66 kW to 6.07 kW). Therefore, the COP of the chiller is found to decrease from 0.602 to 0.579. Thus, increasing the solution pumping rate increases the evaporator cooling duty, but lowers the COP of the chiller. The cooling capacity variation settles to within 2% of this increase in 176 s. The high-side pressure increases and the low-side pressure decreases in response to the higher pumping rate. A higher pressure difference is observed across the valve and as a result, more refrigerant is drawn from the refrigerant tank.

5.6 Chiller response to partial closing of the refrigerant valve

The dynamics of the chiller are analyzed in this section by simulating the transient response of the chiller to a partial closing of the refrigerant valve. This scenario could occur during part load operation or with a sophisticated system controller that dynamically adjusts the valve setting.

As in the previous section, the original simulation is conducted for 550 s, allowing the system parameters to attain near steady state values. At t = 550 s, a 40% ($\Delta C_{valve} = 1 \times 10^{-6}$ kg s^{-1}

$Pa^{-0.5}$) step decrease is applied to the valve coefficient, as shown in Figure 5.29, to partially close the valve and step down the refrigerant flow rate. Other chiller parameters are maintained the same and the model is simulated until t = 800 s, when most output parameters are found to attain near steady state values.

5.6.1 Pressure variation

Figure 5.30 shows the pressure and refrigerant flow rate variations in response to the partial closing of the refrigerant valve.

The high-side pressure decreases from 1957 kPa to 1769 kPa from t = 550 s to t = 800 s. Partial closing of the valve reduces the refrigerant flow rate. It increases the amount of liquid-phase refrigerant retained inside the tank, thus lowering the vapor pressure of the mixture inside the tank.

The low-side pressure decreases from 469 kPa to 229 kPa from t = 550 s to t = 800 s. Partial closing of the refrigerant valve leads to reduced refrigerant flow into the absorber. This

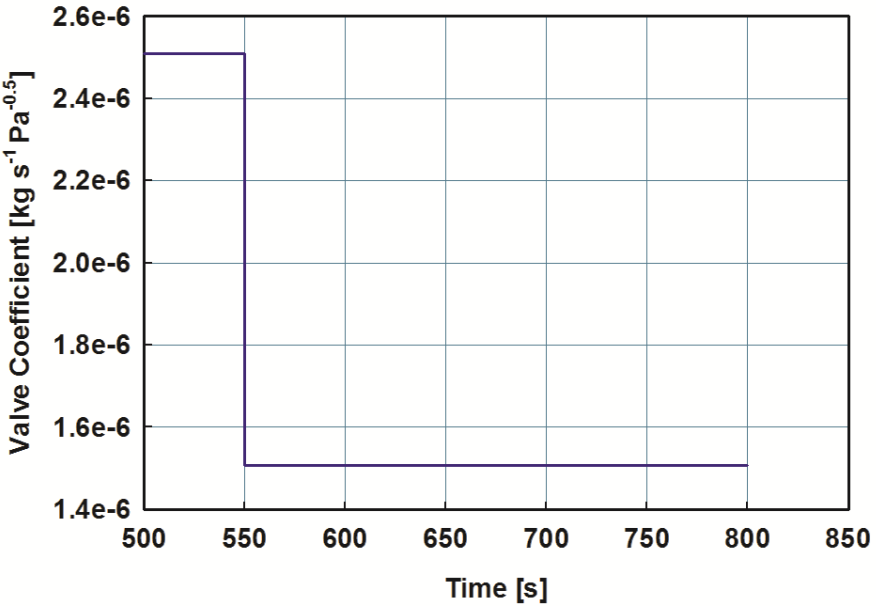

Figure 5.29 Valve coefficient showing partial closing (40%) of the valve

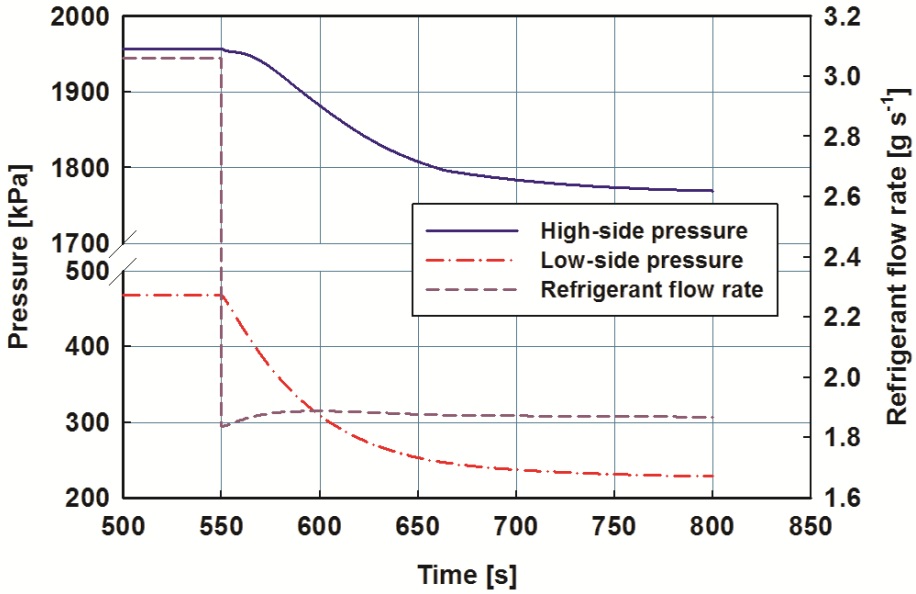

Figure 5.30 Pressure and refrigerant responses to 40% closing of the refrigerant valve

results in reduced flow rate and overall concentration of the solution entering the solution tank downstream of the absorber. However, the concentrated solution is pumped out of the solution tank at a constant rate, which depletes the solution tank of ammonia content, thus causing a reduction in the low-side pressure.

The refrigerant flow rate across the valve is also represented in Figure 5.30. The refrigerant flow rate decreases from 3.06 g s^{-1} to 1.87 g s^{-1} from t = 550 s to t = 800 s. A slight increase in the flow rate from t = 560 s to t = 600 s can be attributed to a temporarily higher pressure difference (ΔP = 1573 kPa) as compared to the pressure difference at t = 560 s (ΔP = 1526 kPa). From t = 600 s to t = 800 s, this pressure difference decreases gradually to 1542 kPa, thus reducing the refrigerant flow rate.

5.6.2 Flow rate variation

Figure 5.31 represents the flow rate variations from t = 550 s to t = 800 s in response to the simulated partial closing of the valve. The refrigerant flow rate undergoes an instantaneous

reduction at t = 550 s, from 3.06 g s^{-1} to 1.84 g s^{-1} and later increases to 1.87 g s^{-1} at t = 800 s, as explained in the previous section.

The flow rate of the dilute solution increases smoothly from 6.69 g s^{-1} to 7.87 g s^{-1}, while the refrigerant vapor flow rate at the desorber exit decreases from 3.18 g s^{-1} to 2.05 g s^{-1} from t = 550 s to t = 800 s, following the partial closing of the valve. The flow rates of the returning dilute solution from the desorber and generated refrigerant vapor are shown in Figure 5.31, and no sharp transients are observed. The returning dilute solution and refrigerant vapor flow rates are governed by the heat and mass transfer rates in the desorber. As stated earlier, the reduced refrigerant flow rate across the valve does not directly influence the heat and mass transfer in the desorber. However, the desorber heat transfer is lower due to the reduced ammonia flow into the desorber. The decrease in the refrigerant flow rate reduces the ammonia inflow into the solution tank downstream of absorber, and thereby decreases the concentration of solution pumped to the

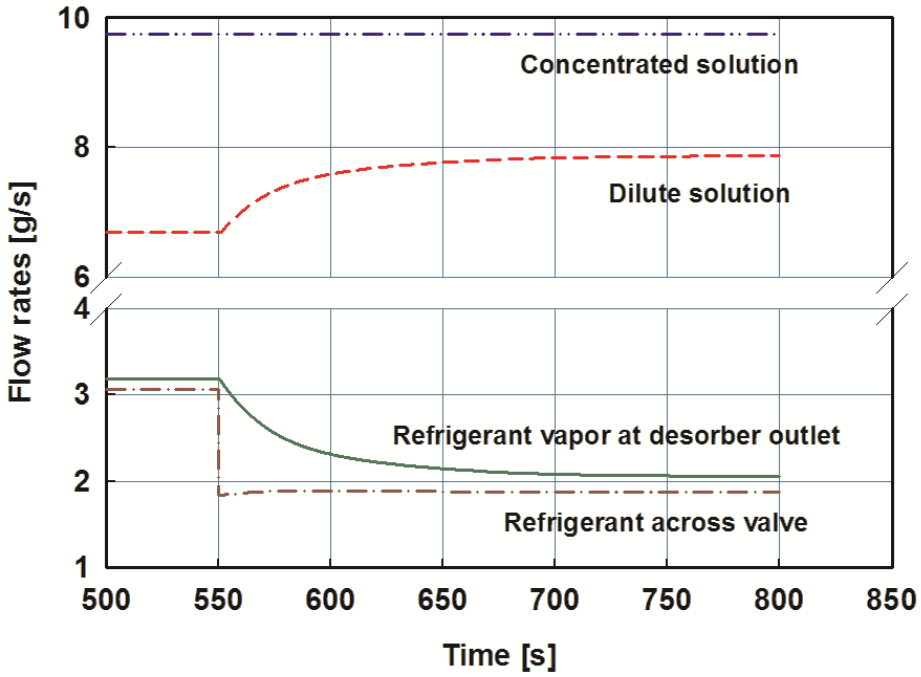

Figure 5.31 Flow rate response to 40% closing of the refrigerant valve

desorber. These factors decrease the heat transfer rate and refrigerant vapor generation in the desorber, and as a result of mass balance in the desorber, the dilute solution flow rate exiting the desorber is increased from 6.69 g s^{-1} to 7.87 g s^{-1} from t = 550 s to t = 800 s.

The pumping rate of the concentrated solution is fixed at 9.75 g s^{-1}. Thus, partial closing of the valve does not affect the flow rate of the concentrated solution.

5.6.3 Concentration variation

Figure 5.32 shows the concentration variation of refrigerant, concentrated and dilute solution in the cycle during the period from t = 550 s to t = 800 s in response to the partial closing of the valve.

The dilute solution returning from the desorber experiences a gradual reduction in ammonia concentration from 0.246 to 0.210 from t = 550 s to t = 800 s. The concentrated solution leaving the solution tank and entering the desorber is poorer in ammonia during the period from t = 550 s to t = 800 s. The concentrated solution concentration decreases from 0.481

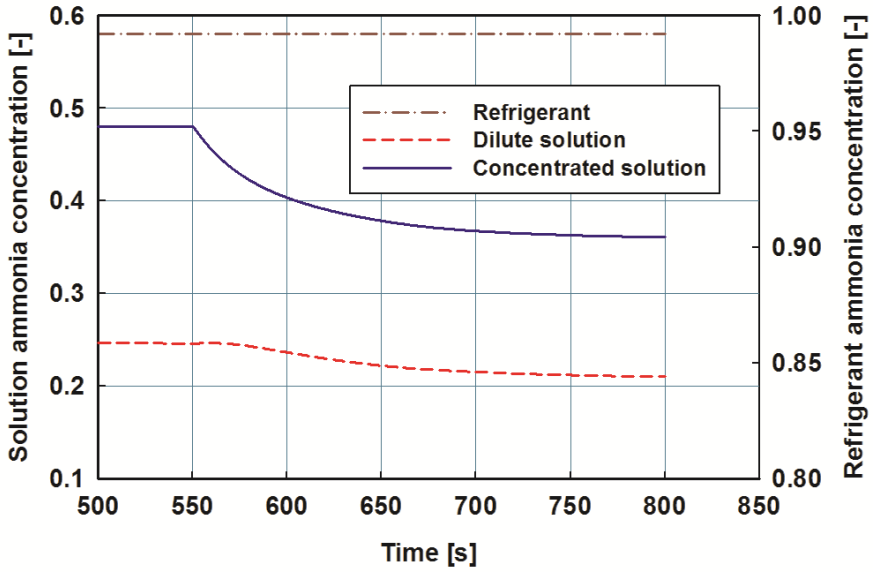

Figure 5.32 Concentration responses to 40% closing of the refrigerant valve

to 0.361 from t = 550 s to t = 800 s. The decrease in the concentrated solution concentration is a direct consequence of a step reduction in the refrigerant flow rate, which results in lower ammonia inflow into the solution tank. As a result, the ammonia fraction in the returning dilute solution gradually decreases, and is reflected in the dilute solution concentration in Figure 5.32.

The concentration of the refrigerant exiting the refrigerant tank is shown in Figure 5.32. The rectifier outlet concentration is assumed to be constant at 0.992 and thus, a sharp decrease in the refrigerant flow rate exiting the refrigerant tank does not induce any sharp transients in the well-mixed refrigerant concentration inside the refrigerant tank. The refrigerant concentration stays at a constant value of 0.992 during the transient period from t = 550 s to t = 800 s.

5.6.4 Heat transfer rate and COP variation

Figure 5.33 shows the variation of heat transfer rates in response to the partial closing of the valve.

The evaporator heat duty decreases from 3.41 kW to 2.20 kW from t = 550 s to t = 800 s.

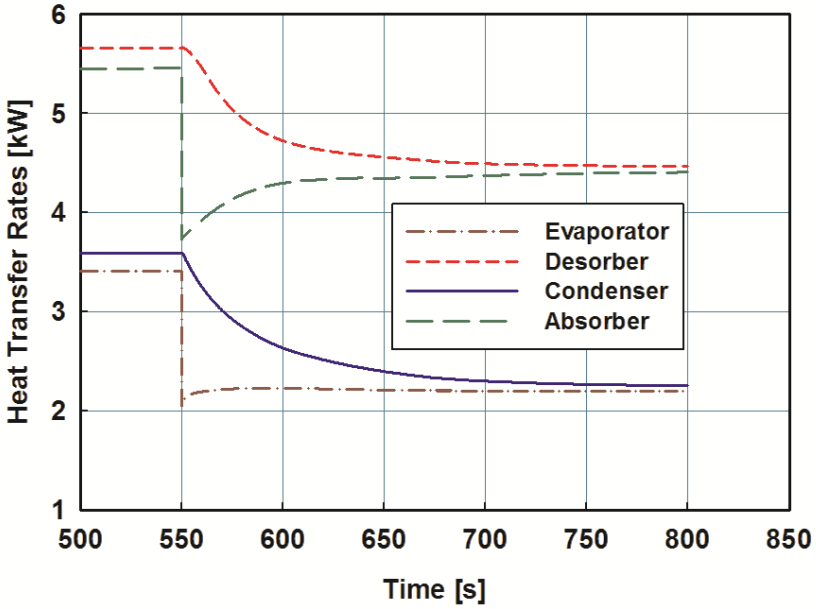

Figure 5.33 Heat transfer rate response to 40% closing of the refrigerant valve

A sharp decrease is observed in the evaporator heat duty at t = 550 s due to the reduction in the refrigerant flow rate. The gradual rise in the evaporator heat duty from t = 550 s to t = 800 s is due to a decrease in the low-side pressure (469 kPa to 229 kPa), which decreases the saturation temperature of refrigerant at the inlet of the evaporator from 4.2°C to -14.2°C. The decrease in saturation temperature results in an increase in the cooling capacity of the evaporator, although an increase in evaporator temperature glide (3 K to 26 K) at lower pressures limits the increase in the cooling capacity.

The desorber heat transfer rate decreases smoothly from 5.66 kW to 4.47 kW from t = 550 s to t = 800 s. The reduced refrigerant flow rate yields a lower desorber solution inlet concentration, decreasing the rate of vapor generation and heat transfer in the desorber. The absorber heat transfer rate decreases steeply from 5.46 kW to 3.74 kW at t = 550 s, but later increases gradually to 4.41 kW by t = 800 s, following trends in the refrigerant flow rate.

The condenser heat transfer rate decreases from 3.59 kW to 2.26 kW from t = 550 s and t = 800 s. The decrease is expected, again, as a result of the reduction in the refrigerant vapor flow rate into the condenser.

The condenser and desorber heat transfer rates vary smoothly, although a step reduction in valve coefficient is introduced. This is because the refrigerant expansion valve is placed downstream of the condenser and desorber, and the storage tank on the solution side dampens the effects on the condenser and desorber from the flow transient in the valve. However, the evaporator and absorber heat transfer rates respond sharply to the step reduction in the refrigerant valve coefficient.

Figure 5.34 shows the COP, desorber duty and evaporator cooling duty variations from t = 550 s to t = 800 s. The variations of evaporator and desorber duties were explained earlier in

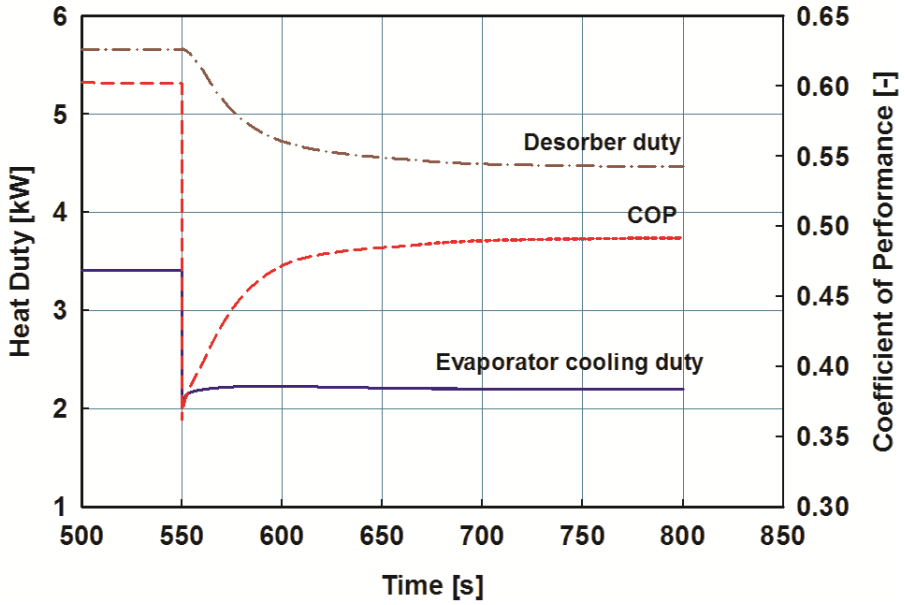

Figure 5.34 Evaporator cooling capacity, desorber heat input, and COP response to 40% closing of the refrigerant valve

this section. The evaporator duty increases from 2.05 kW to 2.20 kW from t = 550 s to t = 800 s after the initial step reduction. The evaporator duty variation settles to within 2% of this increase in 157 s.

The COP of the cycle decreases rapidly from 0.602 to 0.374 at t = 550 s, and then increases gradually to 0.492 by t = 800 s. The initial decrease results from the reduction in refrigerant flow rate. The evaporator cooling capacity increases after the initial transient period, whereas the desorber heat transfer rate continues to decrease, raising the COP to the higher steady state value.

5.6.5 Conclusions

The chiller response to a partial closing of the refrigerant valve is studied in this section by introducing a 40% step decrease ($\Delta C_{valve} = 1 \times 10^{-6}$ kg s^{-1} $Pa^{-0.5}$) in the refrigerant valve coefficient at t = 550 s. The evaporator and absorber heat transfer rates undergo a sharp transient at t = 550 s, whereas the condenser and desorber heat transfer rates decrease gradually during the period from t = 550 s to t = 800 s. The COP of the cycle undergoes a sharp reduction from 0.602

to 0.374 at t = 550 s and later, increases gradually to 0.492. The evaporator cooling capacity is decreased from 3.41 kW to 2.20 kW during this period due to the valve closing operation. The cooling capacity increases by 0.15 kW from t = 550 s to t = 800 s after the initial step decrease. The cooling capacity variation settles to within 2% of this increase in 157 s. The refrigerant flow rate is drastically reduced from 3.06 g s^{-1} to 1.84 g s^{-1} (40%) by the partial closing of the valve at t = 550 s, whereas the dilute solution flow rate is increased gradually.

The pressure variation during the period from t = 550 s to t = 800 s shows that the low-side pressure decreases from 469 kPa to 228 kPa, whereas the high-side pressure decreases from 1957 kPa to 1769 kPa. An increase in the pressure difference from t = 550 s to t = 800 s results in a slight increase in the refrigerant flow during the transient period. The concentration variation during the transient period shows that the concentrations of the dilute and concentrated solution are reduced by 18% and 25% due to the partial closing of the valve.

5.7 Summary of control responses

The previous sections of this chapter discussed the effects of several control inputs on the system behavior. These control inputs include step changes in the desorber coupling fluid temperature and flow rate, step increase in the solution pumping rate and step reduction in the valve setting for part load operation.

It was observed that a 10 K step increase in the inlet temperature of the desorber coupling fluid increased the cooling duty of the evaporator from 3.41 kW to 3.53 kW (3.2%) within a period of 200 s following the step change, and the COP was decreased from 0.602 to 0.594, while the refrigerant flow rate was increased from 3.062 g s^{-1} to 3.117 g s^{-1}. The time taken for the cooling capacity variation to settle to within 2% of the final value is 210 s. This could be an effective control strategy to increase the cooling capacity of the chiller within a short period of

time, and not change the COP of the chiller significantly. It could be practically achieved by increasing the exhaust/waste heat temperature to the absorption system. Second, a 0.017 kg s^{-1} (20%) increase in the coupling fluid flow rate of the desorber was implemented. The system performance results show that an increase in the chiller cooling capacity from 3.41 kW to 3.46 kW could be achieved within 200 s following the step change. The time taken for the cooling capacity variation to settle to within 2% of its final value is 190 s. The COP of the chiller increases from 0.602 to 0.604, which suggested that this control strategy could be used to meet the increased cooling demand of the chiller, with a slight improvement in system performance. This strategy could be achieved through an increased fuel supply (e.g., for a gas-fired desorber) to the desorber, or an increase in the exhaust flow rate, depending on the type of driving heat source. Third, the solution pumping rate was increased by 2 g s^{-1}(20%), and it was found that the evaporator cooling capacity was increased from 3.41 kW to 3.51 kW, while the COP of the chiller decreased from 0.602 to 0.579. The time taken for the cooling capacity variation to settle to within 2% of the increases value is 176 s. The increase in the solution pumping rate could be practically achieved through a step up motor for increasing the pumping rate. Finally, part-load operation of the chiller was studied by decreasing the valve setting by 40%. The system response showed that evaporator cooling duty decreased from 3.41 kW to 2.20 kW, while the COP of the chiller decreased from 0.602 to 0.374, and the refrigerant flow rate decreased from 3.06 g s^{-1} to 1.84 g s^{-1}. The cooling duty increases by 0.15 kW after the initial step decrease. The time taken for the cooling duty variation to settle to within 2% of this increase (0.15 kW from t = 550 s to t = 800 s) is 157 s.This control strategy could be implemented by simply turning down the expansion valve setting to establish part-load operation of the chiller.

Table 5.4 summarizes the results of the control responses considered in the study. In terms of the settling times, the response is the quickest when a valve closing operation is carried out, whereas it is the slowest when a 10 K step change is introduced in the desorber coupling fluid temperature. This difference in response times can be attributed to slow response to a temperature change due to system thermal mass, whereas the system pressure adjustment due to valve step operation takes place relatively quickly. The responses to an increase in flow rates are faster than those to a thermal step input, but slower than the response to a valve closing operation. It can therefore be concluded that a control input that directly influences the system pressures will result in shorter response times. The changes in steady state COP are not significant for most of the control inputs. The largest change observed in the COP (decrease by

Table 5.4 Summary of control responses

Control input	Effect on cooling capacity	Effect on system COP	Settling time for cooling capacity
10 K step increase in desorber coupling fluid temperature	Increase by 0.12 kW (3.5%)	Decrease by 0.008 (1.3%)	210 s
0.017 kg s^{-1} (20%) step increase in desorber coupling fluid flow rate	Increase by 0.05 kW (1.5%)	Increase by 0.002 (0.3%)	190 s
2 g s^{-1} (20%) step increase in solution pumping rate	Increase by 0.10 kW (2.9%)	Decrease by 0.023 (3.8%)	176 s
40% closing of the refrigerant valve	Decrease by 1.21 kW (35.5%)	Decrease by 0.11 (18%)	157 s

0.11, 18%) and cooling capacity (decrease by 1.21 kW, 36%) are for the valve closing operation, while the smallest change is observed for the step increase in the desorber coupling fluid flow rate. Thus, it can be concluded that valve setting is a parameter that influences the system response times and the magnitude of steady state responses significantly.

6. CONCLUSIONS AND RECOMMENDATIONS

6.1 Conclusions

A dynamic model was developed to study the transient behavior of a single-effect ammonia-water absorption chiller. The parameters used in the model such as system flow rates, heat exchanger size, coupling fluid temperatures and flow rates and thermal masses are representative of an experimental small-capacity absorption chiller developed by Determan and Garimella (2012).

The thermal storage capacities of the heat and mass transfer components, refrigerant and solution storage, flow rate development through the valves, etc. are accounted for in the dynamic model. Segmented models of heat and mass transfer components were employed to accurately model the transient phenomena. Storage tanks were modeled to account for expansion and storage of fluid during start-up, shut-down and other transient events. Equilibrium pressures inside the refrigerant and solution tanks established the high-side and low-side pressures respectively.

The following studies are conducted using the dynamic model to compute the transient performance of the chiller.

- System start-up from ambient conditions
- System response to step increase in the desorber coupling fluid temperature
- System response to step increase in the desorber coupling fluid flow rate
- System response to step increase in the pumping rate of solution
- Part-load operation of the chiller

Results from the transient start-up analysis indicate that the parameters such as flow rates, pressures and concentrations attained their steady-state values in approximately 550 s. The

desorber heat transfer rate increased rapidly, followed by the absorber heat transfer rate, and the condenser and evaporator heat transfer rates, respectively. The evaporator cooling capacity is 3.41 kW during steady-state for the given set of component sizes and pumping rate. The cooling capacity variation settled to within 2% of the steady-state value in 320 s. Thermal masses of the external heat exchangers were not included in the computation of chiller start-up. Their inclusion will cause an additional delay in the chiller start-up, but the trends observed in the system flow rates, heat transfer rates and COP are expected to be the same. The steady-state performance results obtained using the transient model were compared with an equivalent steady-state model, and the parameters such as concentrations, flow rates and pressures were found to match closely. A maximum deviation of 7.7% was observed in the COP estimation.

After validation with a steady-state model, analysis of system behavior under varying operating conditions was conducted. First, a 10 K step-increase in the desorber coupling fluid temperature was introduced at t = 550 s, when most system parameters have attained steady state after system start-up. Results from this study showed that the heat transfer rates of the desorber, absorber and condenser increased during the period from t = 550 s to t = 800 s. A higher rate of vapor generation was observed in the desorber due to higher heat transfer from the increased coupling fluid temperature . As a result, the high-side pressure rose. The cooling capacity of the evaporator increased from 3.41 kW to 3.53 kW within a period of 200 s after the step-change was introduced. The cooling capacity variation settled to within 2% of this increase in 210 s. The COP of the chiller decreased from 0.602 to 0.594, and the refrigerant flow rate increased from 3.062 g s^{-1} to 3.117 g s^{-1}.

Second, a 0.017 kg s^{-1} (20%) step-increase was introduced in the desorber coupling fluid flow rate at t = 550 s, and the chiller performance was analyzed during the transient period from t

= 550 s to t = 800 s. An increased vapor generation and higher heat transfer rate in the desorber were observed. The desorber and condenser heat transfer rates increased rapidly, whereas the absorber and evaporator heat transfer rates increased slowly because of a slow increase in refrigerant flow rate due to storage of refrigerant and solution in the storage tanks. The heat transfer rate in the desorber increased from 5.66 kW to 5.73 kW, and the evaporator cooling duty increased from 3.41 kW to 3.46 kW. As a result, the COP was increased slightly. The cooling duty variation settled to within 2% of this increase in 190 s. The refrigerant flow rate increased from 3.062 g s^{-1} to 3.076 g s^{-1}. The step-change in the coupling fluid flow rate resulted in a 1.5% increase in the evaporator cooling duty, and a slight improvement in the COP. In a practical scenario, an increase in the coupling fluid flow rate would consume additional pumping power. The effectiveness of this strategy depends on the marginal pumping power increase required to produce the additional evaporator cooling capacity of 0.05 kW.

Third, the solution pumping rate was increased from 9.75 g s^{-1} to 11.75 g s^{-1} (20%) at t = 550 s. The transient performance of the chiller was analyzed from t = 550 s and t = 800 s. In general, a higher pumping rate of solution resulted in an increase in the refrigerant and returning solution flow rates. A sudden increase in the pumping rate depleted ammonia from the solution tank, and was reflected in the reduced concentration of the pumped solution. The desorber and condenser heat transfer rates increased sharply at t = 550 s, whereas the absorber and evaporator heat loads increased gradually. The desorber heat transfer rate increased from 5.66 kW to 6.07 kW, whereas the evaporator cooling duty increased from 3.41 kW to 3.51 kW, thus resulting in a slight decrease in the COP. The cooling duty variation settled to within 2% of this increase in 176 s. The refrigerant flow rate across the valve increased from 3.062 g s^{-1} to 3.105 g s^{-1}. Thus, a 2 g s^{-1} increase in the pumping rate raised the chiller cooling capacity by 0.1 kW. Introducing

step-changes in the pumping rate could be an effective strategy to control the chiller performance. It could be implemented using a variable speed pump that alters the speed of the motor to achieve different pumping rates.

Finally, part-load operation of the chiller was studied by analyzing partial closing of the refrigerant expansion valve at t = 550 s. The evaporator and absorber heat transfer rates experienced sharp transients at t = 550 s, whereas the condenser and desorber heat transfer rates decreased gradually during the period from t = 550 s to t = 800 s. The refrigerant flow rate decreased from 3.06 g s^{-1} to 1.87 g s^{-1} due to the partial closing of the valve at t = 550 s. The concentrations of the dilute and concentrated solutions were significantly reduced by the simulated partial closing of the valve. The desorber heat transfer rate decreased from 5.66 kW to 4.47 kW, whereas the evaporator cooling duty decreased from 3.41 kW to 2.20 kW. A 0.15 kW increase in the cooling duty was observed after the initial step reduction. The cooling duty variation settled to within 2% of this increase in 157 s. The COP of the chiller decreased from 0.602 to 0.374, and the refrigerant flow rate decreased from 3.06 g s^{-1} to 1.84 g s^{-1}.

These results demonstrate the utility of this system model for studying the behavior of specific absorption systems under varying conditions, unlike most steady state models that do not account for the fixed total fluid charge. Additionally, such simulations can be used to predict the behavior of an absorption system under the continually varying conditions relevant to particular applications. Several controls strategies, such as evaporator temperature glide based control for the refrigerant flow rate, can also be investigated using this model.

6.2 Recommendations

The dynamic model was developed with an objective to study overall chiller behavior during start-up, part-load operation and other transient events. The effect of system parameters

such as heat exchanger size, solution flow rates, specific pump curves, coupling fluid temperatures and flow rates on the transient performance of the absorption system can be studied in detail using the model developed in this work. Several control responses were investigated using this model. In future, a rigorous parametric study should be conducted to establish the strategy best suited for the desired performance. Future work should incorporate additional sub-models accounting for varying thermal capacity of coupling fluid lines and ambient heat exchangers, and could be employed to predict transient performance of a specific installation of the chiller.

As discussed in Chapter 4, several simplifications were made in the component models. A fixed concentration of refrigerant was assumed at the outlet of the rectifier. Future models should assign a specific UA value to the rectifier, and model the heat and mass transfer between the liquid-vapor phases, to estimate the refrigerant concentration at the outlet of the rectifier. Furthermore, the mass transfer resistance between the liquid and vapor phases in the absorber was neglected in the dynamic model. A detailed component model such as the falling-film absorber can be included to accurately model the mass transfer process inside the absorber. A rigorous analysis involving the non-linear 1-D momentum equation and estimation of the interfacial areas could be done to improve the accuracy of the overall system model. However, it would consume more computational time to achieve this level of accuracy. Also, the thermal masses of the connecting lines were neglected in this model. They could be included to account for additional transport delays in the system. Also, constant values of heat transfer coefficients were used by the model. Appropriate correlations could be used to estimate the heat transfer coefficient at each time instant to model the heat and mass transfer processes more accurately.

The present model assumes quasi-steady heat and mass transfer processes inside the rectifier. Future models could account for the transient phenomena in the rectifier by including a simplified heat and mass exchanger model (two to three segments).

Appendix A. Thermal Conductance Estimation

Table A-1 Thermal Conductance Estimation

Absorber

Shim A (Coupling fluid)

$N_{sh} = 26$

$N_{ch/sh} = 88$

$L_{ch} = 0.212$ m

$P_{ch} = 1.93\times10^{-3}$ m

$A_{cf} = N_{sh}\times N_{ch/sh}\times L_{ch}\times P_{ch} = 0.93$ m^2

Heat transfer correlation for flow in a circular duct: (Kakac *et al.*, 1987)

$$\frac{\alpha D_h}{k} = 2.0705\cdot(1+2.2916\varphi-2.5682\varphi^2+1.4815\varphi^3-0.3338\varphi^4)$$

$D_h = 306\times10^{-6}$ m

k = 0.6306 W m^{-1} K^{-1}

$2\varphi = \pi$

$\alpha = 4559$ W m^{-2} K^{-1}

Thermal conductance of coupling fluid side: $(\alpha A)_{cf} = 4272$ W K^{-1}

Shim B (Ammonia-water)

$N_{sh} = 25$

$N_{ch/sh} = 88$

$L_{ch} = 0.248$ m

$P_{ch} = 1.9\times10^{-3}$ m

$A_f = N_{sh}\times N_{ch/sh}\times L_{ch}\times P_{ch} = 1.06$ m^2

Heat transfer correlation for condensation in tubes: (Shah, 1979)

$$\alpha_{tp} = \alpha_{lo}\left[(1-q)^{0.8}+\frac{3.8q^{0.76}(1-q)^{0.04}}{\mathrm{Pr}^{0.38}}\right]$$

$$\alpha_{lo} = 0.023\,\mathrm{Re}_{lo}^{0.8}\,\mathrm{Pr}_l^{0.4}\times\frac{k_l}{D_h}$$

$q = 0.1, \alpha_{lo} = 550$ W m^{-2} K^{-1}

$\alpha_{tp} = 1550$ W m^{-2} K^{-1}

Thermal conductance of fluid side: $(\alpha A)_f = 1636$ W K^{-1}

Table A-1 (continued)

Condenser

Shim A (Coupling fluid)

$N_{sh} = 26$

$N_{ch/sh} = 75$

$L_{ch} = 0.1206$ m

$P_{ch} = 1.93\times10^{-3}$ m

$A_{cf} = N_{sh}\times N_{ch/sh}\times L_{ch}\times P_{ch} = 0.45$ m^2

Heat transfer correlation for flow in a circular duct: (Kakac *et al.*, 1987)

$$\frac{\alpha D_h}{k} = 2.0705\cdot(1+2.2916\varphi-2.5682\varphi^2+1.4815\varphi^3-0.3338\varphi^4)$$

$D_h = 306\times10^{-6}$ m

k = 0.6306 W m^{-1} K^{-1}

$2\varphi = \pi$

$\alpha = 4527$ W m^{-2} K^{-1}

Thermal conductance of coupling fluid side: $(\alpha A)_{cf} = 2056$ W K^{-1}

Shim B (Ammonia-water)

$N_{sh} = 25$

$N_{ch/sh} = 75$

$L_{ch} = 0.155$ m

$P_{ch} = 1.9\times10^{-3}$ m

$A_f = N_{sh}\times N_{ch/sh}\times L_{ch}\times P_{ch} = 0.56$ m^2

Heat transfer correlation for condensation in tubes: (Shah, 1979)

$$\alpha_{tp} = \alpha_{lo}\left[(1-q)^{0.8}+\frac{3.8q^{0.76}(1-q)^{0.04}}{\mathrm{Pr}^{0.38}}\right]$$

$$\alpha_{lo} = 0.023\,\mathrm{Re}_{lo}^{0.8}\,\mathrm{Pr}_l^{0.4}\times\frac{k_l}{D_h}$$

$q = 0.4, \alpha_{lo} = 302.7$ W m^{-2} K^{-1}

$\alpha_{tp} = 1692$ W m^{-2} K^{-1}

Thermal conductance of fluid side: $(\alpha A)_f = 952$ W K^{-1}

Table A-1 (continued)

Evaporator

Shim A (Coupling fluid)

$N_{sh} = 34$

$N_{ch/sh} = 75$

$L_{ch} = 0.051$ m

$P_{ch} = 1.93\times10^{-3}$ m

$A_{cf} = N_{sh}\times N_{ch/sh}\times L_{ch}\times P_{ch} = 0.25$ m^2

Heat transfer correlation for flow in a circular duct: (Kakac *et al.*, 1987)

$$\frac{\alpha D_h}{k} = 2.0705\cdot(1+2.2916\varphi-2.5682\varphi^2+1.4815\varphi^3-0.3338\varphi^4)$$

$D_h = 306\times10^{-6}$ m

k = 0.4595 W m^{-1} K^{-1}

$2\varphi = \pi$

$\alpha = 4245$ W m^{-2} K^{-1}

Thermal conductance of coupling fluid side: $(\alpha A)_{cf} = 1062$ W K^{-1}

Shim B (Ammonia-water)

$N_{sh} = 17$

$N_{ch/sh} = 75$

$L_{ch} = 0.085$ m

$P_{ch} = 1.9\times10^{-3}$ m

$A_f = N_{sh}\times N_{ch/sh}\times L_{ch}\times P_{ch} = 0.21$ m^2

Heat transfer correlation for condensation in tubes: Kandlikar *et al.* (2003; 2004)

$$\alpha_{tp} = 0.6683\cdot \mathrm{Co}^{-0.2}(1-q)^{0.8}\alpha_{lo} + 1058\mathrm{Bo}^{0.7}(1-q)^{0.8}F_{fl}\alpha_{lo}$$

$$\frac{\alpha_{lo} D_h}{k_l} = 2.0705\cdot(1+2.2916\varphi-2.5682\varphi^2+1.4815\varphi^3-0.3338\varphi^4)$$

$$\mathrm{Co} = \left[\frac{(1-q)}{q}\right]^{0.8}\left[\frac{\rho_v}{\rho_l}\right]^{0.5}$$

$$\mathrm{Bo} = \frac{q''}{G\cdot h_{LV}}$$

$q = 0.7, F_{fl} = 1, G = 8.2$ kg m^{-2} s^{-1}

$\alpha_{tp} = 10,305$ W m^{-2} K^{-1}

Thermal conductance of fluid side: $(\alpha A)_f = 2173$ W K^{-1}

Table A-1 (continued)

SHX

Shim A (Dilute solution)

$N_{sh} = 26$

$N_{ch/sh} = 42$

$L_{ch} = 0.044$ m

$P_{ch} = 1.93\times10^{-3}$ m

$A_{cf} = N_{sh}\times N_{ch/sh}\times L_{ch}\times P_{ch} = 0.094$ m^2

Heat transfer correlation for flow in a circular duct: (Kakac *et al.*, 1987)

$$\frac{\alpha D_h}{k} = 2.0705\cdot(1+2.2916\varphi-2.5682\varphi^2+1.4815\varphi^3-0.3338\varphi^4)$$

$D_h = 306\times10^{-6}$ m

$k = 0.588$ W m^{-1} K^{-1}

$2\varphi = \pi$

$\alpha = 5451$ W m^{-2} K^{-1}

Thermal conductance of hot fluid side: $(\alpha A)_{hot} = 511$ W K^{-1}

Shim B (Concentrated solution)

$N_{sh} = 25$

$N_{ch/sh} = 42$

$L_{ch} = 0.073$ m

$P_{ch} = 1.9\times10^{-3}$ m

$A_f = N_{sh}\times N_{ch/sh}\times L_{ch}\times P_{ch} = 0.148$ m^2

Heat transfer correlation for flow in a circular duct: (Kakac *et al.*, 1987)

$$\frac{\alpha D_h}{k} = 2.0705\cdot(1+2.2916\varphi-2.5682\varphi^2+1.4815\varphi^3-0.3338\varphi^4)$$

$D_h = 306\times10^{-6}$ m

$k = 0.50$ W m^{-1} K^{-1}

$2\varphi = \pi$

$\alpha = 4765$ W m^{-2} K^{-1}

Thermal conductance of cold fluid side: $(\alpha A)_{cold} = 705$ W K^{-1}

Table A-1 (continued)

RHX

Shim A (Hot ammonia-water)

$N_{sh} = 26$

$N_{ch/sh} = 42$

$L_{ch} = 0.114$ m

$P_{ch} = 1.93\times10^{-3}$ m

$A_{cf} = N_{sh}\times N_{ch/sh}\times L_{ch}\times P_{ch} = 0.241$ m^2

Heat transfer correlation for flow in a circular duct: (Kakac *et al.*, 1987)

$$\frac{\alpha D_h}{k} = 2.0705\cdot(1+2.2916\varphi-2.5682\varphi^2+1.4815\varphi^3-0.3338\varphi^4)$$

$D_h = 306\times10^{-6}$ m

$k = 0.46$ W m^{-1} K^{-1}

$2\varphi = \pi$

$\alpha = 4142$ W m^{-2} K^{-1}

Thermal conductance of hot fluid side: $(\alpha A)_{hot} = 998$ W K^{-1}

Shim B (Cold ammonia-water)

$N_{sh} = 25$

$N_{ch/sh} = 42$

$L_{ch} = 0.143$ m

$P_{ch} = 1.9\times10^{-3}$ m

$A_f = N_{sh}\times N_{ch/sh}\times L_{ch}\times P_{ch} = 0.29$ m^2

Heat transfer correlation for flow in a circular duct: (Kakac *et al.*, 1987)

$$\frac{\alpha D_h}{k} = 2.0705\cdot(1+2.2916\varphi-2.5682\varphi^2+1.4815\varphi^3-0.3338\varphi^4)$$

$D_h = 306\times10^{-6}$ m

$2\varphi = \pi$

$\alpha = 274$ W m^{-2} K^{-1}

Thermal conductance of cold fluid side: $(\alpha A)_{cold} = 80$ W K^{-1}

Table A-1 (continued)

Desorber

Shim A (Coupling fluid)

$N_{sh} = 19$

$N_{ch/sh} = 102$

$L_{ch} = 0.102$ m

$P_{ch} = 1.93\times10^{-3}$ m

$A_{cf} = N_{sh}\times N_{ch/sh}\times L_{ch}\times P_{ch} = 0.374$ m^2

Heat transfer correlation for flow in a circular duct: (Kakac *et al.*, 1987)

$$\frac{\alpha D_h}{k} = 2.0705\cdot(1+2.2916\varphi-2.5682\varphi^2+1.4815\varphi^3-0.3338\varphi^4)$$

$D_h = 306\times10^{-6}$ m

k = 0.1 W m^{-1} K^{-1}

$2\varphi = \pi$

$\alpha = 900$ W m^{-2} K^{-1}

Thermal conductance of coupling fluid side: $(\alpha A)_{cf} = 337$ W K^{-1}

Shim B (Ammonia-water)

$N_{sh} = 8$

$N_{ch/sh} = 2$

$A_f = 0.111$ m^2

$\alpha = 6500$ W m^{-2} K^{-1}

Thermal conductance of fluid side: $(\alpha A)_f = 726$ W K^{-1}

REFERENCES

Bittanti, S., A. DeMarco, M. Giannatempo and V. Prandoni (2010), "A Dynamic Model of an Absorption Chiller for Air Conditioning," *Proceedings of the International Conference on Renewable Energies and Power Quality, Granada: Spain* pp. 1-6.

Butz, D. and K. Stephan (1989), "Dynamic Behavior of an Absorption Heat Pump," *International Journal of Refrigeration* Vol. 12(4) pp. 204-212.

Cai, W., M. Sen and S. Paolucci (2011), "Dynamic Simulation of an Ammonia–Water Absorption Refrigeration System," *Industrial & Engineering Chemistry Research* Vol. 51(4) pp. 2070-2076.

Determan, M. D. and S. Garimella (2012), "Design, Fabrication, and Experimental Demonstration of a Microscale Monolithic Modular Absorption Heat Pump," *Applied Thermal Engineering* Vol. 47(0) pp. 119-125.

Fernández-Seara, J. and M. Vázquez (2001), "Study and Control of the Optimal Generation Temperature in Nh3–H2o Absorption Refrigeration Systems," *Applied Thermal Engineering* Vol. 21(3) pp. 343-357.

Fu, D. G., G. Poncia and Z. Lu (2006), "Implementation of an Object-Oriented Dynamic Modeling Library for Absorption Refrigeration Systems," *Applied Thermal Engineering* Vol. 26(2–3) pp. 217-225.

Incropera, F. P. and D. P. DeWitt (1996). *Fundamentals of Heat and Mass Transfer*. 4th Edition Ed., John Wiley & Sons. p. 581-619.

Jeong, S., B. H. Kang and S. W. Karng (1998), "Dynamic Simulation of an Absorption Heat Pump for Recovering Low Grade Waste Heat," *Applied Thermal Engineering* Vol. 18(1–2) pp. 1-12.

Kakac, S., R. K. Shah and W. Aung (1987). *Handbook of Single-Phase Convective Heat Transfer*. New York, Wiley.

Kandlikar, S. G. and P. Balasubramanian (2004), "An Extension of the Flow Boiling Correlation to Transition, Laminar and Deep Laminar Flows and Microchannels," *Heat Transfer Engineering* Vol. 25(3) pp. 86-93.

Kandlikar, S. G. and M. E. Steinke (2003), "Predicting Heat Transfer During Flow Boiling in Minichannels and Microchannels," *Amer. Soc. Heating, Ref. Air-Conditioning Eng. Inc.*, Chicago, IL, United States, pp. 667-676.

Kaushik, S., N. Sheridan, K. Lam and S. Kaul (1985), "Dynamic Simulation of an Ammonia-Water Absorption Cycle Solar Heat Pump with Integral Refrigerant Storage," *Journal of Heat Recovery Systems* Vol. 5(2) pp. 101-116.

Kim, B. and J. Park (2007), "Dynamic Simulation of a Single-Effect Ammonia–Water Absorption Chiller," *International Journal of Refrigeration* Vol. 30(3) pp. 535-545.

Klein, S. A. (2010). *Engineering Equation Solver*.

Klein, S. A. *e. a.* (2006). *Trnsys Manual, a Transient Simulation Program* Madison: Solar Engineering Laboratory, Univeristy of Wisconsin-Madison.

Kohlenbach, P. and F. Ziegler (2008a), "A Dynamic Simulation Model for Transient Absorption Chiller Performance. Part I: The Model," *International Journal of Refrigeration* Vol. 31(2) pp. 217-225.

Kohlenbach, P. and F. Ziegler (2008b), "A Dynamic Simulation Model for Transient Absorption Chiller Performance. Part Ii: Numerical Results and Experimental Verification," *International Journal of Refrigeration* Vol. 31(2) pp. 226-233.

Marc, O., F. Lucas, F. Sinama and E. Monceyron (2010), "Experimental Investigation of a Solar Cooling Absorption System Operating without Any Backup System under Tropical Climate," *Energy and Buildings* Vol. 42(6) pp. 774-782.

MathWorks (2010). *Matlab*. Natick, MA.

Matsushima, H., T. Fujii, T. Komatsu and A. Nishiguchi (2010), "Dynamic Simulation Program with Object-Oriented Formulation for Absorption Chillers (Modelling, Verification, and Application to Triple-Effect Absorption Chiller)," *International Journal of Refrigeration* Vol. 33(2) pp. 259-268.

Monné, C., S. Alonso, F. Palacín and L. Serra (2011), "Monitoring and Simulation of an Existing Solar Powered Absorption Cooling System in Zaragoza (Spain)," *Applied Thermal Engineering* Vol. 31(1) pp. 28-35.

Nellis, G. and S. A. Klein (2009). *Heat Transfer*, Cambridge University Press. p 823-831, 841-848.

Nielsen, T. R., J. Rose and J. Kragh (2009), "Dynamic Model of Counter Flow Air to Air Heat Exchanger for Comfort Ventilation with Condensation and Frost Formation," *Applied Thermal Engineering* Vol. 29(2–3) pp. 462-468.

Paratherm (2012). *Paratherm Nf Heat Transfer Fluid*.

Patankar, S. V. (1980). *Numerical Heat Transfer and Fluid Flow*, Hemisphere Publishing Corporation, Taylor and Francis Group, New York.

Pérez de Viñaspre, M., M. Bourouis, A. Coronas, A. García, V. Soto and J. M. Pinazo (2004), "Monitoring and Analysis of an Absorption Air-Conditioning System," *Energy and Buildings* Vol. 36(9) pp. 933-943.

Prasartkaew, B. and S. Kumar (2010), "A Low Carbon Cooling System Using Renewable Energy Resources and Technologies," *Energy and Buildings* Vol. 42(9) pp. 1453-1462.

Rattner, A. S. and S. Garimella (in preparation, 2013), "Fast, Stable Computation of Thermodynamic Properties of Ammonia-Water Mixtures," *International Journal of Refrigeration*.

Shah, M. M. (1979), "A General Correlation for Heat Transfer During Film Condensation inside Pipes," *International Journal of Heat and Mass Transfer* Vol. 22(4) pp. 547-556.

Syed, A., M. Izquierdo, P. Rodríguez, G. Maidment, J. Missenden, A. Lecuona and R. Tozer (2005), "A Novel Experimental Investigation of a Solar Cooling System in Madrid," *International Journal of Refrigeration* Vol. 28(6) pp. 859-871.

Wang, S. K. (2001), *Handbook of Air Conditioning and Refrigeration.* Vol. 2 Ed. New York, McGraw-Hill.

Ziegler, B. and C. Trepp (1984), "Equation of State for Ammonia-Water Mixtures," *International Journal of Refrigeration* Vol. 7(2) pp. 101-106.

Zinet, M., R. Rulliere and P. Haberschill (2012), "A Numerical Model for the Dynamic Simulation of a Recirculation Single-Effect Absorption Chiller," *Energy Conversion and Management* Vol. 62(0) pp. 51-63.